Università degli Studi di Milano
Facoltà di Scienze Matematiche, Fisiche e Naturali
Dottorato di Ricerca in
Fisica, Astrofisica e Fisica Applicata

Study of fast electron transport and energetic proton generation at high laser intensity and application to fast ignition

Coordinatore Prof. Marco Bersanelli

Tutore Prof. Nicola Piovella

Tesi di Dottorato

di

Alessio Morace
Ciclo XXV

Anno Accademico 2009-2010

Contents

List of Figures

List of Tables

Chapter 1

Inertial Confinement Fusion

1.1 Introduction

The achievement of controlled energy gain via nuclear fusion would represent an enormous step forward for mankind. The possibility to access a virtually unlimited and potentially clean source of energy can be the answer to the world energetic increasing request, global warming, and at the same time a factor of political stability. The Inertial Confinement Fusion (ICF) concept consists in compressing and heating a Deuterium- Tritium capsule (DT), up to ignition conditions, by means of a large number of symmetrically arranged highly energetic ns laser pulses or Z-pinches. Despite the fact that fusion energy gain was already demonstrated 61 years ago, in a fashion conceptually very similar to the ICF approach, it is only recently that the quest for controlled thermonuclear fusion has become possible. The Ivy Mike event on Bikini Island , with a yield of 10 Mt, was the first full-scale fusion experiment. The liquid isotopes were compressed and heated by means of a fission nuclear device, which was used as driver. The explosive release of such amount of energy in atmosphere is clearly not recommended and definitely not suitable for energy production. Up to now, this has been the only effective method to obtain fusion energy gain. For the first time in history, the possibility to achieve this outstanding result becomes realistic. The National Ignition Facility (NIF) at Lawrence Livermore National Laboratory, with a

laser energy of $\sim 2MJ$ and peak power of $\sim 500TW$, is now conducting an experimental campaign, the National Ignition Campaign (NIC) focused on the Central Host Spot (CHS) ignition of a spherical DT ice shell containing DT gas. CHS ignition is considered to be the classic ICF approach and his conception is as old as the discovery of laser is. Alternative approaches to ICF have been conceived with the evolution of laser sources and the introduction of the Chirped Pulse Amplification technique, allowing the generation of ultra-high intensity laser pulses, with intensities on target above the relativistic threshold $10^{18}W/cm^2$ attaining the relativistic regime. This regime is characterized by relativistic oscillatory energy of the electron under the action of the laser field. At this regime, a generalization of radiation pressure called ponderomotive force (still present at lower laser intensities), becomes the predominant effect, determining plasma electrons acceleration up to several MeV. The acceleration process is very efficient, turning about 50% of laser energy into fast electrons, with energies $\geq$ 1MeV. Besides the pure scientific interest of such a high brightness sources, many are the possible applications that have been proposed. These electron beams can propagate through the matter releasing their energy and heating up the target material up to several tens or hundreds of eV with the actual available laser system, opening a all new scenario in the study of matter at extreme conditions, including astrophysical objects and particularly planetology. The high electron energy can be used to produce bright, ultrafast x-ray sources, to be used as diagnostic for fast or transient events, from implosion radiography to Compton scattering on shock-driven samples, allowing the study of material phase changes under extreme pressure conditions. The generation of fast electron beams in thin foils con lead to the production of energetic proton beams, whose applications range from microscopy and plasma diagnostic to cancer treatment with hadrons. A very important application of high-intensity laser-produced fast electron and proton beams resides in an alternative approach to ICF, called Fast Ignition (FI). In FI, differently from the classic CHS ignition approach, the phases of compression and heating are separated, and the compressed DT core heating is delegated to a fast electron or fast ion beam, releasing its energy in a small region of the core, producing a lateral hot spot, from

which the thermonuclear burst will propagate through the compressed DT fuel. The reason to pursue an alternative ignition approach resides in the very tight constraints of CHS ignition approach, which can be loosen in the alternative FI scheme. In this work the author will illustrate the principles of classic and alternative ignition approaches and concentrate his attention on aspects of fast electron transport and proton beam generation of high relevance for FI science.

1.2 Nuclear fusion

Nuclear fusion is a particular type of exothermic nuclear reaction. In general, we can define an exothermic nuclear reaction when the mass of the reaction products is lower than the mass of the reagent nuclei. The missing mass is released as energy, following the well known Einstein's special relativity result:

$$\Delta E = \Delta m_{nuclei} c^2. \tag{1.1}$$

We can associate ΔE to the binding energy of a nucleus. Indeed the total mass of a nucleus differ from the total mass of its single components by

$$\Delta m = Z m_p + (A - Z)\, m_n - m \tag{1.2}$$

and the binding energy of the nucleus can be therefore written as

$$E_{bin} = \Delta m c^2. \tag{1.3}$$

Finally we can write the total energy released in a nuclear reaction as

$$\Delta E = \Delta m_{nuclei} c^2 = \sum_f E_{bin_f} - \sum_i E_{bin_i}. \tag{1.4}$$

If we plot the binding energy per nucleon E_{bin}/A as function of the mass number A, appears clear that is possible to produce nuclear energy by dividing high Z nuclei (fission) or fusing together low Z nuclei. The element for which the binding energy is maximum is Fe. Fission or fusion of Fe ions do

not produce any nuclear energy being instead an endothermic reaction. This reaction is very important for the final stages of the evolution of massive stars, with mass exceeding 10 solar masses.

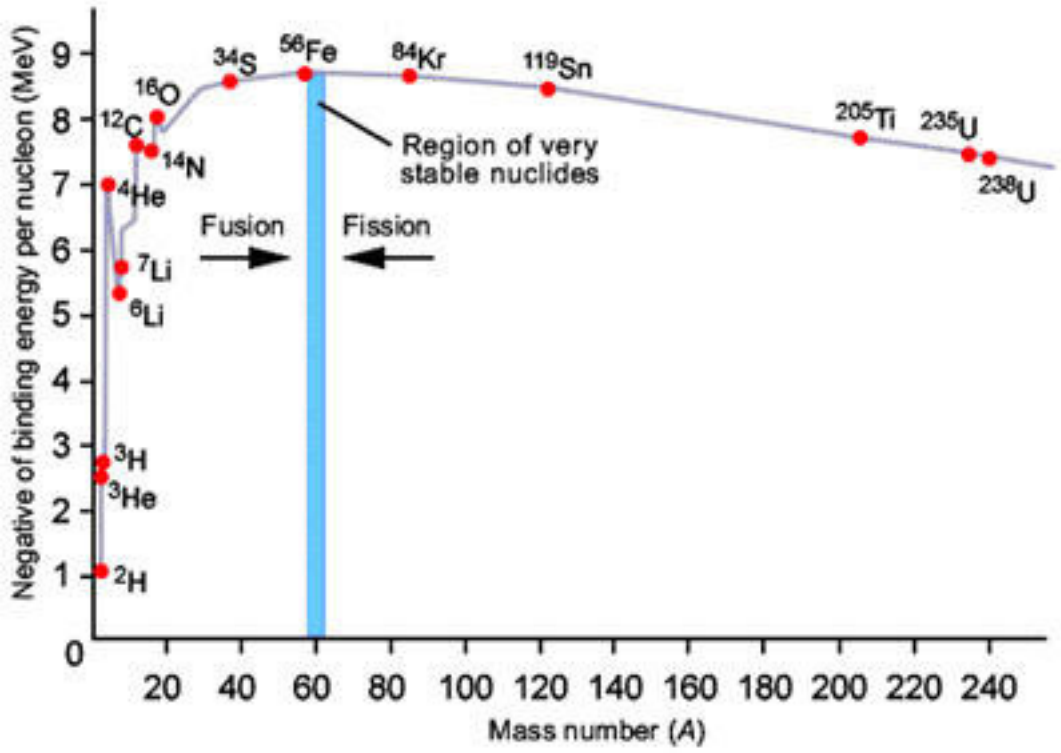

Figure 1.1: **Binding energy per nucleon versus atomic mass number A**

Up to now, the only source of nuclear energy has been represented by fission of U^{235} nuclei in a nuclear power plant. The total energy produced in a single fission event is around 220 MeV. Nuclear power plants in the United States produce a total of 807 billion of kWh, covering the 20% of the energy production in the country. Despite the great advantages of fission power plants in terms of amount of energy produced, strong reduction in air pollution and greenhouse gas production, several are the problems related to this source of energy. The limited reserve of uranium guarantees energy production at the actual rate for no more than 100 years. The large quantity of nuclear waste produced represents a serious concern in terms of stok-

ing and related safety and security issues. Moreover nuclear power plants are not completely safe in terms of accidents or terroristic attacks, as appeared clear after the Japan earthquake and tsunami that severely damaged the Fukushima power plant, releasing large quantities of radioactive material in the surrounding areas. Nuclear fusion instead, produces no nuclear waste except for some neutron stimulated nuclear activation of the interaction chamber walls. Moreover it is intrinsically safe and, being hydrogen the most common element in the Universe, it represents an endless supply of fuel for fusion energy.

A fusion event occurs when interacting nuclei have enough energy to overcome the Coulomb repulsion and get into the nuclear potential well, of depth $\sim 30 - 40$ MeV. The maximum Coulomb potential is given by

$$V_C = \frac{Z_1 Z_2 e^2}{r_n} \tag{1.5}$$

where Z_1 and Z_2 are the nuclear charges and r_n is the inter-nuclei distance $r_n = 1.44 \times 10^{-13} \left(A_1^{1/3} + A_2^{1/3} \right)$, where A_1 and A_2 are the atomic numbers of the reagents. The maximum Coulombe potential energy, related to r_n is about 1 MeV. In the classical limit, the interacting nuclei must have a total energy ≥ 1 MeV to have a non-zero probability to fuse. However, fusion events occur at much lower ion energies. This is quantum mechanically allowed by tunnelling effect of a finite potential barrier. The fundamental quantity for the treatment of nuclear reactions is the cross section, $\sigma(v)$, where v is the relative velocity of the interacting particles. The cross section represents the probability of the reaction event per pair of ions. The probability of reaction per unit time is given by $n\sigma(v)\, v$. Another very important quantity is the fusion reactivity, which is defined as the probability of reaction per unit time and unit density of target nuclei. Assuming a normalized velocity distribution $f(v)$ for the interacting nuclei, we can define the average fusion reactivity as

$$\langle \sigma v \rangle = \int_0^\infty \sigma(v)\, v f(v) dv \tag{1.6}$$

and the volumetric reaction rate is given by

$$R_{12} = \frac{f_1 f_2}{1 + \delta_{12}} n^2 \langle \sigma v \rangle, \tag{1.7}$$

where the indices 1 and 2 indicate the two reacting ion species and δ_{ij} is the Kronecker symbol. In Figure **??** are represented the fusion cross sections versus ion temperature in eV for hydrogen isotopes and light elements including Litium, Boron and Helium. From Figure **??** appears clear that, above

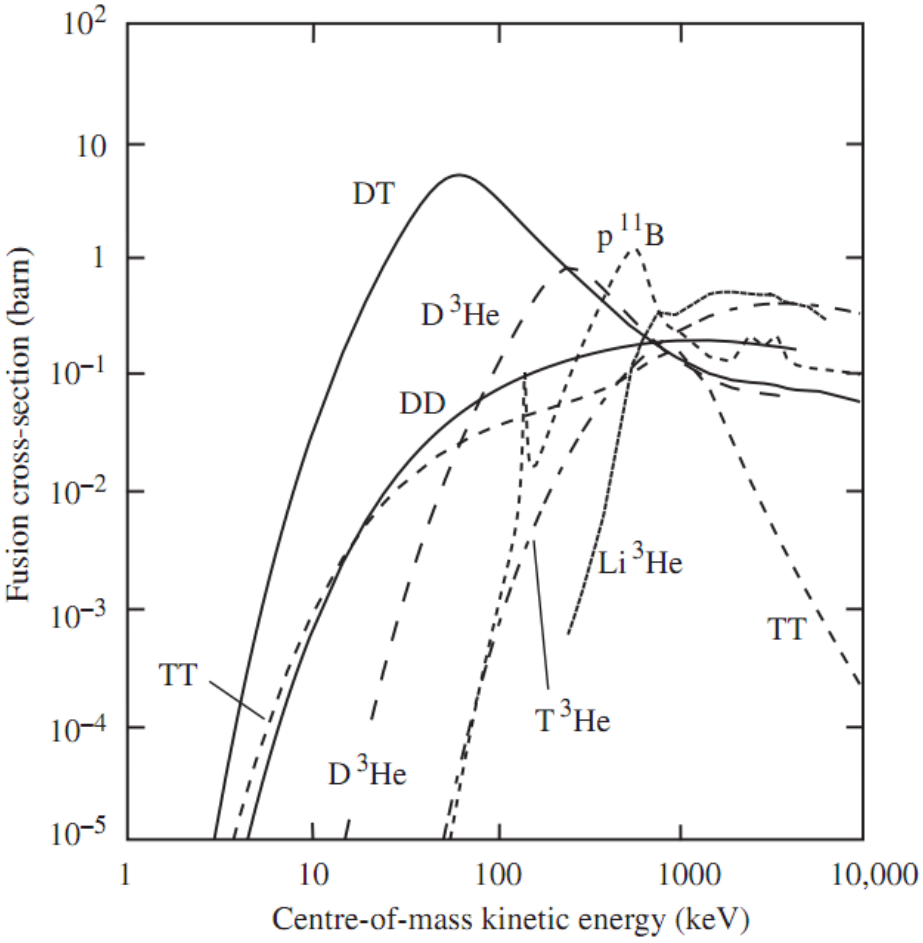

Figure 1.2: **Fusion cross sections for hydrogen isotopes and light elements versus ion temperature. The DT fusion cross section is the largest at low temperatures. (S. Atzeni and Mayer Ter Ven).**

all the fusion reactions, DT has the larger cross section at low temperatures

and is therefore the most suitable fuel for a fusion reactor. The DT fusion reaction

$$D + T \longrightarrow \alpha(3.5MeV) + n(14.1MeV) \tag{1.8}$$

releses a total of 17.6 MeV per fusion reaction, the most of it carried by the neutron, while the α particle energy, responsible for the plasma heating, guarantees the reaction to be self sustained. The plasma temperature necessary to achieve a self sustained nuclear fusion reaction is above 5 keV. No materials can sustain such temperature, without ionize and become plasmas, therefore a method to confine such a high temperature plasmas in a proper container is required. ICF represents one of the possible approaches to solve this issue. The plasma is confined by its own mass inertia in a small volume of radius R, over a period of time equal to the time required to a sound wave of speed c_s to travel from the center to the surface of the sphere. In this short amount of time, the thermonuclear burn occurs.

1.3 Principles of Inertial Confinement Fusion

Laser driven ICF in its classical fashion consist of four fundamental stages:

1. quasi-isentropic shell compression
2. adiabatic heating of a small portion of fuel
3. fuel ignition at the moment of stagnation
4. combustion of the cold fuel in the shell ...

and it is based on a single, shaped laser pulse constituted of multiple beams. The implosion of the shell is driven by laser irradiation, which deposits the energy onto the capsule surface producing mass ablation. The shell acceleration is produced by ablation pressure: while the ablated mass flows outwards, the shell is accelerated inwards for momentum conservation as in a spherical rocket. If we indicate the velocity of the ablated plasma as v_{abl}, the mass of the ablated shell as Δm, the velocity of the imploding shell as v_{sh} and its

mass M, the momentum conservation condition is given by:

$$\Delta m v_{abl} = (M - \Delta m)\, v_{sh} \tag{1.9}$$

and the rocket equation is :

$$M\frac{dv_{sh}}{dt} = -v_{abl}\frac{dM}{dt}, \tag{1.10}$$

finally we obtain for the shell velocity :

$$v_{sh} = v_{abl} \ln \frac{M_0}{M(t)}. \tag{1.11}$$

The maximum implosion velocity of the shell determines the hot spot temperature at stagnation time. The compression has to be quasi-isentropic in order to minimize the driver energy. Indeed, if we define U as internal energy of the compressed DT gas, S as the entropy, P and V respectively as the DT gas pressure and the volume of the shell, it follows from the first law or thermodynamics that:

$$dU = TdS - PdV. \tag{1.12}$$

Therefore order to minimize the invested energy, we need to adiabatically heat the fuel ($dS = 0$). The heating of DT plasma is then simply produced by thermodynamic work PdV. At stagnation time, the compressed DT gas has a very high temperature (~ 5) keV and a relatively low density ($\rho R_{HS} \simeq 0.2\text{g/cm}^2$), and is surrounded by a cold, dense DT shell. This configuration is defined as isobaric fuel assembly (figure **??**). The fraction of fuel that triggers the thermonuclear burst is therefore a small fraction ($\simeq 3 - 5\%$) of the total DT mass. The surrounding DT shell is supposed to be ignited by the energy released by the α particles produced during the fusion of the hot spot plasma. To achieve self sustained nuclear fusion reactions, the α particle heating rate must be larger than the power loss rate. This can be summarized in the so-called Lawson criterion :

$$\frac{\epsilon_\alpha}{4} n^2 \langle \sigma\nu \rangle > \frac{3}{2}\frac{P}{\tau}. \tag{1.13}$$

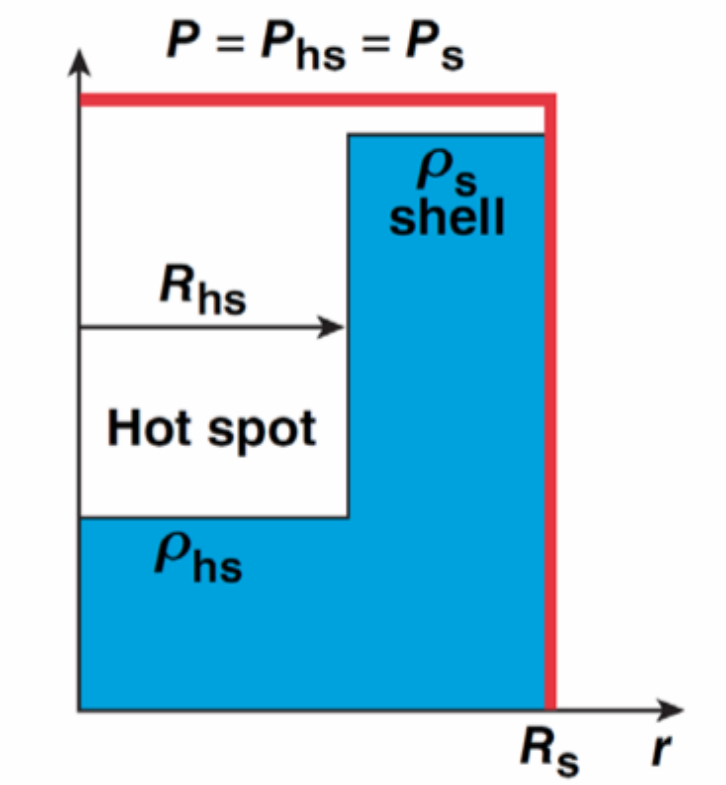

Figure 1.3: **Isobaric fuel assembly in central hot spot ignition. Courtesy of prof. R. Betti.**

Where ϵ_α is the energy of the α particle, n the ion density (we assume an identical concentration of D and T ions), $\langle\sigma\nu\rangle$ is the DT fusion reactivity, P the plasma pressure and τ the energy confinement time, which corresponds to the time spent by a sound wave of speed $c_s = \sqrt{2k_bT/m}$ to travel from the center to the boundary of the hot spot $\tau = R_{hs}/c_s$. The right hand side of the inequality **??** represents the expansion losses or the internal energy of the hot spot transformed into kinetic energy of the cold shell. Using $P \approx 2nT$, we can define the Lawson parameter $P\tau$ as:

$$P\tau > \frac{24}{\epsilon_\alpha}\frac{T^2}{\langle\sigma\nu\rangle} = f(T) \tag{1.14}$$

and the overall ignition parameter χ

$$\chi \equiv \frac{P\tau}{f(T)} > 1. \tag{1.15}$$

This is a general argument, valid for all ignition approaches, ICF and magnetic confinement fusion. The ideal ignition conditions are those for which χ has a minimum in the $P\tau$-T plane, as represented in figure **??**. The minimum is for $P\tau = 9$ atm·s at a temperature ~ 13 keV. To reach such a high hot spot temperature, high implosion velocity is required and therefore a thin shell. Hydrodynamic simulations of shell implosion show that thin shell break up in flight, due to Railegh-Taylor (RT) instabilities. Is therefore necessary to use thicker shells, reducing the implosion velocity. Figure **??** shows the Lawson parameter and temperature at which the National Ignition Facility will operate. The energy released in a ICF implosion is obtained

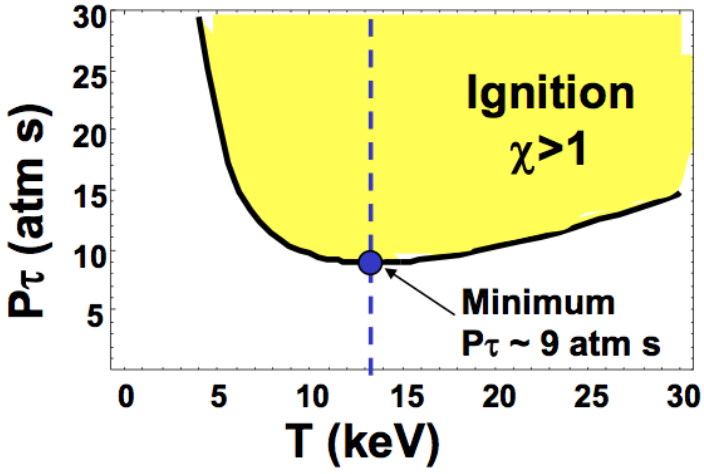

Figure 1.4: χ **curve in the** $P\tau$-T**, plane. Courtesy of prof. R. Betti.**

calculating the fuel burn fraction ϕ [**?**]. The reaction rate is given by:

$$\frac{dn}{dt} = n_D n T \langle \sigma v \rangle. \tag{1.16}$$

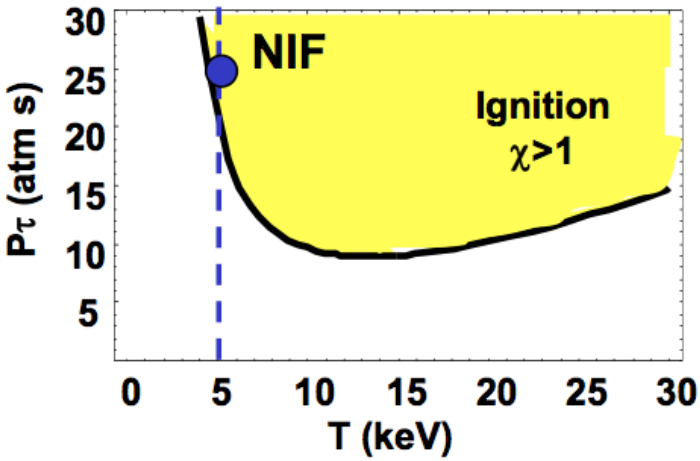

Figure 1.5: **Nif operating point. Courtesy of prof. R. Betti.**

Considering an identical concentration of D and T ions, and defining the burn fraction $\phi = 2n/n_0$ we have:

$$\frac{d\phi}{dt} = \frac{n_0}{2}\left(1-\phi^2\right)\langle\sigma v\rangle. \tag{1.17}$$

Assuming $\langle\sigma v\rangle$ to be approximately constant during the burn process, we can integrate eq. **??** obtaining:

$$\frac{\phi}{1-\phi} = \frac{n_0\tau}{2}\langle\sigma v\rangle. \tag{1.18}$$

The burning process remain efficient during the stagnation time, before the rarefaction wave, propagating inwards at the speed of sound, moves for a fraction of the fuel radius r. After that, the fuel density becomes too low to sustain efficient nuclear burn. By assuming $\tau \approx \frac{r}{4c_s}$, equation **??** becomes

$$\frac{\phi}{1-\phi} = n_0\langle\sigma v\rangle\frac{r_{HS}}{8c_s}. \tag{1.19}$$

Being the ratio of the fusion reactivity to the sound speed constant for optimal fuel burn temperature of 20-40 keV, we can find an approximated

solution for the burn fraction:

$$\phi = \frac{\rho r}{H_B + \rho r}, \tag{1.20}$$

With the burn parameter

$$H_B = \frac{8 c_s m_f}{\langle \sigma v \rangle}. \tag{1.21}$$

The burn parameter H_B has the dimension of an areal density and assumes values ≥ 6 g/cm^2. This implies that, to burn a fraction $\sim 30\%$ of fuel, the required areal density is:

$$\rho r \simeq 3 g/cm^2, \tag{1.22}$$

corresponding to a fuel density of 300 g/cm^3.

1.4 Alternative Ignition schemes

With the development of Chirped Pulse Amplification (CPA) technique [**?**], higher laser intensities became attainable. Laser intensities above the relativistic threshold $I \sim 10^{18}$ W/cm^2 opened a all new vista on laser plasma interaction. These laser pulses are characterized by high energy ($\sim 10^2 J$) and ultra short pulse duration ($\leq 1ps$). The power of a single laser shot may exceed few petaW, and the very short duration allows to deliver the energy faster than the typical hydrodynamic temporal scale length. In this context develops the idea of Fast Ignition (FI) [**?**] [**?**] as alternative approach to ICF. FI consists in the separation of the compression and ignition stages by using a secondary, ultra-intense laser pulse, to ignite the compressed DT fuel. The ultra-intense laser pulse generates an energetic particle particle beam, the ignitor beam, constituted by electrons or protons, that transports a substantial fraction of the laser pulse energy from the laser-plasma interaction region to the compressed core. The reason for an alternative ignition method resides in the very tight constraints imposed by the CHS approach. The requirements for perfectly symmetrical implosion, low adiabat, fuel assembly and minimization of hydrodynamic instabilities, leading to mixing of the cold shell material with the hot spot, quenching the ignition, can be

dramatically loosen in FI. The Fast Ignition fuel assembly is defined as "isochoric" and characterized by constant radial density ($\sim 300 g/cm^2$). The energy released by the ignitor beam is deposited in the core generating a lateral hot spot, from which the thermonuclear explosion takes place. The only requirement resides in a sufficiently high areal density of the compressed core ($\sim$ 0.5 g/cm^2), to guarantee large α particle energy deposition in the DT fuel. The Fast Ignition approach to ICF can be easily schematized in three fundamental steps:

1. Fuel compression by laser pulses.

2. Ignition at peak compression by a short, high intensity laser pulse.

3. Burn of the compressed fuel.

The separation of compression and ignition stages allows to reduce the driver energy leading to higher energy gain. Moreover, the removal of central hot spot creation condition allows to explore different fuel assembly geometries, such as cylindrically compressed fuel [**?**].

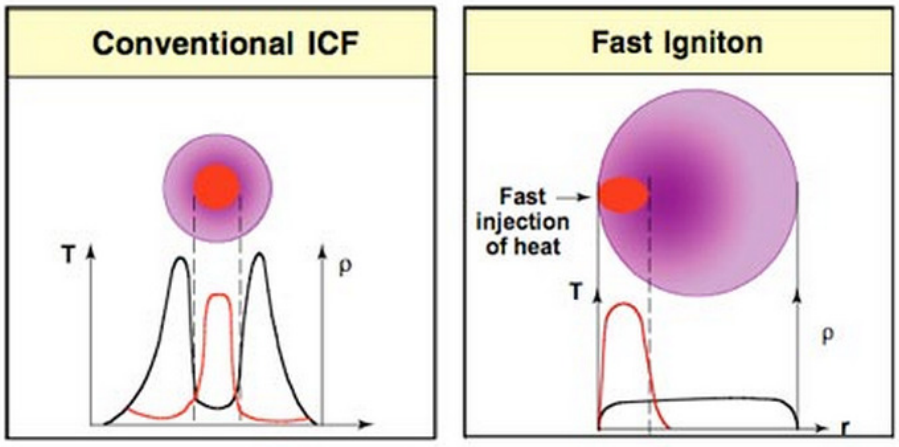

Figure 1.6: **Fuel assembly for CHS ignition (isobaric assembly), and Fast Ignition (isochoric assembly). Courtesy of Lawrence Livermore National Laboratory.**

Atzeni [?] derived the ignition conditions for areal density and lateral hot spot temperature $\rho R_h \geq 0.5$ g/cmcm^2 and $T_h \geq 12$ keV. The ignition energy relative to these values is :

$$E_{ign} = 72/\hat{\rho}^2 kJ. \tag{1.23}$$

Where $\hat{\rho}$ is the density in unit of 100 g/cm^3. This energy has to be released in a small portion of the compressed fuel, or radius $r \leq R_h$ in a time $t \leq t_c = R_h/cs$. The ignition windows were calculated by Atzeni [?] using the 2-D hydrodynamic code DUED, giving the minimum ignition requirements for energy, power and intensity as follows:

$$E_{ign} = 140\hat{\rho}^{-1.85} kJ, \tag{1.24}$$

$$W_{ign} = 2.6 \times 10^{15} \hat{\rho}^{-1} W, \tag{1.25}$$

$$I_{ign} = 2.4 \times 10^{19} \hat{\rho}^{0.95} W/cm^2. \tag{1.26}$$

Assuming a compressed fuel density $\rho = 300$ g/cm^3, we need to deliver ~ 18 kJ in $t \sim 20ps$, corresponding to a $\sim 7 \times 10^{19}$ W/cm^2 beam intensity.

1.4.1 Cone guided fast ignition

However, several are the issues related to the FI approach. One of the main problems is that the ultra-high intensity laser pulse has to be focused on a distance $\leq 100\mu$m, in order to avoid that the intrinsic divergence of the generated fast electrons reduces the beam intensity, releasing their energy over a wide area in the compressed fuel, with consequent reduction of the fuel temperature below the ignition threshold. The ignitor pulse path is indeed obstructed by a large cloud of low density plasma, as result of DT mass ablation during the compression stage. As addressed in Chapter 2, an electromagnetic wave cannot propagate into a plasma which density is higher than a critical value, depending on the wave frequency, whose is orders of magnitude below the plasma density at a distance $\leq 100\mu$m from the compressed core. To avoid this problem, targets with cone-in-shell geometry have

been proposed [?](see Figure ??). The function of the cone is to provide a clear path to the UHI pulse, that can therefore be focused close to the compressed core. At the same time, hydrodynamic simulations [?] demonstrate that is possible to achieve the compressed areal density requirements for FI in cone-in shell geometry.

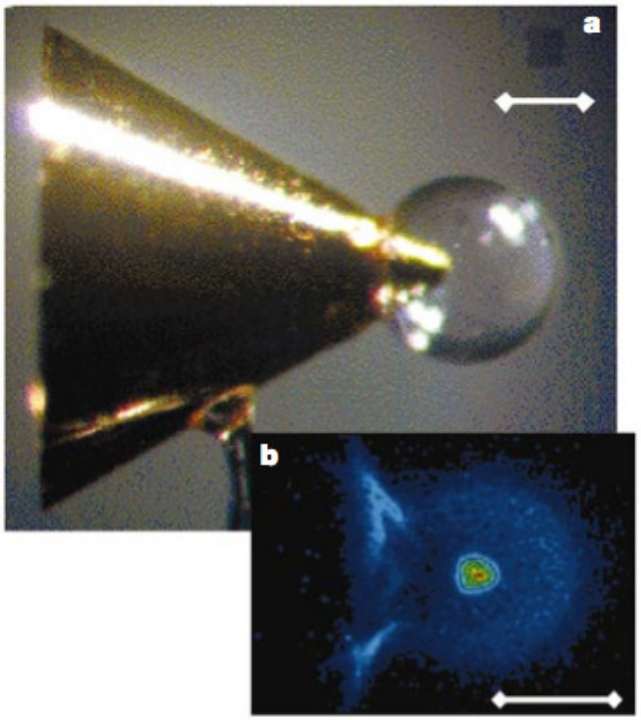

Figure 1.7: **(a) The reentrant cone target used by Kodama et al. [?]. The gold cone was attached to a CD shell of 500 μm diameter and 7 μm wall thickness. (b) An x-ray image showing the imploded core plasma at the cone tip.**

The laser pulse energy is converted at the cone tip in a fast electron beam, which subsequently propagates into the compressed fuel depositing its energy, this approach is called "electron fast ignition". The introduction of a cone in the target geometry allowed also to explore different FI methods like ion fast ignition: the laser energy is converted into an energetic ion beam, produced on a thin layer positioned inside the cone. The ion beam subse-

quently freely propagates inside the cone and is focused on the compressed core, releasing its energy. In general, only particles within a specific energy range are suitable for FI. Indeed, particle range in matter, measured in unit of areal density (g/cm^2), is dependent on the particle energy. In order to match the compressed core areal density $\sim$ 1.2 g/cm^2, the particle range in matter has to be of the same amount, corresponding for fast electron to an energy window of 1-2 MeV and for protons 3-18 MeV.

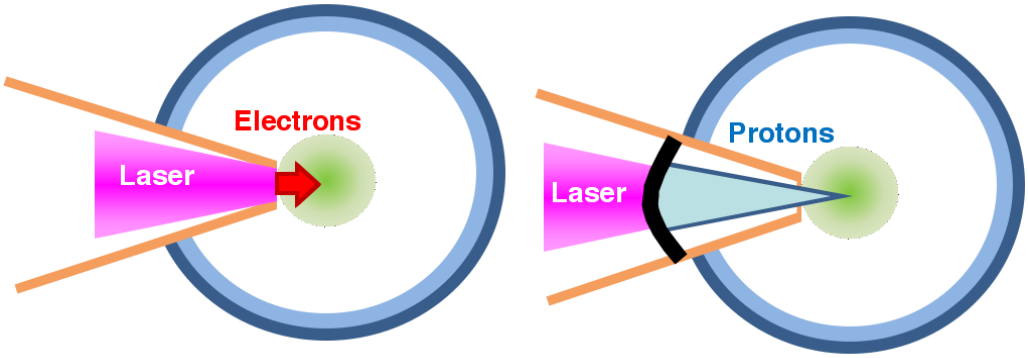

Figure 1.8: **Fast electron (left) and proton fast ignition concepts in re-entrant cone geometry.**

In order to meet the requirements for the ignitor beam, a deeper understanding of UHI laser produced fast particle beams generation and transport and laser to particle energy conversion efficiency, as well as fast electron and proton energy spectrum, is required. In this work we will attempt to address some of these issues.

1.5 Outline of the thesis

This work explores the physics of fast electron transport and fast ion generation for Fast Ignition research. The experiments were conducted at Jupiter Laser Facility,Titan Target Area at Lawrence Livermore National Laboratory and at Tcubed Laser, Center for Ultrafast Optical Science (CUOS), University of Michigan. the experiments were modeled with Lsp hybrid-code.

Chapter 2 describes the Physics of Laser- Plasma interaction for underdense and overdense plasmas, describes the physics of fast electron generation and transport and ion acceleration.
Chapter 3 describes the capabilities of Titan and Tcubed lasers, the x-ray diagnostics for fast electron transport experiments and the diagnsotics related to ion acceleration.
Chapter 4 shows the experimental results and modeling for fast electron transport in Warm Dense Matter, with particular attention to the collective effects on transport in plasmas at the Fermi temperature. It also introduces a study on fast electron transport in counter directed resistivity gradients that will be subject of a future publication.
Chapter 5 Is the transcription of a submitted paper describing the experimental results obtained at Tcubed laser on improved Laser-to proton energy conversion efficiency in reduced mass targets (RMT), as function of the target isolation. The experiment is modeled with Lsp hybrid code.
Chapter 6 summarizes the results and implications for fast electron and proton fast ignition.

Chapter 2

The physics of laser-plasma interaction

2.1 Single electron in a laser field

We start our discussion on laser plasma interactions by treating the motion of a single electron in a laser field. A focused laser beam can be approximated locally by a linearly polarized wave of amplitude E as:

$$\mathbf{E}\left(\mathbf{x},\mathbf{t}\right)=\mathbf{E}\mathbf{e}^{\mathbf{ikx-i\omega t}}, \tag{2.1}$$

$$\mathbf{B}=\frac{\mathbf{k}}{\omega}\times\mathbf{E}, \tag{2.2}$$

and its relative intensity **I**in vacuum defined by the cycle-averaged modulus of the Poynting vector **S**,

$$\mathbf{I}=|\mathbf{S}|=\mathbf{c^2}\epsilon_\mathbf{0}|\langle\mathbf{E}\times\mathbf{B}\rangle|=\frac{\mathbf{1}}{\mathbf{2}}\mathbf{c}\epsilon_\mathbf{0}\mathbf{E^2}. \tag{2.3}$$

Classically, the motion of a free electron of mass m under a laser field is governed by the Lorentz force:

$$\frac{d}{dt}(m\mathbf{v})=-\mathbf{e}(\mathbf{E}+\mathbf{v}\times\mathbf{B}). \tag{2.4}$$

This expression can be easily corrected for relativistic electron energies by multiplying the mass by the relativistic γ factor. In general a solution $\mathbf{x(t)}$ is highly non-linear, depending both on electric and magnetic field. For non relativistic laser intensities the magnetic field can be disregarded, being its magnitude $B = E/v_{phi}$ where $v_{\omega/k}$ is the phase velocity. We therefore find :

$$\mathbf{v}(\mathbf{x},\mathbf{t}) = -\mathbf{i}\frac{\mathbf{e}}{\mathbf{m}\omega}\mathbf{E}\mathbf{e}^{\mathbf{ikx-i\omega t}}, \tag{2.5}$$

$$\delta(\mathbf{x},\mathbf{t}) = \frac{\mathbf{e}}{\mathbf{m}\omega^{\mathbf{2}}}\mathbf{E}\mathbf{e}^{\mathbf{ikx-i\omega t}}, \tag{2.6}$$

where $\mathbf{v}(\mathbf{x},t)$ and $\delta(\mathbf{x},\mathbf{t})$ are respectively the electron oscillation velocity and the periodic displacement. An important quantity for future discussions is the cycle-averaged oscillation energy W:

$$W = \frac{1}{4}m\mathbf{v}^2 = \frac{e^2}{4m\omega^2}\mathbf{E}^2, \tag{2.7}$$

and for relativistic velocities:

$$W = mc^2\left\{\left[1+\frac{1}{2}\left(\frac{eA}{mc}\right)^2\right]^{1/2} - 1\right\}, \tag{2.8}$$

where A is the vector potential amplitude. Following the argument in [**?**], if we consider $\mathbf{E}$ slowly varying in space, such that $|(\delta\nabla)E| \ll E$, which is true at non-relativistic laser intensities. For simplicity we consider a standing wave, in this case the oscillation W energy in equation **??** is a function of the position only, for slow drifting of the electron from one point to another. In this case, the oscillatory energy in 2 differenct positions a and b will be different $W(a) \neq W(b)$. The difference in energy has to be related to the work performed by the laser field on the particle, increasing its kinetic energy. Indicating the velocity of the electron oscillation center as v_0, the energy conservation writes as:

$$E_{kin} + W = \frac{1}{2}m\mathbf{v}_0^2 + \frac{e^2}{4m\omega^2}\mathbf{E}^2 = const, \tag{2.9}$$

with W representing effectively a potential energy and taking its negative gradient we obtain a force $\mathbf{f}_p$:

$$\mathbf{f}_p = -\nabla W = -\nabla \frac{e^2}{4m\omega^2}\mathbf{E}^2, \tag{2.10}$$

called ponderomotive force, and W represents the ponderomotive potential.

2.1.1 The ponderomotive force

The ponderomotive force can be considered as a generalization of the radiation pressure p_L, which was first calculated by James Clerk Maxwell considering a light beam impinging normally upon a surface of reflectivity R:

$$p_L = (1+R)\frac{I}{c}, \tag{2.11}$$

where I represents the intensity of the light. However, the expression for the ponderomotive force obtained in the previous section, as inverse gradient of a conservative field potential is much richer, since relates f_p to the gradient of the laser intensity and to the laser frequency. In this section we propose the classical perturbative approach to this problem. We decompose the motion $\mathbf{x}(t)$ of a charge q in the field of an electromagnetic wave, into a nearly periodic oscillatory component $\boldsymbol{\xi}(t)$ and the oscillation center component $\mathbf{x}_0(t)$:

$$\mathbf{x}(t) = \mathbf{x}_0(t) + \boldsymbol{\xi}(t) \quad \mathbf{v}(t) = \mathbf{v}_0(t) + \mathbf{w}(t), \tag{2.12}$$

where $\mathbf{v} = \dot{\mathbf{x}}$, $\mathbf{v}_0 = \dot{\mathbf{x}}_0$ and $\mathbf{w} = \dot{\boldsymbol{\xi}}$ respectively. Let's consider now the Lorentz force on a charge q in a monochromatic electromagnetic field:

$$m\frac{d\mathbf{v}}{dt} = q(\mathbf{E} + \mathbf{v} \times \mathbf{B}). \tag{2.13}$$

For oscillation amplitudes ξ small compared to the local wavelenght of the field, we can linearize the Lorentz equation and solve order by order:

$$m\frac{d\mathbf{v}}{dt} \simeq \left[\frac{\partial \mathbf{w}}{\partial t} + (\mathbf{v}_0\nabla)\mathbf{w}\right] = q\mathbf{E}(\mathbf{x}_0) + \mathbf{v}_0 \times \mathbf{B}(\mathbf{x}_0). \tag{2.14}$$

Assuming non-relativistic temperatures, the convective derivative $(\mathbf{v}_0\nabla)\mathbf{w}$, as well as the force term $\mathbf{v}_0 \times \mathbf{B}(\mathbf{x}_0)$, become negligible and a solution for $\mathbf{w}(t)$ can be found as:

$$\mathbf{w}(t) = i\frac{q}{m\omega}\mathbf{E}(\mathbf{x}_0). \tag{2.15}$$

In the next order we can calculate the oscillation center velocity $(\mathbf{v}_0(t)$. The ponderomotive force is the time derivative of this quantity:

$$f_p = m\frac{d\mathbf{v}_0}{dt} = q\left[\mathbf{E}(\mathbf{x}_0 + \boldsymbol{\xi}(t)) + \mathbf{w}(t) \times \mathbf{B}(\mathbf{x}_0)\right]_0, \tag{2.16}$$

where the subscript "0" indicates that the terms osciallating at 2ω will be for the moment neglected. Being $\boldsymbol{\xi}$ a quantity of the second order, we can perform a Taylor expansion of $\mathbf{E}(\mathbf{x}_0 + \boldsymbol{\xi}(t))$:

$$\mathbf{E}(\mathbf{x}_0 + \boldsymbol{\xi}(t)) = \mathbf{E}(\mathbf{x}_0) + \boldsymbol{\xi} \cdot \nabla\mathbf{E}|_{\mathbf{x}_0} + ... \tag{2.17}$$

Suppressing the terms oscillating at 2ω and using $\boldsymbol{\xi} = i\mathbf{w}/\omega$ and $\mathbf{B} = -i/\omega\nabla \times \mathbf{E}$, we obtain:

$$\mathbf{f}_p = -\frac{q^2}{m\omega^2}[(\mathbf{E}\nabla)\mathbf{E} + \mathbf{E} \times \nabla \times \mathbf{E}], \tag{2.18}$$

or

$$\mathbf{f}_p = -\frac{q^2}{2m\omega^2}\nabla\mathbf{E}^2. \tag{2.19}$$

Averaging over a laser period we finally obtain:

$$\mathbf{f}_p = -\frac{q^2}{4m\omega^2}\nabla\mathbf{E}^2. \tag{2.20}$$

Therefore, f_p can be considered as the inverse gradient of a quantity $textbfW_p$ called ponderomotive potential. It is possible to relate the expression for f_p

?? to the electromagnetic wave intensity I by using the definition exposed in eq ??. Is therefore possible to relate the ponderomotive force f_p to the gradient of the laser intensity $f_p \propto \nabla I$.

2.2 Laser-plasma interaction and related effects

2.2.1 Introduction

We start our discussion on the interaction of electromagnetic waves with plasmas by introducing a fundamental plasma parameter, the plasma frequency ω_p. Let's consider a plasma initially in equilibrium, with completely stationary ions and electrons positioned in the minima of the electrostatic potential. A small dispacement in the position of the plasma electrons will create an electric field acting as a restoring force. Once free to move, the energy stored in the electric field will be transformed into kinetic energy of the electrons, accelerated towards the original position. The kinetic energy acquired by the electrons will force them to undergo periodic oscillations around the potential minima. These kind of oscillations are called "Langmuir oscillations", and their proper frequency is the plasma frequency ω_p:

$$\omega_p = \sqrt{\frac{n_e e^2}{m\epsilon_0}}, \tag{2.21}$$

where m is the electron mass. Let's now consider a high frequency electromagnetic wave propagating in a plasma. From the Maxwell equations and the continuity equation we can obtain the dispersion relation:

$$\omega^2 = c^2 k^2 + \omega_p^2. \tag{2.22}$$

The dispersion relation **??** has several interesting implications. In particular if we consider the group velocity

$$\frac{\partial \omega}{\partial k} = \frac{c^2}{1 + \omega_p^2 / c^2 k^2}, \tag{2.23}$$

we can see at at very low frequencies ($ck \ll \omega_p$), only constant frequancy waves with $\omega = \omega_p$ can propagate. Being $\partial\omega/\partial k = 0$, no energy or information can be transported in the plasma. At very high frequencies instead $\partial\omega/\partial k = c$, and the wave propagates as in vacuum. The plasma frequency therefore, determines the propagation of electromagnetic waves in the plasma. it can be seen as the capability of the plasma electrons to respond to an electromagnetic stimulation. This can be more clearly seen considering again the dispersion relation **??**

$$\omega^2 - \omega_p^2 = k^2 c^2, \tag{2.24}$$

which implies that an electromagnetic wave with frequency $\omega < \omega_p$,cannot propagate in a plasma, having an imaginary wave vector k. Indeed, if we solve this equation for the wave vector k we obtain:

$$k = \frac{\left(\omega^2 - \omega_p^2\right)^{1/2}}{c}, \tag{2.25}$$

which assumes imaginary values for $\omega < \omega_p$. The wave is then exponentially attenuated within a skin depth defined as

$$\delta = \frac{c}{\left(\omega^2 - \omega_p^2\right)^{1/2}}. \tag{2.26}$$

The electron density corresponding to this cutoff is called critical density and is given by:

$$n_c = \frac{m\omega^2}{\epsilon_0 e^2} \tag{2.27}$$

or in practical units:

$$n_c = \frac{1.1 \times 10^{21}}{\lambda^2} cm^{-3}. \tag{2.28}$$

Depending on the intensity of electromagnetic radiation, several are the mechanism that could contribute to the wave damping in regions where the plasma density is above n_c. For low intensities the loss mechanism is related to collisional damping of the wave, due to the excitation of electrons that subsequently lose their energy by collisions with the plasma ions. For higher intensities various absorption mechanisms collisional and collisionless, take place. We will address some of these phenomena, important for the generation of hot electrons in Chapter 2. From equation **??** follows that the critical density n_c depends only on the laser frequency/wavelenght. This is in general not true. In case of very high laser intensities indeed (the so-called relativistic intensity), the motion of an electron in the laser field becomes relativistic and the electron mass must be corrected by the relativistic gamma factor γ :

$$n_{cRel} = \frac{\gamma m \omega^2}{\epsilon_0 e^2} = \gamma \frac{1.1 \times 10^{21}}{\lambda^2} cm^{-3}. \tag{2.29}$$

As a consequence, in relativistic laser plasma interaction, the laser light can propagate in denser regions, due to the higher mass, and therefore higher inertia, of the plasma electrons. The iso-surface with plasma density $n_e = \gamma n_c$ is called critical surface and represents the region where the majority of the laser energy is absorbed. It is possible to introduce a very useful dimensionless parameter in relativistic laser plasma interaction: the normalized momentum a_0, defined as:

$$a_0 = \frac{p_{osc}}{mc} = \frac{\gamma v_{osc}}{c} = \frac{eE}{mc\omega} = \sqrt{\frac{I\lambda^2(\mu m)}{1.37 \times 10^{18}(W/cm^2)}}. \tag{2.30}$$

The normalized momentum a_0 discriminates between non relativistic ($a_0 < 1$) and relativistic ($a_0 > 1$) laser plasma interaction. Given a certain laser intensity I, the value of γ can be easily calculated as $\gamma = \sqrt{1 + a_0^2}$ for circularly polarized light, or $\gamma = \sqrt{1 + a_0^2/2}$ for linearly polarized light. The derivation of these useful relations gives more insights on the physics describing the motion of a single particle in an electromagnetic field. Let's consider the Lagrangian for a charge (charge e and mass m) in an electromagnetic field

as exposed in the classic work by Landau and Lifshitz [**?**]

$$L(\mathbf{v},\ \mathbf{r}, t) = -mc^2\sqrt{1-\frac{v^2}{c^2}} + \frac{e}{c}\mathbf{A}\cdot\mathbf{v} - e\phi \tag{2.31}$$

where $\mathbf{A}(\mathbf{r}, t)$ and $\phi(\mathbf{r}, t)$ are the vector and scalar potentials of the eld respectively. Then the canonical momentum $\mathbf{P}$ is dened as

$$\mathbf{P} = \frac{\partial L}{\partial \mathbf{v}} = \frac{m\mathbf{v}}{\sqrt{1-\frac{v^2}{c^2}}} + \frac{e}{c}\mathbf{A} = \mathbf{p} + \frac{e}{c}\mathbf{A}, \tag{2.32}$$

where $\mathbf{p} = \gamma m\mathbf{v}$ is the momentum of the electron. Knowing from Lagrangian mechanics that

$$\frac{d}{dt}\left(\frac{\partial L}{\partial \dot{x}}\right) - \frac{\partial L}{\partial x} = 0 \tag{2.33}$$

we can write the equation for mechanical momentum as [**?**]

$$\frac{d}{dt}(\gamma m\mathbf{v}) = \frac{e}{c}\left(\nabla\mathbf{A}\cdot\mathbf{v} - \frac{\mathbf{A}}{dt}\right) - e\nabla\phi, \tag{2.34}$$

which is the expression for the usual Lorentz force if we remember that $E = -\nabla\phi - \frac{1}{c}\frac{\partial \mathbf{A}}{\partial t}$ and $\frac{d\mathbf{A}}{dt} = \frac{\partial \mathbf{A}}{\partial t} + (\mathbf{v}\cdot\nabla)\mathbf{A}$. We now decompose our quantities in longitudinal and perpendicular components, and we consider our variables only dependent on z or $\mathbf{A} \equiv \mathbf{A}(z, t) \equiv (A_\perp, A_z)$, $\phi \equiv \phi(z, t)$ and $\mathbf{r} \equiv (r_\perp, z)$. Noting that

$$(\nabla\mathbf{A}\cdot\mathbf{v})_j = \sum_{i=1}^{3}\left(\frac{\partial A_i}{\partial r_j}\right)v_i \tag{2.35}$$

we obtain the following relations for parallel (z) and perpendicular (r) directions

$$\frac{d}{dt}\left(\gamma m v_\perp + \frac{e}{c}A_\perp\right) = 0. \tag{2.36}$$

$$\frac{d}{dt}(\gamma m v_z) = eE_z + \frac{e}{c}\left(v_\perp\frac{\partial A_\perp}{\partial z}\right) \tag{2.37}$$

This shows that in one dimensional case, canonical momentum is conserved in the perpendicular direction. Integrating equation **??** and taking $v_\perp(0) =$

$A_\perp(0) = 0$ we can reduce the equation **??** in

$$\frac{d}{dt}\left(\gamma m v_z\right) = eE_z - \frac{e^2}{2\gamma mc^2}\frac{\partial A_\perp^2}{\partial z}. \tag{2.38}$$

The second term on the right hand side represents the relativistic ponderomotive force on the charge particle. The energy conservation equation can be written as:

$$\frac{d}{dt}\left(\gamma mc^2\right) = e\mathbf{E}\cdot\mathbf{v} = eE_z v_z + \frac{e^2}{2\gamma mc^2}\frac{\partial A_\perp^2}{\partial t} \tag{2.39}$$

Considering now electromagnetic radiation (ω, k), we normalize the fundamental quantities as: $t \to \omega t$, $z \to kz$, $p \to p/mc$, $v \to v/c$, $A \to eA/(mc^2)$, $E \to eE/(mc\omega)$. This allows us to write the relativistic electron dynamics in a-dimensional form :

$$\frac{d}{dt}(\gamma v_\perp - A_\perp) = 0 \tag{2.40}$$

$$\frac{d}{dt}(\gamma v_z) = -E_z - \frac{1}{2\gamma}\frac{\partial A_\perp^2}{\partial z} \tag{2.41}$$

$$\frac{d\gamma}{dt} = -E_z v_z + \frac{1}{2\gamma}\frac{\partial A_\perp^2}{\partial t}. \tag{2.42}$$

For $E_z = 0$ and plane electromagnetic wave $A_\perp = A_\perp(t - z)$, the parallel momentum equation and energy conservation equation can be combined to give another constant of motion as

$$\frac{d}{dt}(\gamma - p_z) = \frac{d}{dt}[\gamma(1 - v_z)] = 0. \tag{2.43}$$

Redefining the constant of motion as $\gamma - p_z) = \Delta$ and combining it with $\gamma^2 = 1 + p_z^2 + p_\perp^2$ we obtain,

$$p_z = \frac{1 - \Delta^2 + p_\perp^2}{2\Delta}, \tag{2.44}$$

from conservation of canonical momentum in the perpendicular direction results $p_\perp = A_\perp$, it is possible to then to calculate for an electron initially at

rest ($\Delta = 1$) and linearly polarized light ($A_\perp = a_0 \cos(t - z) = a_0 \cos\tau$):

$$p_z = \frac{a_0^2}{4}(1 + \cos 2\tau) \tag{2.45}$$

$$p_\perp = a_0 \sin\tau. \tag{2.46}$$

From the above equation appears clear that the longitudinal momentum of the electron in presence of linearly polarized light has a secular component and a rapidly oscillating (2ω) component. This last property is characteristic of linearly polarized light. For circular polarized light, $A_\perp = a_0/\sqrt{2}(\cos\tau x \pm \sin\tau y)$, we obtain $A_\perp^2 = const$ and no 2ω oscillations are present. Therefore for circular polarization we obtain:

$$p_z = \frac{a_0^2}{4} \tag{2.47}$$

$$p_z = \frac{a_0}{\sqrt{2}} \cos\tau \tag{2.48}$$

$$p_z = \frac{a_0^2}{\sqrt{2}} \sin\tau \tag{2.49}$$

Considering a Neodimium (Nd) based laser system ($\lambda \sim 1\mu$m), the relativistic intensity occurs for $I \geq 10^{18}$W/cm^2 ($a_0 = 1$). The When $a_0 > 1$, the electron motion in the laser field is no longer determined only by the action of E. The B field action on the particle becomes non negligible and the electron is accelerated longitunally by the Lorentz force $-e\mathbf{v} \times \mathbf{B}$. This leads to a very important energy absorbtion machanism called $J \times B$ heating, which will be diffusely treated in section **??**.

From the above discussion, it comes natural to distinguish between two main domains of laser plasma interaction: interaction with underdense ($n_e < n_c$) and overdense plasma ($n_e > n_c$).

2.3 Interaction with underdense plasma

Ultra-intense, short pulse lasers are characterized by pulse lengths ≤ 1 ps, much faster than typical plasma expansion time scale ($\propto 100$ ps). This

would imply, in principle, that short pulse lasers only interact with overdense plasmas. This is not usually the case. Typical short laser pulses are indeed composed by a long ($\sim ns$), low intensity pedestal, followed by the short, high intensity pulse. The intensity contrast ratio between the short pulse and the pedestal can be as high as 10^7-10^8, nevertheless, for ultra-relativistic laser pulses, the intensity of the pedestal can be of the order of few times 10^{12} W/cm^2. This intensity is high enough to create a plasma expanding into vacuum approximately at the speed of sound c_s. The scale length of the plasma can be defined as $c_s\tau$, where τ represents the length of the pedestal pulse. The short pulse, therefore, before reaching the relativistic critical surface propagates into an underdense plasma, and can be modified by non-linear processes, depending on the pulse own properties.

2.3.1 Self-focusing

Laser self focusing is a non-linear process occurring in relativistic laser plasma interaction regime. It is possible to distinguish two different, and cooperating, non linear effect leading the beam to self focus: the relativistic and the ponderomotive self focusing [**?**][**?**].

Relativistic self-focusing

A fundamental quantity for the description of laser pulse propagation in a plasma is the refractive index n_{ref} which can be expressed as:

$$n_{ref} = \sqrt{1 - \left(\frac{n_e}{\gamma n_c}\right)}, \tag{2.50}$$

where n_e represents the plasma electron density and γn_c the relativistic critical density. The phase and group velocity of the propagating laser pulse are given by:

$$v_g = \frac{\partial \omega_L}{\partial k_L} = n_{ref} c \tag{2.51}$$

$$v_{phi} = \frac{\omega_L}{\partial k_L} = \frac{c}{n_{ref}}. \tag{2.52}$$

The laser intensity is generally not uniform, but higher in the central region of the pulse. For relativistic laser intensities, this implies that the electron in the central region will have higher relativistic mass γm, increasing the refractive index in the axial region. The laser light therefore, propagates slower in the center of the beam than in the wings. This causes the wavefront to bend, with concavity directed towards the propagation direction (see Figure **??**).

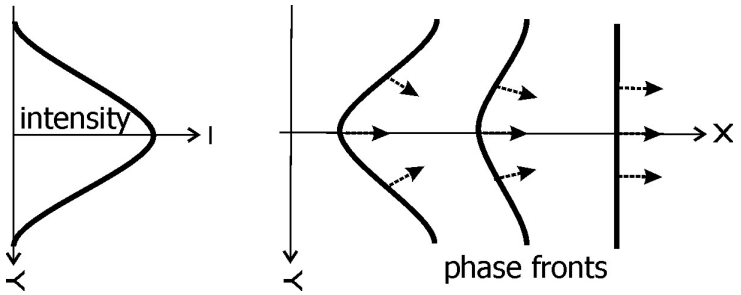

Figure 2.1: **Radial laser intensity lineout and correspondent wavefront bending, caused by the non uniform plasma refractive index. The wavefront surfaces are displayed for decreasing pulse power.**

The Poynting vector **S**, defined in equation **??**, is always perpendicular to the wavefront, and as result, the laser pulse focuses and the intensity further increases.

Ponderomotive self-focusing

Ponderomotive and relativistic self focusing share several common features. Indeed in both mechanisms are driven by the non uniformity of the laser pulse, and the configuration of the plasma refractive index as well as the wavefront can be described in the same way. The ponderomotive self focusing differs from the relativistic one by the mechanism that leads to the non uniformity of the plasma refractive index, which gradient points towards the light propagation axis. The ponderomotive force associated to the laser intensity gradient accelerates the plasma electrons away from the laser axis, reducing the plasma electron density and consequently, from equation **??** the refractive index.

2.3.2 Inverse Bremmsstrahlung

At relatively low laser intensities (10^{12}-10^{15} W/cm^2), one of the predominant machanisms of laser energy absorption is plasmas is represented by collisions with plasma ions. In the so-called inverse bremmsstrahlung process the plasma electrons absorb laser energy and a plasma heating process takes place. The electrons gain net energy being decoupled from the oscillatory laser field by collisions with the plasma ions. The electron-ion collision frequency is given by [**?**]:

$$\nu_{ei} = \frac{3 \times 10^{-6} Z^2 n_e \ln(\Lambda)}{T_e^{3/2}} s^{-1}, \tag{2.53}$$

where $T_e \simeq 1/2m\mathbf{v}^2$ is the electron temperature with $|v| = eE_L/m\omega_L$, the oscillation velocity of the electron in the laser field. From **??** we can observe that the collision frequency increases with the plasma density and ion charge, and decreases with temperature. As consequence, for very high laser intensities, the collision frequency drops due to the very high electron oscillation energy. The collisional absorption remains substantial in case of heavy (high Z) materials, due to the quadratic dependence on Z.

2.4 Interaction with overdense plasma

For very high laser intensities ($> 10^{17}$ W cm^2), the energy carried by the pulse is mainly absorbed at the critical or relativistic critical surface. The absorption processes are mainly collisionless, since the collision frequency drops dramatically at very high electron temperatures. These processes lead to the formation of high energetic electron beams, that can propagate through the solid material, far beyond the critical surface, and deposit the laser energy deeper in the target material.

2.4.1 Resonance absorption

Resonance absorption is a nonlinear laser plasma process that takes place when a component of the laser electric field is parallel to the plasma density

gradient $\mathbf{E}_L \cdot \nabla \mathbf{n} \neq 0$. This condition is fulfilled, for example, for p-polarized light and oblique incidence. The laser light will be specularly reflected at the critical density n_c, and the electric field component tunnels through the critical density, driving a plasma wave in this region.

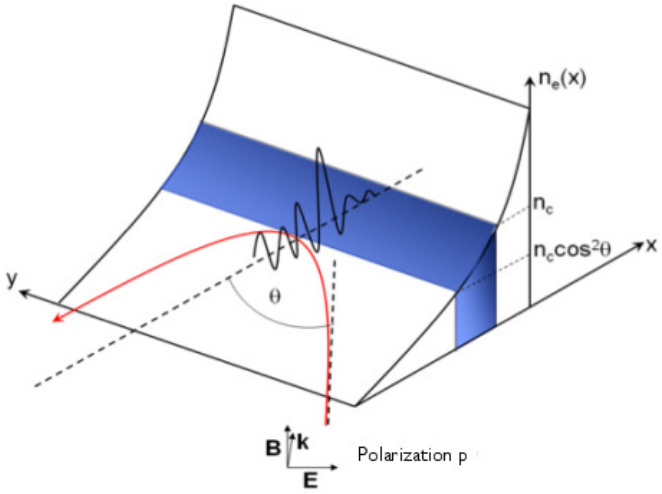

Figure 2.2: **Schematic of the resonant absorption mechanism [?]. The laser light is reflected at the critical density and a Langmuir wave is driven by the electric field component parallel to the density gradient.**

The Langmuir wave generated grows for a number of laser cycles and is damped either by collisions (at low intensities) or by electron trapping and wavebreaking (high intensities), heating the plasma electrons up to hundreds of keV. Resonant absorption is important for large plasma scale lengths, condition which can be summarized by $kL \gg 1$, where k is the light wave vector and $L^{-1} = (1/n_e)dn_e/dx$. The absorption fraction ha a self-similar dependence on the parameter $\xi = (kL)^{1/3} \sin\theta$, where θ is the angle of incidence. The angular absorption $\phi(\xi)$ in this limit is given by

$$\phi(\xi) \simeq 2.3\xi e^{\frac{-2\xi^2}{3}}, \tag{2.54}$$

and the fractional absorption is given by

$$\eta_{ra} = \frac{1}{2}\phi^2(\xi). \tag{2.55}$$

The hot electrons generated in this process have a hot Maxwellian tail superimposed to initial background electron temperature. Numerical (PIC) simulations can provide scalings for the hot electron component of the spectrum [**?**]:

$$T_{hot} \approx 14[T_{keV} I_{16} \lambda_{\mu m}^2]^{1/3} keV, \tag{2.56}$$

where T_{keV} is the electron temperature in KeV, I_{16} the laser intensity in units of 10^{16} W/cm^2 and $\lambda_{\mu m}$ is the wavelength in unit of μm.

2.4.2 Vacuum heating

Resonance absorption is strongly reduced in case of steep plasma density gradients. Indeed, even if a plasma wave ca be driven by the electric field component tunnelling the critical surface, the conditions of resonance impose for the amplitude of the electronic oscillation to be smaller than the plasma scale length $\simeq eE_L/m\omega^2 < L$. Therefore, no resonance absorption can take place with this configuration. Nonetheless, an acceleration mechanism occurs, still dependent on the $\mathbf{E}_L \cdot \nabla n \neq 0$ condition, and involving the electrons located at the boundary of the sharp boundary plasma-vacuum. The laser electric field can reach unperturbed the steep plasma gradient, accelerate the electrons into the vacuum over a semi-cycle on a distance larger than the thermal Debye sheath $\lambda_D = v_{te}/\omega_p$ and, re-accelerate them into the plasma in the subsequent semi-cycle. Beyond the critical density, the electric field is abruptly damped after a skin depth $\sim /\omega_p$,and the electrons decouples from the laser field, gaining net energy, and propagate into the target material, releasing their energy by collisions.

2.4.3 J × B heating

For laser light intensities exceeding the relativistic limit ($\sim 10^{18}$ W/cm^2), the motion of the electron in the laser field cannot be described solely by the action of the electric field. The $\mathbf{v} \times \mathbf{B}$ term of the Lorentz force becomes non negligible at relativistic quiver velocities, and accelerates the electrons in the laser propagation direction with $2\omega_L$ frequency. A free electron in a relativistic intense laser field, indeed, undergoes oscillations perpendicular and parallel to the wave vector $\mathbf{k}$, and the global trajectory is simply a composition of the two oscillations, as represented in figure **??**.

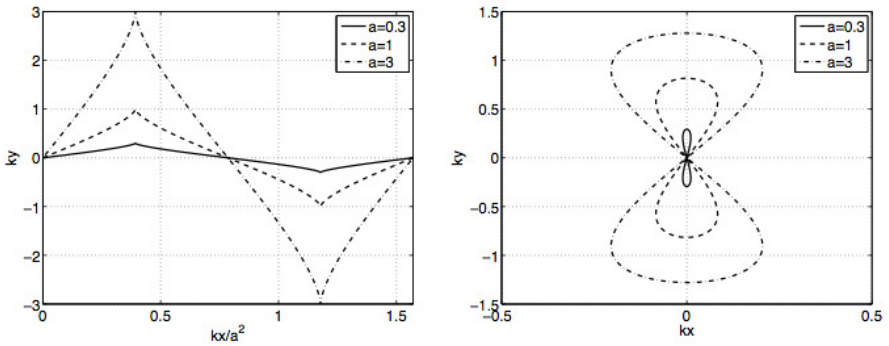

Figure 2.3: **Electron trajectory in a relativistic laser field. The motion is a composition of transverse and longitudinal oscillations, related respectively to the laser electric and magnetic field.**

In presence of a steep plasma gradient, the adiabaticity of the electron motion is broken, and a process, very similar indeed to the vacuum heating, occurs. The $\mathbf{E}$ and $\mathbf{B}$ fields penetrate within a skin depth, and, very similarly to the vacuum heating process, the longitudinally accelerated electrons decouple from the laser light and propagate in the supercritical plasma with net energy gain. This effect can be seen in an alternative way if we consider the ponderomotive force, accounting this time also for the terms oscillating at $2\omega_L$. Considering the electric field of the form $\mathbf{E} = E_L \sin(\omega_L t)$, from **??** we obtain:

$$\frac{e^2}{4m\omega^2}\nabla \mathbf{E}^2 = -\frac{m}{4}\frac{\partial}{\partial x} v_{osc}^2(x)(1 - \cos(2\omega_L t)). \tag{2.57}$$

The first term on the right hand side represents the secular ponderomotive force **??**, which can cause the steepening of the plasma density during the irradiation. The second, high frequency term, represents the oscillating electrostatic field that heats non-adiabatically the electrons. From PIC simulations of laser plasma interaction [**?**] is possible to obtain a scaling law for the fast electron temperature as result of $\mathbf{J} \times \mathbf{B}$ heating:

$$T_{hot} = 511\text{keV}\left(\sqrt{1 + \frac{I\lambda_{\mu m}^2}{\alpha 10^{18}\left(\text{W/cm}^2\right)}} - 1\right), \tag{2.58}$$

where α is a parameter dependent on the light polarization. For circularly polarized light $\alpha = 1.37$ and for linearly polarized light $\alpha = 2.8$. The expression for T_{hot} represents the ponderomotive potential, or the relativistic oscillation energy for an electron in a high intensity laser field.

2.5 Fast electron transport

In the previous sections, we treated, in a rather elementary way, the physics of laser-plasma interaction and laser energy absorption, and particularly the generation of suprathermal electrons, that can transport the laser energy far beyond the critical density, in the solid target material. In this section we focus our attention on the properties of the laser produced fast electron beams, and on the physics related to their propagation in the solid density plasma.

2.5.1 Fast electron conversion efficiency

In this work, the relevant laser intensities are above the relativistic limit, ranging from few times 10^18 to peak values of $\sim 10^{20}$ W/cm^2. At these intensities, a laser pulse can transfer a very significant amount of energy into fast electrons. This property, together with the fast electron energy distribution, determines many remarkable features of fast electron transport. The laser-to electrons energy conversion efficiency, indeed, in our intensity range of interest, ranges between the 20% and the 50% [**?**] [**?**] [**?**] [**?**], and scales

with the intensity approximately as $\sim I_{Las}^{0.3}$. In figure **??**, is represented the conversion efficiency versus laser intensity .

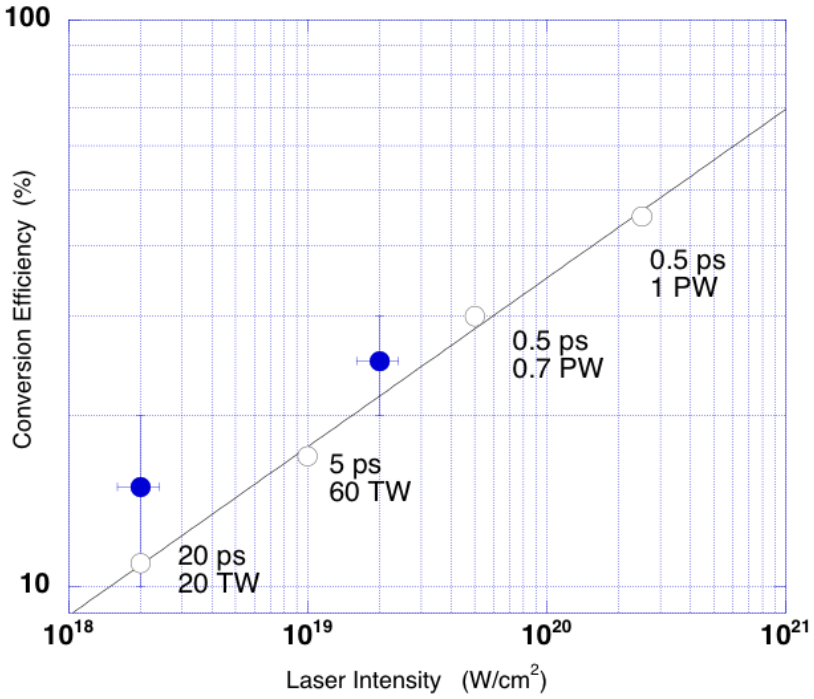

Figure 2.4: **Laser-to fast electrons conversion efficiency as function of the laser intensity** $(I\lambda^2)$**.** ***Open circles*** **LLNL (1**ω**)** [?]**,** ***filled circles*** **LULI (2**ω**)** [?] **.**

The uncertainty in the measurement of such quantity is nevertheless quite large, since is often related to the measurement of x-ray radiation produced by the fast electron beam when traveling through matter. In particular, Kα radiation spectroscopy has been systematically adopted, assuming that the cross-section for K-shell ionization is approximately constant over a wide range of electron temperatures and obatining quantitative estimations via Monte Carlo simulations, which do not include many important features of the fast electron transport such as collective effects.

2.5.2 Fast electron energy distribution

The determination of the fast electron energy distribution has been treated in numerous works [**?**] and still represents an open problem. Energy distribution functions can be expressed in the general form $f(E) \sim E^k \exp(E/T_{hot})$ where the exponent k can assume the values $k = 0, 0.5, 2$, determining the distribution type, and T_{hot} is a parameter that determines the shape of the distribution functions and is related to the fast electron temperature.

The first concept that needs to be clarified is that of temperature. In literature, the definition of fast electron "temperature" is sometimes quite confused, and, in some cases, should be substituted with "average energy". Distribution which can be associated to a temperature are for example the well-known Maxwellian distribution ($k = 1/2$) and its relativistic counterpart ($k = 2$). Recent PIC simulations of laser-plasma interaction show that the fast electron energy distribution can be described as an exponential ($k = 0$), or a composition of exponential distributions of the form

$$f(E) \approx \exp(-E/T_{hot}), \tag{2.59}$$

where T_{hot}, sometimes called "slope-temperature", has not to be confused with the fast electron temperature, but represents indeed the fast electron average energy. However for a Maxwellian distribution

$$f(E) \approx E^{1/2} \exp(-E/T_{hot}), \tag{2.60}$$

the parameter T_{hot} represents the actual fast electron temperature and is related to the average energy by $E_{ave} = 1.5T_{hot}$. In the relativistic regime, the Maxwellian is substituted by the 3D Juttner-type relativistic fast electron distribution [**?**]:

$$f(E) \approx E^2 \exp(-E/T_{hot}), \tag{2.61}$$

which is characterized by a much more extended tail at high temperatures. This influences the relation between T_{hot} and the average energy as $E_{ave} = 3T_{hot}$. Several measurements of fast electron energy spectrum, as well as LPI PIC simulations (see figure **??**), seem to point out the signature of a

two-temperature distribution function.

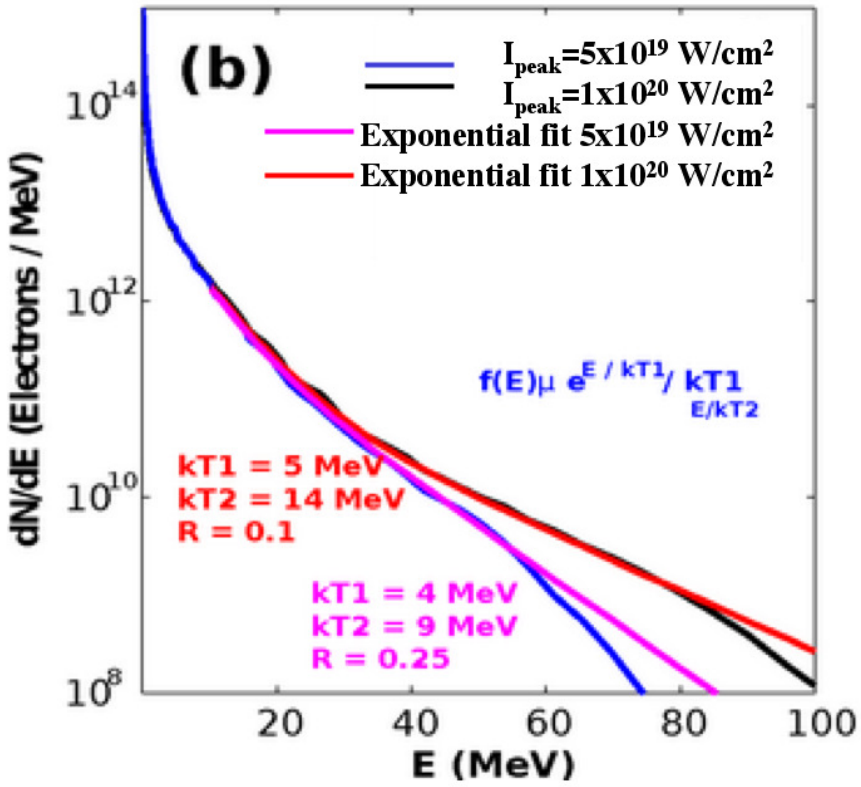

Figure 2.5: **Laser plasma interaction simulations performed with Lsp hybrid code at 5×10^{19} and 10^{20}W/cm^2 peak laser intensity. The results can be fitted with a two-temperature exponential distribution. Image courtesy of A. J. Link.**

However, it is very difficult to directly measure the fast electron distribution using, for example, electron spectrometer diagnostics, due to the large space charge fields generated when the fast electrons cross the solid-vacuum interface. The two-temperature distribution is related to different electron acceleration mechanism in a plasma density gradient. The high energy tail, which extends up to several tens of MeV, may be related to wake-field type acceleration in the underdense plasma while the low energy part correspond to the energy scaling for $\mathbf{J} \times \mathbf{B}$ and resonant absorption heating.

2.5.3 Fast electron temperature

Let's now focus our attention on the parameter T_{hot}, that determines the slope of the energy distribution function. A general scaling law seems to hold for different acceleration mechanisms, given by $T_{hot} \propto (I\lambda^2)^b$, where b assumes different values according to the laser intensity, $b \approx 1/3$ for lower laser intensities (below $10^{19}\mathrm{W/cm}^2$), and $b \approx 1/2$ for ultra-relativistic intensities. Note that the value of T_{hot} has in general to be considered as fast electron "slope-temperature" or average energy, given the exponential distribution functions obtained by measurements as well as simulations. For relatively low laser intensities ($b \approx 1/3$), the predominant heating processes are resonant absorption and vacuum heating, and the fast electron temperature scaling law [**?**] is expected to be, in practical units:

$$T_{hot} \approx 100\mathrm{keV}(I_{17}\lambda_{\mu m}^2)^{1/3}, \tag{2.62}$$

where I is measured in units of $10^{17}\mathrm{W/cm}^2$ and λ in μm. For ultra-relativistic laser intensities, the oscillatory component of the ponderomotive force becomes important, and the scaling law is represented by the $\mathbf{J} \times \mathbf{B}$ heating given in equation **??**, and that we repeat for simplicity:

$$T_{hot} = 511\mathrm{keV}\left[\left(1 + 0.43 I_{18}\lambda_{\mu m}^2\right) - 1\right]. \tag{2.63}$$

It is possible to observe the transition between the two scaling laws, related to the different acceleration mechanisms, using proton diagnostics. As we will see in section **??**, the maximum accelerated proton energy E_{max} is directly related to the laser intensity. From the analysis of several experiments [**?**, **?**, Clark+al] a change of slope for E_{max} occurs at $I\lambda^2 \sim 10^{19}\mathrm{W/cm}^2$, as represented in figure **??**.

2.5.4 Collective stopping power

A fast electron beam propagating in matter can be described by a current $I(\mathrm{A})$, with a current density $J(\mathrm{A/cm}^2)$. A rough estimate of the fast electron

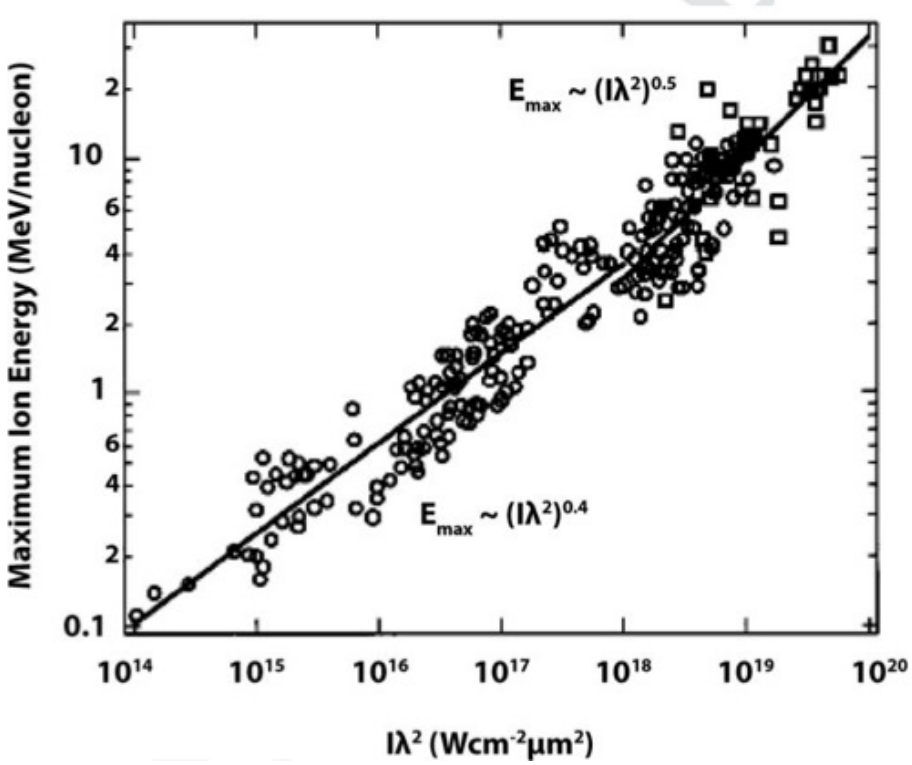

Figure 2.6: **Maximum proton energy versus $(I\lambda^2)$. The slope change occurs for intensities about 10^{19}W/cm^2. At low intensities, E_{max} scales as 0.4 power of $(I\lambda^2)$, but it should be pointed out that the $1/3$ power law is related to the fast electron average energy and not to the maximum ion energy. Figure taken from Clark et al. [?].**

current magnitude is very straightforward. If we consider a $\tau \approx 700$ fs laser pulse with average intensity $\sim 5 \times 10^{19}$W/cm^2 and total energy of $E_{Las} \approx 150$J (typical parameters for the Jupiter Laser Facility, Titan target area short pulse, at Lawrence Livermore National Laboratory), and assuming a conversion efficiency of $\eta_{eff} \approx 30\% = 0.3 \times E_{Las}$, as given in figure **??**, the fast electron current can be estimated as:

$$I \approx \frac{E_{Las}\eta_{eff}}{T_{hot}\tau} \approx 25 \times 10^6 \text{A}, \tag{2.64}$$

that is an enormous value! Such a current cannot propagate due to the Alfven [?] limit to the current density:

$$J_A = \frac{4\pi mc\gamma\beta}{\mu_0 e}, \tag{2.65}$$

given in useful units by

$$J_A = 15000\gamma\beta. \tag{2.66}$$

The Alfven current J_A represents the largest current that can propagate in vacuum or in a conductive medium. Above this limit the current cannot propagate anymore due to the self-generated magnetic field action on the electron beam, which turns the electrons back to the source. Moreover, the magnetic field generated by such a current, assuming a beam radius of 50μm and the electron beam to be confined in a cylinder of $60\mu m$ in lenght, the magnetic field amplitude at the edge of the cylinder will be $\sim$ 1000MG and the correspondent field energy $\sim$ 1.5 kJ, which is energetically unconceivable. Experimental results, nevertheless, show that such a high current does in fact propagate, which forces to make the assumption that this current is balanced point by point by a a second, counter-propagating return current, composed by background plasma electrons, so that

$$J_{tot} = J_{fast} - J_{ret} \approx 0. \tag{2.67}$$

The number of cold electrons constituting the return current is much larger than that of the fast electron current. Due to the much lower velocity, the return current electrons undergo collisions with background ions much more efficiently than fast electrons, or in other words, they are sensitive to the resistivity of the medium η. As conseuqence, the return current heats up the plasma medium by Ohmic heating $\propto \eta(T)J_{ret}^2$, where $\eta(T)$ is the temperature dependent resistivity. The resistive effects on the return current prevents a complete current neutralization, with the consequent generation of an electric field E opposed to the motion of the fast electrons. The growth of this resistive electric field gives rise to a magnetic field $\partial_t B = -\nabla \times E$, which has a collimating effect on the fast electron beam. The presence of E, opposed to

the fast electron transport as result of collective effects, is responsible for the so-called collective stopping power. It is possible to give a simple, analytical explanation of this effect (see Bell et al. [**?**]), starting from the assumption of current neutralization **??**, and considering the continuity equation for fast electrons:

$$\frac{\partial n}{\partial t} = \nabla \cdot \left(\frac{J_{fast}}{e} \right) = -\nabla \cdot \left(\frac{\sigma}{e} E \right), \tag{2.68}$$

where we used $J_{ret} = \sigma E$, with σ being the electric conductivity of the plasma. For a Maxwellian fast electron distribution confined by the electric field $E = -\nabla\phi$, the fast electron number density is $n = const \times \exp(\phi/T_{hot})$, giving:

$$E = -\frac{T_{hot}}{n} \nabla n. \tag{2.69}$$

Substituting this result in equation **??** we obtain:

$$\frac{\partial n}{\partial t} = \nabla \cdot \left(\frac{\sigma T_{hot}}{en} \nabla n \right), \tag{2.70}$$

which is a diffusion equation with diffusion coefficient $D = \sigma T_{hot}/en$, inversely proportional to the fast electron density. To solve this equation analytically, some strong assumptions and simplifications have to be applied: the fast electron temperature is assumed constant during laser irradiation, σ is assumed constant in space and time and the system is a one dimensional function of z, the distance from the focal spot. These assumptions are unrealistic but allow to get an estimate of the collective effects on fast electron transport. Under these conditions we find a solution for n in the form

$$n = n_0 \left(\frac{t}{\tau_{las}} \right) \left(\frac{z_0}{z + z_0} \right)^2, \tag{2.71}$$

where

$$n_0 = \frac{2 I_{abs}^2 \tau_{las}}{9 e T_{hot}^3 \sigma} \tag{2.72}$$

and

$$z_0 = \frac{3 T_0^2 \sigma}{I_{abs}}. \tag{2.73}$$

Where I_{abs} is the absorbed laser intensity, τ the pulse duration, and z_0 is the Ohmic stopping scale-length, which represents the distance over which the potential energy equals the energy of the fast electrons. The scale-length z_0 is directly proportional to the fast electron temperature and inversely proportional to the laser intensity and the resistivity. As the intensity goes up, the fraction of energy absorbed increases, and so the current density. This produces a higher potential that acts against the fast electron propagation. In the limit for very high intensities, z_0 becomes constant, due to the dependence $\propto T_{hot}^2$, being $T_{hot} \propto I_{abs}^{1/2}$.

2.5.5 Collisional and radiative stopping power

A fast electron beam propagating in a dense plasma undergoes binary collisions with plasma electrons and ions, loosing energy by inelastic scattering with electrons, by radiation (bremmsstrahlung) losses interacting with ions and exciting plasma waves, resulting in a total stopping power:

$$\left(\frac{dE}{ds}\right)_{total} = \left(\frac{dE}{ds}\right)_{collisional} + \left(\frac{dE}{ds}\right)_{radiative} + \left(\frac{dE}{ds}\right)_{waves}, \qquad (2.74)$$

where the first term on the right hand side accounts for inelastic collisions with electrons and the second term for bremmsstrahlung losses. The collisional term is, as well, composed by two contributions, accounting for free-bound and free-free electronic collisions:

$$\left(\frac{dE}{ds}\right)_{collisional} = \left(\frac{dE}{ds}\right)_{bound} + \left(\frac{dE}{ds}\right)_{free}. \qquad (2.75)$$

In general, the electron stopping power in matter, can be described for binary collisions as :

$$\left(\frac{dE}{ds}\right) = -En_i \int_0^{1/2} \epsilon \frac{d\sigma}{d\epsilon} d\epsilon, \qquad (2.76)$$

where $\epsilon = \Delta E/E$ represents the energy loss normalized by the energy of the incident electron, n_i is the ionic density and $d\sigma/d\epsilon$ is the differential cross section for energy transfer. The upper bound of the integral is set to 1/2

in order to account for indistinguishability of scattered electrons. Several works treated in great detail the stopping power for electrons in cold and warm matter [?] [?], due to collisions with bound and free electrons. Collisions with ions are quasi-elastic, due to the large ion mass compared to the electron mass $M \gg m$, keeping the electron energy substantially unchanged. The interaction of the electron with the ion potential modifies its trajectory, according, in first approximation, to Rutherford's theory of scattering, characterized by the cross section:

$$\sigma(\theta)_{Ruth} = r_e^2 \frac{Z^2}{\beta^4} \frac{1}{4\sin^4(\theta/2)}, \tag{2.77}$$

where $r_e = e^2/4\pi\epsilon_0 mc^2$ is the classic electron radius. The cross section $\sigma(\theta)$ reported above is divergent for small deflection angles. Introducing a Wentzel-Yukawa type screened potential of the form $V(r) \sim Zer^{-1}\exp(-r/\delta)$ [?], where $\delta = 0.885aZ^{-1/3}$ is the screening parameter, and $a = 4\pi\epsilon_0\hbar^2/me^2$ the Bohr radius, and correcting for relativistic electron energies, we finally obtain:

$$\sigma(\theta) = r_e^2 \frac{Z^2}{\beta^4\gamma^2} \frac{1}{4\left(\sin^2(\theta/2) + (1/\gamma ka)\right)^2}, \tag{2.78}$$

with $k = p/\hbar$ being the wave vector. The deflection of the electrons as consequence of Coulomb-type collisions is called *angular diffusion*. this effect reduces the fast electron penetration and increases the beam divergence [?]. Another important aspect of electron-ion collision, is the emission of x-rays, generated during the electron acceleration by the ion potential. This radiation, called *braking radiation* or *bremmstrahlung*, is at the origin of the so-called radiative stopping power. Similarly to equation [?], the radiative stopping power is expressed as :

$$\left(\frac{dE}{ds}\right)_{rad} = -n_i \int_0^E W \frac{d\sigma}{dW} dW, \tag{2.79}$$

where $0 \leq W \leq E$ is the emitted photon energy, and E is the energy of the colliding electron. Despite the presence in literature of several works treating the differential cross-section $d\sigma/dW$, the only analytical solutions

are obtained at expense of very strong approximations, and the results are out of the range of photon energies relevant for fast electron transport science. We report therefore, in figure **??**, cross sections tabulated in Atomic Data and Nuclear Data Tables [**?**], including nuclear and electron-electron bremmstrahlung.

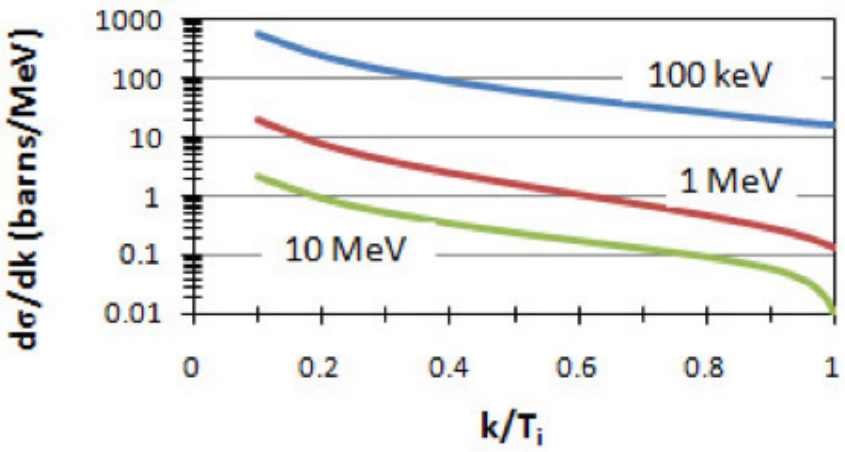

Figure 2.7: **Differential cross section for bremmstrahlung photon emission for photon energies of** 100 **keV,** 1 **MeV and** 10 **MeV. The cross section includes both electron-ion and electron-electron bremmstrahlung.**

2.5.6 Plasma resistivity

The plasma resistivity is a fundamental quantity to understand, and properly model, the fast electron transport in cold or Warm Dense Matter (WDM). However, the estimation of this physical quantity is, in many cases, quite difficult. Let's introduce the concept of resistivity following the classic Drude model [**?**]:

$$\eta = \frac{m\nu}{e^2 n_e}, \tag{2.80}$$

where ν is the electron-ion collision frequency and n_e the plasma electron density. The evaluation of this quantity is non-trivial over a wide range of

temperatures, from the melting point up to several tens of eV, depending on the material. Also, a lack of experimental data in this temperature range makes difficult to verify the validity of the models, attempting to provide a general description of resistivity. In general, the estimate of plasma resisitvity relies on the knowledge of the two fundamental parameters, ν and n_e, over a wide range of temperatures and densities. In the limit of a cold solid at temperatures below the Fermi temperature the electrons are in a degenerate state. The collision frequency in this condition is independent on the electron temperature and is determined by the electron-phonon scattering [**?**] ,

$$\nu_{el-phonon} = k_s \frac{e^2}{\hbar v_F}\left(2 - \frac{v_F^2}{c^2}\right)\left[1 + \left(0.13\frac{\hbar\omega_{pi}}{k_B T_i}\right)^2\right]^{-1/2}\frac{k_B T_i}{\hbar}, \tag{2.81}$$

where ω_{pi} is the ion plasma frequency and $v_F = \hbar(3\pi^2 n_e)^{1/3}/m$ is the Fermi velocity. k_s is a numerical constant which value is given in [**?**]. For cold, solid matter $v_F \ll c$ and $\hbar\omega_{pi} \ll k_B T_i$ and the $\nu_{el-phonon}$ can be approximated as:

$$\nu_{el-phonon} \approx 2k_s \frac{e^2 k_B T_i}{\hbar^2 v_F}. \tag{2.82}$$

For temperatures $T \gg T_F$, with T_F the Fermi temperature, the plasma behaves like a classic gas, and assuming a Maxwellian electron temperature, the plasma frequency is given by Spitzer [**?**]:

$$\nu_{Spitz} = \frac{4}{3}(2\pi)^{1/2}\frac{\bar{Z}e^4 m n_e}{(m k_B T_e)^{3/2}} ln(\Lambda), \tag{2.83}$$

where $\bar{Z}$ is the ionization degree, T_e the electron temperature and $ln(\Lambda)$ is the Coulomb logarithm, where $\Lambda = \left[1 + (b_{max}/b_0)^2\right]^{1/2}$, being b_{max} the maximum impact parameter usually associated with the Debye length $\lambda_D = (\epsilon_0 k_B T_e/n_e e^2)^{1/2}$ and $b_0 = max\left[\bar{Z}e^2/k_b T_e, \hbar/(m k_B T_e)^{1/2}\right]$. In general, there is no analytical expression for ν in the range of temperatures between the melting point and the Spitzer regime. Lee-More-Desjarles [**?**] developed a model based on the linearization of the Boltzmann equation, in stationary state (Maxwellian distribution) and in the limit of small temperature gra-

dients and weak electric field. A traditional solution to this problem is to perform an harmonic average of the electron-phonon and Spitzer collision frequencies of the form:

$$\nu^{-1} = \nu_{Spitz}^{-1} + \nu_{el-phonon}^{-1}, \tag{2.84}$$

and introduce a frequency cut-off

$$\nu < \frac{v_e}{r_0} = \frac{(v_F^2 + k_B T_e/m)^{1/2}}{r_0}, \tag{2.85}$$

to account for the unphysical high frequencies around the maximum of ν at few eV temperature. The electron mean free path λ_e, associated to the collision frequency, is in this temperature region, much smaller than the interatomic distance $\lambda_e \ll r_0$. The cutoff frequency in equation **??** imposes that the frequency cannot be higher than the electron thermal velocity $v_e = (v_F^2 + k_B T_e/m)^{1/2}$ divided by the interatomic distance.

The electron density n_e is a quantity dependent on the plasma electron temperature T_e and the plasma ion density n_i

$$n_e = \bar{Z}(T_e) n_i. \tag{2.86}$$

The calculation of $\bar{Z}(T_e)$ is non-trivial and is performed numerically, using ionization models such as the Thomas-Fermi [**?**], or in local-thermal equilibrium (LTE) conditions, the Saha-Boltzmann [**?**]. Hybrid simulations of high (solid and above solid) density plasmas make use of the equation of state (EOS) tables, to obtain for given values of density and temperature, the plasma average ionization state. A typical resistivity curve for solid density Al, resulting from the Eidmann-Chimier model, very close to the model described above, but including the cutoff frequency in the harmonic average, is given in figure **??**. $\bar{Z}$ is calculated using the Thomas-Fermi model.

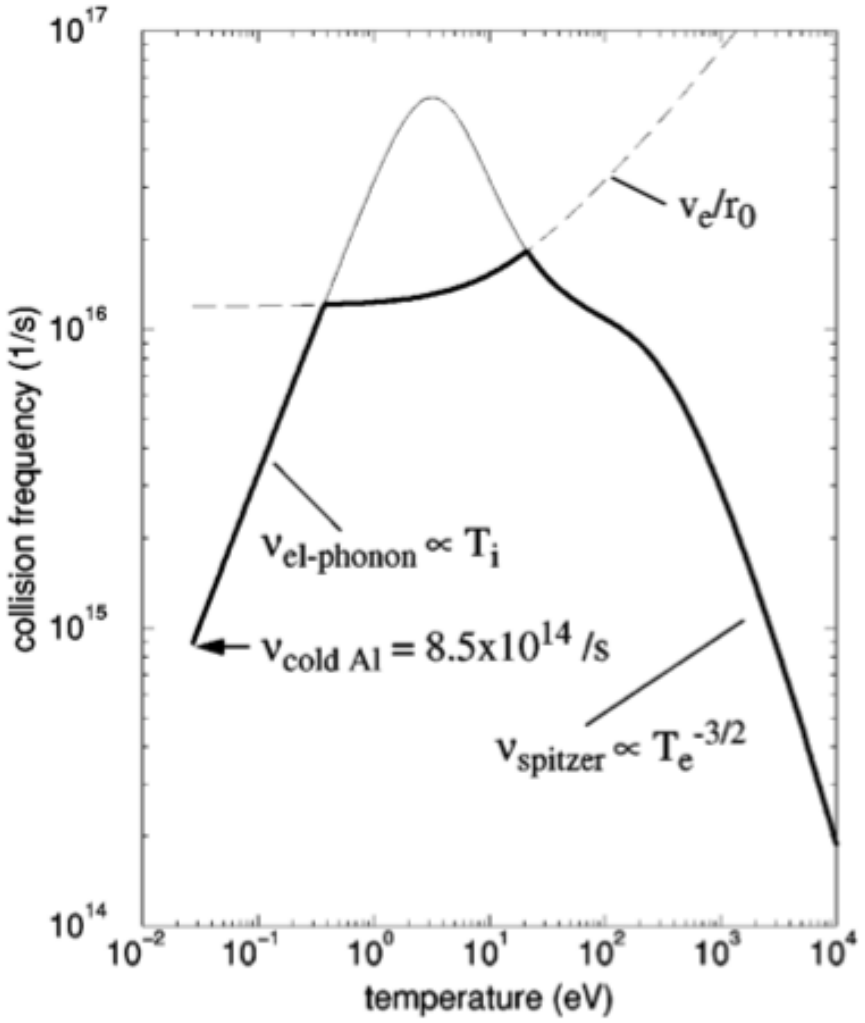

Figure 2.8: **Collision frequency for Al at thermal equilibrium ($T_e = T_i$), (thick solid line). The thin solid line is the interpolated frequency and the dashed line is the cut-off frequency. Image taken from [?].**

2.5.7 Ion acceleration

In several works as has been observed that high intensity laser interactions with solid targets lead to the production of multi-MeV proton and heavier ion beams [?] [?] [?] [?]. The source of these ion beams has been identified with a thin ($\sim$ nm) contaminant layer of hydrocarbons, condensed on the

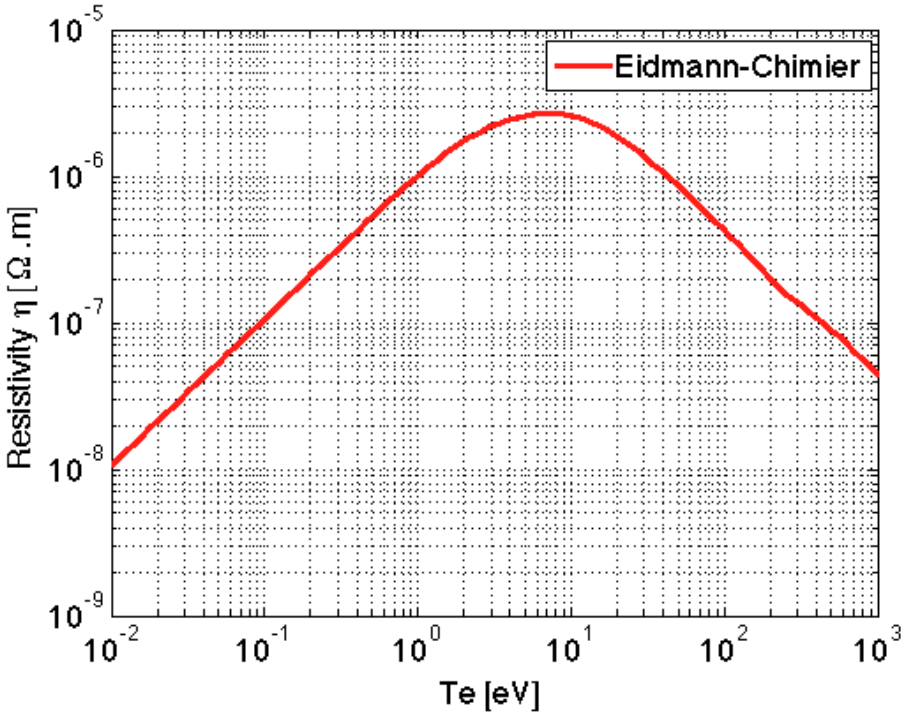

Figure 2.9: **Resistivity for solid density ($2.7 g/cm^3$) Al from the Eidmann-Chimier model.**

target surface. Protons are accelerated more efficiently than heavier ions due to the large charge to mass ratio. When a large number of laser generated fast electrons reach the target surface and expand into vacuum, the charge separation between the electrons and the plasma ions generates a large space charge electric field, directed normally to the target surface. This electric field forces the vast majority of fast electrons back into the target producing a well known effect called *fast electron refluxing*, and at the same time, accelerates the ions from the ionized contaminant layer into vacuum. This process is known as *target normal sheath acceleration* (TNSA). In general, this process occurs at the target front and rear surface, TNSA protons from the front surface generally have lower maximum energy than those accelerated from the rear because of the longer plasma scale length related to the laser pedestal. Several experiments evidenced that the ion acceleration is normal

to the target surface. In [?], Snavely et al. using a wedge shaped target, show ion emission normal to both wedge surfaces. TNSA proton beams have very remarkable properties such as point like source, high brightness and very low emittance. Several works attempted to give an analytical description of the proton acceleration process. In early works [?], analytical estimate for the initial electric field was found via self similar solution of fluid equations describing the 1D plasma expansion in a semi-infinite space. Assuming the hot electrons in equilibrium with the electrostatic potential $n_e = n_0 \exp(e\phi/T_e)$, a solution for the electric field is found as:

$$E_{sheath} = \frac{k_B T_{hot}}{e L_n}, \tag{2.87}$$

where $L_n = c_S \tau$ is the local plasma length. A more sophisticated model, accounting for the evolution of the electric field during the plasma expansion into vacuum is developed by Mora [?]. In this model, ions are assumed cold, with an initial step-like density distribution in $x = 0$. The electrons density is instead described by a Boltzmann distribution with temperature T_e:

$$n_e(x) = n_{e0} \exp\left(\frac{e\phi(x)}{k_B T_e}\right). \tag{2.88}$$

The Poisson equation is written in terms of the charge distribution $\rho(x) = e(n_e - Z n_i)$ as:

$$\frac{\partial^2 \phi(x)}{\partial x^2} = -\frac{\rho(x)}{\epsilon_0} = \frac{(n_e - Z n_i)}{\epsilon_0}. \tag{2.89}$$

For $x \leq 0$ the ion density is $n_i = n_{i0}$ and is $Z n_{i0} = n_{e0}$, and the Poisson equation becomes

$$\frac{\partial^2 \phi(x)}{\partial x^2} = \frac{e n_{e0}}{\epsilon_0} \left[\exp\left(\frac{e\phi(x)}{k_B T_e}\right) - 1\right], \tag{2.90}$$

and for $x > 0$ the Poisson equation becomes:

$$\frac{\partial^2 \phi(x)}{\partial x^2} = \frac{e n_{e0}}{\epsilon_0} \exp\left(\frac{e\phi(x)}{k_B T_e}\right), \tag{2.91}$$

being $n_i = 0$ for $x > 0$. Using $E = -\nabla\phi$, we can calculate the initial ($t = 0$) electric field at the front as:

$$E_{f0} = \int_0^\infty \frac{en_{e0}}{\epsilon_0} \exp\left(\frac{e\phi(x)}{k_B T_e}\right) dx = \sqrt{\frac{2}{e_E}} E_0, \tag{2.92}$$

where e_E is the Neper number 2.7182... and $E_0 = \sqrt{k_B T_e n_{e0}/\epsilon_0}$. For $t > 0$ the ions start expanding into vacuum, accelerating until the electrons lose the most of their energy. This is associated, according to Mora, to the laser pulse duration, or in other words, there will be hot electrons as long as the the laser generates them. The plasma expanding into vacuum is described in 1D by the fluid equations:

$$\left(\frac{\partial}{\partial t} + v_i \frac{\partial}{\partial x}\right) n_i = -n_i \frac{\partial v_i}{\partial x} \tag{2.93}$$

$$\left(\frac{\partial}{\partial t} + v_i \frac{\partial}{\partial x}\right) v_i = -\left(\frac{Ze}{m_i}\right) \frac{\partial \phi}{\partial x}, \tag{2.94}$$

where $v_i = v_i(x,t)$ and $n_i = n_i(x,t)$ are the local velocity and density of the ions. Assuming $T_i \ll T_e$, the plasma sound velocity is given by $c_s = (Zk_b T_e/m_i)^{1/2}$. Imposing the condition of quasi-neutrality

$$n_e = Zn_i = n_{e0} \exp\left(-\frac{x}{c_s t} - 1\right) \tag{2.95}$$

and $v_i = c_s + x/t$, we can find a self-similar solution to equations **??** and **??** in the form:

$$E_{ss} = \frac{k_B T_e}{e c_s t} = \frac{E_0}{\omega_{pi} t}, \tag{2.96}$$

where ω_{pi} is the ion plasma frequency. However, the solution **??** is meaningless for values of the Debye length $\lambda_D = (\epsilon_0 k_B T_e/n_e e^2)^{1/2}$ larger than $c_s t$. The solution also predicts the proton energy to diverge for $x \to \infty$. Solving the equations **??**, **??**, **??**, **??** using a 1D Lagrangian code, Mora obtains more accurate results for the peak value of the electric field as function of time :

$$E_t = \frac{2E_0}{(2e_E + \omega_{pi}^2 t^2)^{1/2}} = \sqrt{\frac{2}{e_E}} \cdot \frac{E_0}{\sqrt{1+\tau^2}}, \tag{2.97}$$

where $\tau = \omega_{pi} t/(2e_E)^{1/2}$. Solutions for the ion front velocity v_f and position x_f are found integrating the equations $dv_f/dt = ZeE/m_i$ and $dx_f/dt = v_f$ obtaining:

$$v_f \simeq 2c_S \ln\left(\tau + \sqrt{\tau^2+1}\right) \tag{2.98}$$

$$x_f = 2\sqrt{2e_E}\lambda_{D0}[\tau \ln\left(\tau + \sqrt{\tau^2+1}\right) - \sqrt{\tau^2+1} + 1]. \tag{2.99}$$

From this model is possible to estimate the maximum ion energy by assuming the acceleration time t to be equal to the pulse duration:

$$\mathcal{E}_{max} = \frac{1}{2} m_i v_f^2 \simeq 2Zk_B T_e [\ln(\tau + \sqrt{\tau^2+1})]^2. \tag{2.100}$$

Finally the self-similar model predicts the form of the ion energy spectra, $dN/d\mathcal{E}_i$:

$$\frac{dN}{d\mathcal{E}_i} = \frac{n_{i0} t}{\sqrt{2\mathcal{E}_i}} \exp\left(-\sqrt{\frac{2\mathcal{E}_i}{Zk_B T_e}}\right), \tag{2.101}$$

with $\mathcal{E}_i$ the ion energy. The ion spectrum has a sharp cutoff defined by $\mathcal{E}_{max}$.

Chapter 3

Experimental methods

In my thesis project, I had the fortune to perform a large number of experiments in about 10 different laser facilities around the world. The experiments were mainly focused on fast electron transport and fast ion beams production for FI research. The visited laser facilities include LULI 100 TW, LULI2000, Alisé laser Facility at Commissariat á l'Energie Atomique (CEA), Bordeaux, UHI100 at CEA Saclay, Vulcan Laser facility, Target Area Petawatt (TAP), at Rutherford Appleton Laboratory, Omega EP Laser Facility at Laboratory for Laser Energetics (LLE), Rochester, Jupiter Laser Facility (JLF), Titan target area , at Lawrence Livermore National Laboratory (LLNL), Tcubed Laser at Center for Ultrafast Optical Science (CUOS), University of Michigan, Chinese Academy of Sciences, Beijing, Tata Institute for Fundamental Research, Mumbai, India and GEKKO+LFEX laser at the Institute for Laser Engineering (ILE), Osaka, Japan. However, the experiences accumulated are too many to efficiently fit into a thesis dissertation, therefore I selected two of those experiments that allow me to give an overall feel of the breadth of the work I've been performing i past few years. The experiments relevant for this thesis work have been performed in two different laser facilities: Titan Target Area at JLF and Tcubed laser at CUOS. Both laser systems are Neodimium based and characterized by short, ultra-high intensity pulses, obtained via Chirped Pulse Amplification (CPA) technique [**?**]. In addition The Titan Target Area also features a long ($\sim$ 5ns) laser pulse to shock drive target

samples, or to be used as backlighter for x-ray radiography diagnostic.

3.1 Technology of ultra-intense laser pulses

The generation of short laser pulses has always been a fundamental area of laser research. Many are the motives that stimulated the research in short pulses: the seek for high power sources for fusion and particle acceleration research, the study of ultrafast phenomena that need to be resolved on a picosecond or femtosecond time scale, the study of high density plasmas for astrophysical research.

The introduction of mode-locking and Q-switching techniques, by means of acusto-optic modulators and saturable absorbers, represented a fundamental step forward in the quest for ultra-short pulses. The mode-locking technique resides on the multi-mode nature of laser light. The mode-locking [**?**] introduces a condition on the phases of the modes that can oscillate in a cavity, in general selecting only modes that periodically, constructively interfere, resulting in a very short, peaked single pulse, that oscillates in the cavity with period $\tau = 2L/c$, where L is the lenght of the cavity. The phase condition is imposed by a modulator, either electro-optic or, more common in traditional laser systems, acusto-optic. The modulator acts as a switch that opens with frequency τ the cavity, allowing the mode-locked pulse to oscillate, and closes at all other times to prevent any other light from oscillating in the cavity. The temporal lenght of the pulse is determined by the Fourier transform of the laser spectrum. Therefore only lasers with a relatively broad spectrum can be efficiently compressed. The Q-switching techinque [**?**] is adopted to obtain high energy, pulsed laser light. It is characterized by a switch device positioned inside the cavity that opens only when the amplifying medium reaches the maximum population inversion. At this point the light is allowed to oscillate in the cavity, rapidly discharging the medium and attaining high power. An example of Q-switching device is represented by a saturable absorber. When the population inversion in the amplifier medium reaches its maximum, the large amount of spontaneously emitted photons produces a saturation of the excited states in the saturable

absorber, with consequent transparency to laser light and cavity opening. Despite the introduction of Q-switching and mode-locking techiniques in the 70's, the peak laser intensity remained limited to few 10^{15}W/cm^2 for more than a decade, until the CPA technique was first proposed [**?**]. CPA laser pulses are characterized by high energy and ultra-short pulse duration (≤ 1 ps), with output power largely exceeding the TW value. The key of CPA technique is to temporally stretch the mode-locked laser pulse, allowing for higher amplification without exceeding the damage threshold for the amplifier, and subsequently re-compress it after the amplification stage, attaining high output power. The scheme of CPA is represented in figure **??**, the mode-locked pulse is extracted from the oscillator and spectrally dispersed by means of two gratings, stretching it in time by 3-4 orders of magnitude. The pulse is subsequently amplified in the laser chain, recompressed by means of two large gratings and sent in the experimental chamber where is focused by an off-axis parabola. No transmission optics are allowed after recompression in order to avoid velocity group dispersion with the consequent partial decompression of the beam, and because in many cases, the compressed beam power exceeds the damage treshold of the optics themselves.

As we observed, a large spectral bandwidth is required to efficiently compress the laser puse. In many laser systems, the bandwidth can be reduced at the high gain amplification stages such as the regenerative amplifier, where the pulse energy increases by several orders of magnitude. This phenomenon, known as "gain narrowing", causes the reduction of the spectral bandwidth, and therefore, the impossibility to re-compress the laser pulse to conditions close to the mode-locked pulse. The Optical Parametric Amplification (OPA) [**?**] technique has been introduced to avoid this problem and gurantee large bandwidth amplification. The chirped pulse is amplified in a non-linear crystal, typically Beta-Barium-Borate (BBO), which is pumped by a long (ns), temporally flat top, laser pulse with the energy of few Joules. The pulse length of the pump and the chirped seed pulse must be the same to guarantee maximum efficiency. The temporal top hat condition for the pump laser is crucial to obtain a uniform amplification of the seed, keeping its entire bandwidth. In the non-linear crystal, photons of the pump laser, polarized

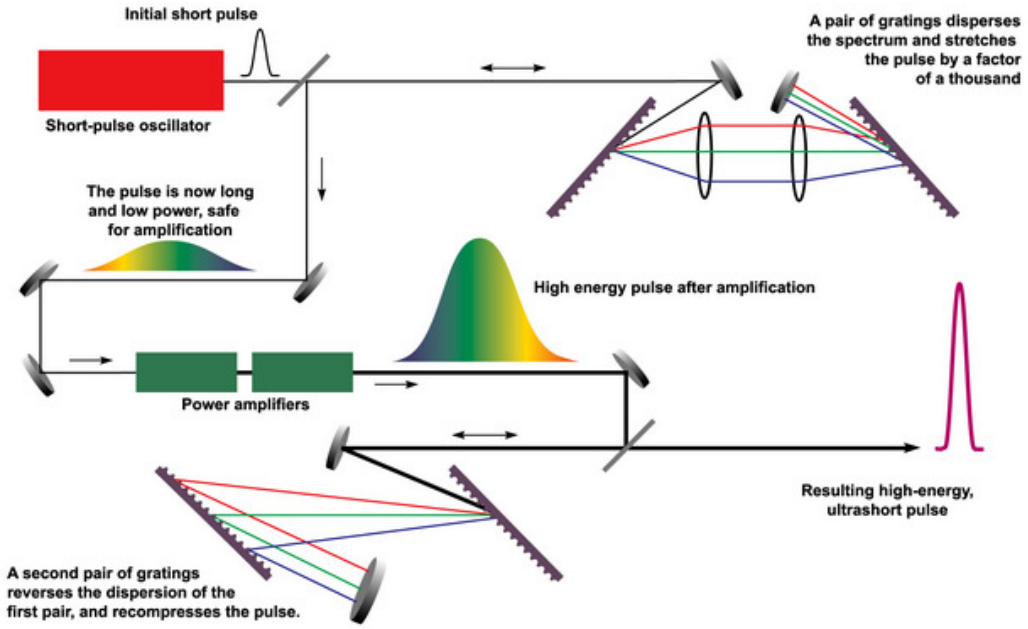

Figure 3.1: **The Chirped Pulse Amplification technique.**

orthogonally to seed, are converted into seed photons, plus an equal number of idler photons, so that $\omega_p \rightarrow \omega s + \omega i$. The phase matching condition applies to the wave-vectors as well, $k_p \rightarrow ks + ki$. The pump laser light is completely converterted into seed or idler photons, and allows to amplify the seed keeping its original spectral bandwidth. The OPA technique has recently substituted the regenerative amplifier stage in many laser systems.

3.1.1 Titan laser at JLF

The Titan laser is a petaWatt class laser based on Optical Parametric Chirped Pulse Amplification (OPCPA), achieving a peak intensity of 1×10^{20}W/cm^2 on target. The seed pulse, generated by a Time Bandwidth Products GLX-200 master oscillator, with duration of 100-200 fs, is stretched up to 1.6 ns and sent into a OPA preamplifier,consistent of two BBO crystals pumped by a 1.06 μm Nd:YLF laser with frequency doubled to 532 nm. The pulse is then amplified up to $\approx$ 5 J by 25 and 50 mm rod amplifiers, it takes a dual pass though 9.4 cm disk amplifiers. The pulse is then switched by a Pockels cell

and passes through a serie of 9.4 and 15 cm disk amplifiers, where it reaches its maximum energy of $\approx$ 300 J before compression. The pulse is then re-compressed under vacuum to about 0.7 ps by a pair of 40x80 cm Multilayer Dielectric (MLD) diffraction gratings and sent by two turning mirrors to the experimental chamber, where is focused down to $\approx 10\mu$m FWHM spot on target. Titan laser is composed also by a second, long pulse beam 300 J $\sim$ 5 ns, flat top temporal profile, used to drive shock in targets or as a back-lighter. The pulse is produced using the same OPCPA method as the Titan short pulse, and is frequency doubled using a KDP anisotropic crystal. The pulse is then focused by means of a 200 mm, $f/5$ lense on a 20μm focal spot. The lens is usually coupled with a random phase plate (RPP), obtaining a flat top smoothed spot with size varying from 200 to 700μm according to the type of RPP adopted. The timing of the two beams is determined by means of two photodiodes coupled with an oscilloscope. The uncertainty in the measurement is about 100 ps, to which has to be added the electronic jitter of about 100-200 ps. In the long pulse laser chain is included a delay line, that allows to set a delay between long pulse and short pulse of $\pm$10 ns.

3.1.2 Tcubed laser at CUOS

The Tcubed laser is a teraWatt class laser at CUOS, University of Michigan. The T-cubed oscillator system "Mira-900" by Coherent utilizes a Kerr mode-locked Ti:sapphire laser producing a 76 MHz train of 100 fs pulses operating at a wavelength of 1.053 microns with an average power of 200 mW. This oscillator is pumped with CW Coherent "Innova 200" argon laser, which produces multi-line output over the wavelength range 0.47-0.53 microns with an average power of 10 W. The argon laser has a maximum output power of 30 W. The short pulse train from the oscillator is sent to the stretcher, where it is stretched out temporally by 4 passes on a single 1740 lines/mm grating to $\approx$ 1 ns. After the selection of a single pulse with the Pockels cell at 10 Hz repetition rate it is amplified in the Ti:Sa regenerative amplifier to a 1 mJ level. The regenerative amplifier is pumped with frequency doubled 10 Hz repetition rate Continuum "Surelight" laser. The pump laser has

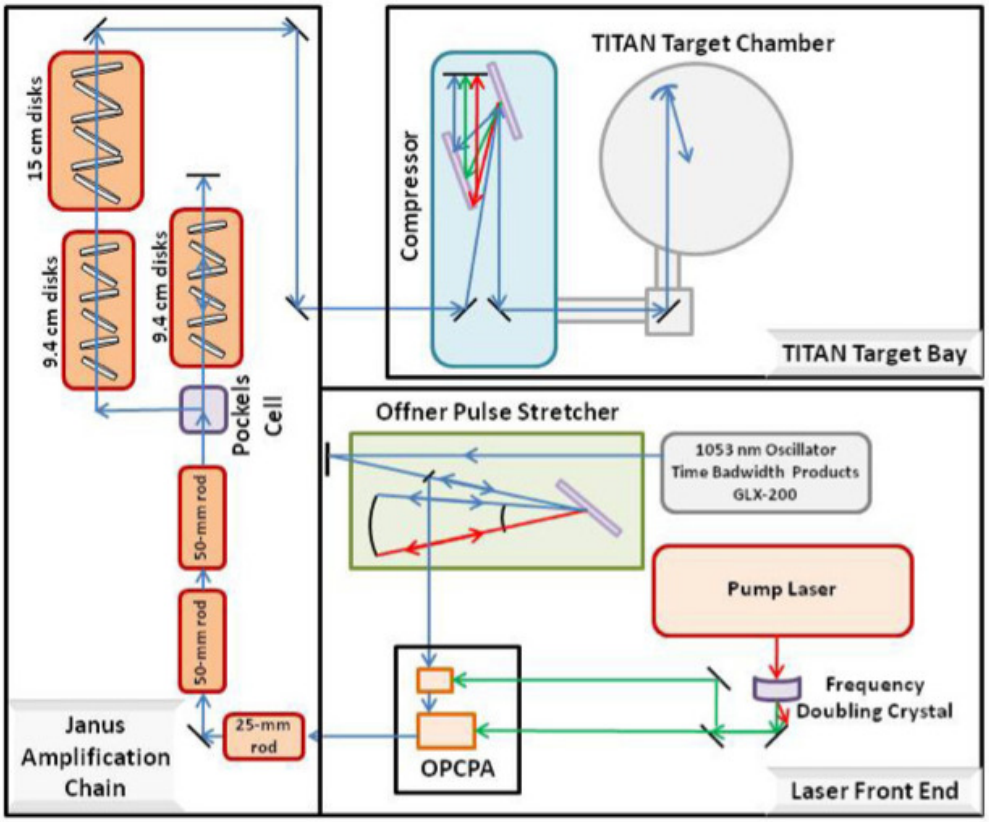

Figure 3.2: **Schematic of Titan laser at JLF, courtesy of Lawrence Livermore National Laboratory.**

wavelength of 0.53μ , duration of 6 ns and delivers $\sim$ 30 mJ/arm of pump energy to both ends of Ti:Sa crystal. The regen output is coupled into the amplification chain, where it is amplified in Neodymium doped glass rod (Nd:Glass) amplifiers up to 10 Joules. The chain currently consists of two heads with rods of 16×500 mm and one head with a rod of 45×500 mm. Vacuum spatial filters after each Nd:Glass amplifier vacuum are used for beam expansion, relay imaging and beam smoothing by elimination of local modulations of its intensity. The operational repetition rates of the final amplifiers are 3 minutes for the 16 mm heads and 8 minutes for the 45 mm head. The amplified pulse is delivered to the vacuum compressor chamber, where it is compressed by a grating pair (1740 l/mm) to duration of 0.4 ps

and has a maximum energy of 6 J.

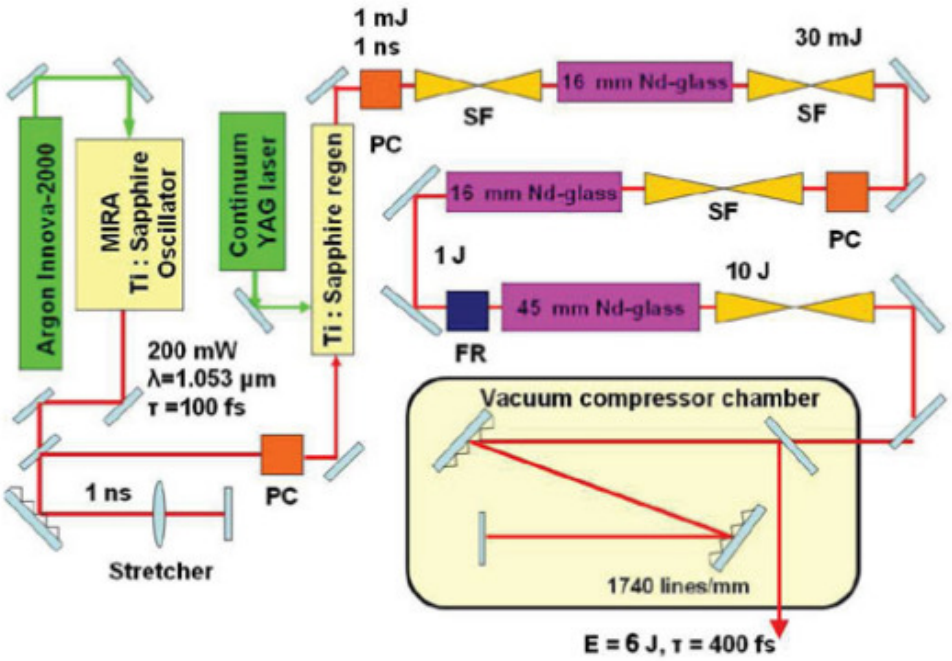

Figure 3.3: **Schematic of Tcubed laser at CUOS, courtesy of the University of Michigan.**

3.2 Laser diagnostics

The laser source needs to be carefully characterized before the experiment. A suite of laser diagnostics are available on Titan to measure laser focal spot size, pulse duration and intensity distribution in the focal spot. The focal spot size for both Titan beams is measured under vacuum using a 12-bit CCD camera coupled with a microscope objective. The image is taken from target chamber center (TCC) during the final stage of the focal spot optimization.

3.2.1 Equivalent Plane Monitor

The on shot intensity distribution at the target plane is measured using an equivalent plane monitor (EPM), that images the focal spot from a $f/26$ nova lens collecting the 10^{-4} leakage from the final turning mirror before the parabola. The image is recorded on a 16-bit CCD Apogee Alta U2000 camera. The camera has a 1600×1200 pixels and images the focal spot with a $66\times$ magnification. The focal spot image recorded by the EPM and relative intensity distribution is represented in figure **??**, **??**.

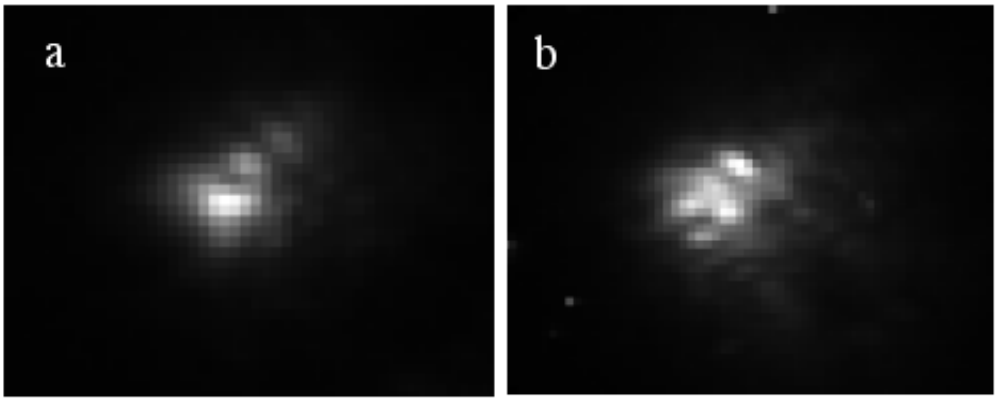

Figure 3.4: **EPM image of the focal spot for low energy OPCPA (a) and full-energy shot (b).**

3.2.2 Second order autocorrelator

The pulse duration is measured on shot by a second order autocorrelator. After compression, a small part of the beam is extracted and splitted in two beams using a beam splitter. One of the two beams travels through a delay line, and the two beam paths cross in a non-linear KAP crystal. The single beam intensity is not high enough to induce non-linear effects, with second harmonic generation, in the crystal. Only when the two beams overlap, the total light intensity becomes high enough. The two beams are synchronized in the crystal by changing the delay on the delay line. Perfect overlapping occurs when the intensity of the 2ω light is maximized. The pulse duration

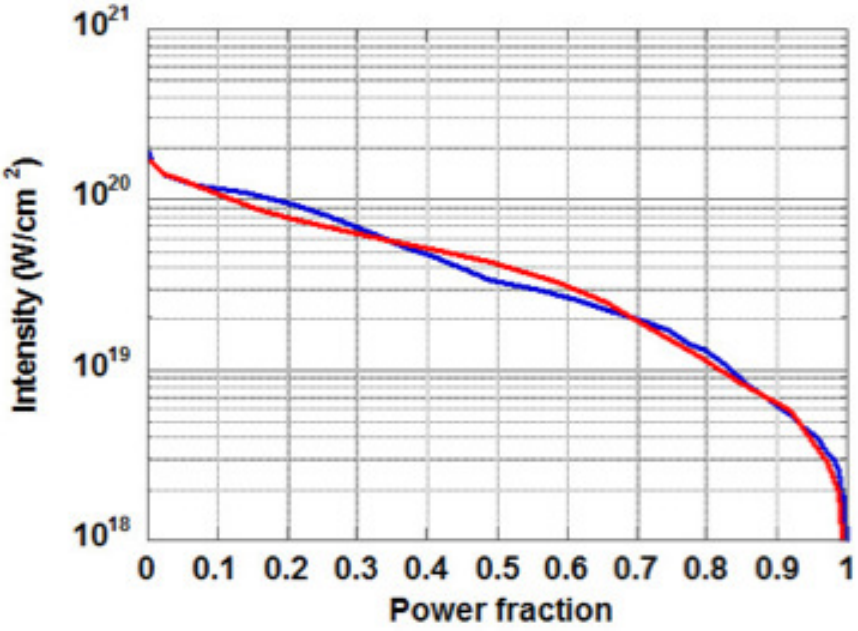

Figure 3.5: **Intensity distribution for (blue) full energy shot and (red) low energy OPCPA. The intensity distribution is calculated for a** 150 **J laser energy and** 0.7 **ps pulse duration.**

is then measured shot-to-shot by measuring the size (FWHM) of the 2ω emission, recorded by a 16-bit CCD camera with interferential filter.

3.2.3 Pre-pulse measurement

A laser pulse is always characterized by the presence of a pedestal with duration of few nanosecond, preceding the main short pulse.The pedestal is due to Amplified Spontaneous Emission (ASE) in the amplifiers. The ASE is often combined with a prepulse, produced by stray reflections i the beamline, preceding by few nanoseconds the main pulse. The action of ASE and prepulse leads to the generation of a plasma on the target front surface called preplasma, which scale-length determines the laser-plasma interaction, influencing the fast electron energy distribution. Therefore the knowledge of the prepulse and pedestal energy and duration is fundamental to properly model

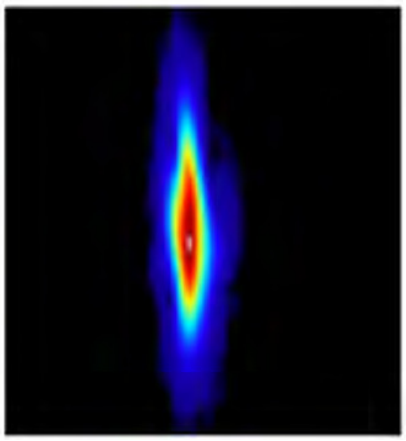

Figure 3.6: 2ω **emission from the overlapping of the two beams in the anisotropic crystal.**

the fast electron source. The measurement of this quantity is performed using a fast photodiode coupled with an oscilloscope. Typical energy values for ASE at Titan laser range from 5 to 80 mJ and 1-30 mJ for the prepulse spike.

3.3 X-ray diagnostics for fast electron transport

As we already observed in the previous chapter, the fast electron stopping power is distinguished into collisional and collective effects. In particular, collisional effects lead to emission of radiation, either from atomic level recombination, subsequent the impact ionization from fast electrons, or emitted directly from fast electrons as result of coulomb collisions with the ions of the plasma medium.

3.3.1 $K\alpha$ emission

The spectroscopy of $K\alpha$ radiation emitted from solid or above solid density targets is one of the most common diagnostics for fast electron transport. The

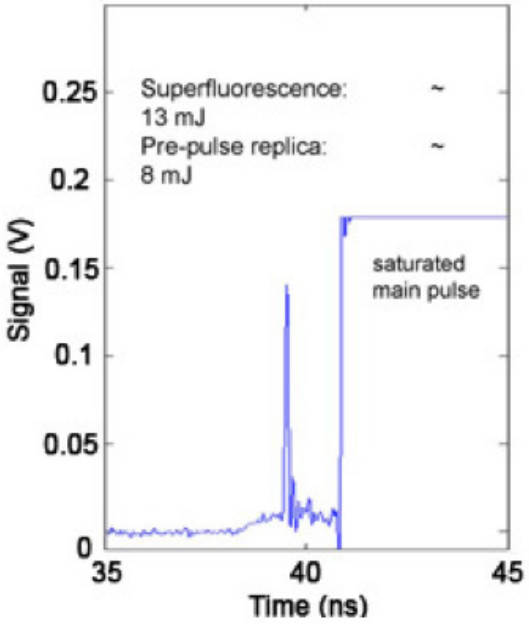

Figure 3.7: **Trace of prepulse and ASE on the oscilloscope at Titan laser. The main pulse saturates the signal on the oscilloscope.**

absence of constraints for diagnostic alignment, due to the intrinsic isotropic nature of $K\alpha$ emission, allows for a variety of possible experimental setups, for spectroscopy or imaging of the x-ray source. The spectroscopic diagnostic technique implies the usage of tracer layers or tracer dopant materials, characterized by a relatively high $K\alpha$ emission energy, related to the impact ionization by hot electrons, and allowing the radiation itself to be only partially re-absorbed in the target material. In principle, the adoption of very high Z materials as tracer layer, such as for example Au, would be ideal because allows the selection of higher energy electrons and is less sensitive to temperature shifting of the $K\alpha$ lines, undesired effect for imaging diagnostic. However this would, at the same time, introduce a severe limitation on the x-ray diagnostics that could be used, being the most of them based on the Bragg reflection, which is limited to about 20 keV, but becomes already very poorly efficient for x-ray energies exceeding 10 keV. In this section we briefly

introduce the theory of K-shell ionization and $K\alpha$ photon emission and its implications to the study of fast electron transport in dense plasmas.

The radiation emitted as result of atomic K-shell recombination has a well specified energy $E_{K\alpha}$, related to the binding energy of the scattered electron E_K as follows:

$$E_{K\alpha} = E_K - E_{L\alpha} - E_{M\alpha} - ... \tag{3.1}$$

Where $E_{L\alpha}$ and $E_{M\alpha}$ are the energies of the photons emitted as result of recombination cascade effect, from the K-shell up to the outer atomic level. The radiation emitted as consequence of an electronic transition from the L-shell to the K-shell of an atom is called $K\alpha$ radiation, while a transition from the M-shell to the L-shell is called $L\alpha$ radiation. In general this radiation is not single lined, but composed by multiple lines with different relative intensity related to the transition probability from different energy levels. For example, the $K\alpha$ emission from a Cu ion is composed by a doublet corresponding to the transitions $2p_{3/2} \rightarrow 1s$ and $2p_{1/2} \rightarrow 1s$, with relative intensity of 1 and 0.51 and emitted photon energies of 8.048 and 8.028 keV.

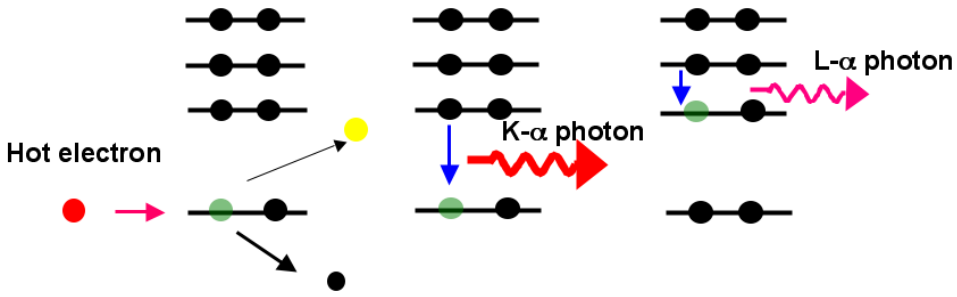

Figure 3.8: **Schematic of K-shell ionization and subsequent cascade emission.**

However, a fast electron beam propagating in matter statistically produces ionization of all atomic levels, according to their relative ionization cross section. A first example of ionization cross section in the non-relativistic limit is given by Lotz empirical formula [**?**]:

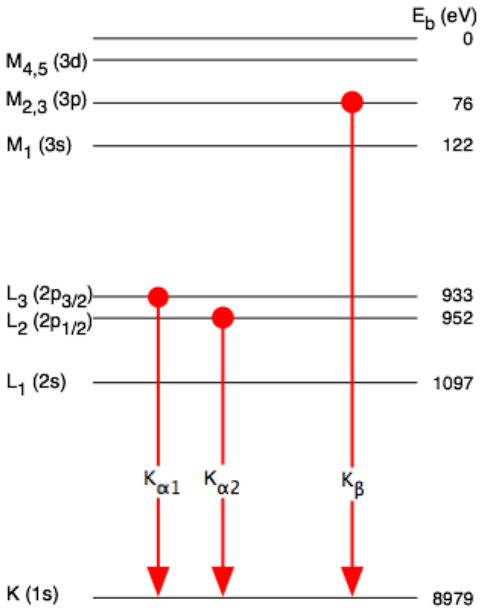

Figure 3.9: **Scheme of the atomic transitions related to Cu K-shell ionization.**

$$\sigma_i(E) = \sum_{i=1}^{N} a_i q_i \frac{\ln(E/P_i)}{EP_i}\{1 - b_i \exp\left[-c_i(E/P_i - 1)\right]\}, \tag{3.2}$$

where P_i is the electron binding energy in the i-th subshell (note that this formula is valid only for $E \geq P_i$), q_i is the number of equivalent electrons in the i-th subshell, a_i, b_i and c_i are individual constants tabulated for each subshell. From this formula it appears clear that the overall cross section is inversely proportional to the electron binding energy, this means that for inner shell electrons of high Z materials, the probability of electron impact ionization can be significantly smaller than for lighter materials. If we focus our attention on the K-shell ionization cross section and we account for relativistic corrections, σ_{K-Rel} is expressed by [**?**]:

$$\sigma_{K-Rel} = 2\pi a_0^2 R(U) \left(\frac{R_H}{E_K}\right)^{G(U)} D(U), \tag{3.3}$$

where a_B is the Bohr radius, $R_H = m_e e^4/(8\epsilon_0 h^2) \approx 13.6$ eV is the Rydberg constant, $G(U)$ and $D(U)$ are a-dimensional quantities dependent on the fast electron energy $U = E/E_K$, with E_K the K-shell ionization potential

$$G(U) = 2.0305 - \frac{0.316}{U} + \frac{0.1545}{U^2} \tag{3.4}$$

$$D(U) = \left(3.125 - \frac{4.172}{U} + \frac{1.877}{U^2}\right)\frac{\ln U}{U}. \tag{3.5}$$

Finally, introducing $J = m_e c^2/E_K$, we define the relativistic correction factor $R(U)$ as:

$$R(U) = \left(\frac{1+2J}{U+2J}\right)\left(\frac{U+J}{1+J}\right)^2\left[\frac{(1+U)(U+2J)(1+J)^2}{J^2(1+2J)+U(U+2J)(1+J^2)}\right]^{3/2} \tag{3.6}$$

The relativistic correction factor is responsible for the increase in the K-shell

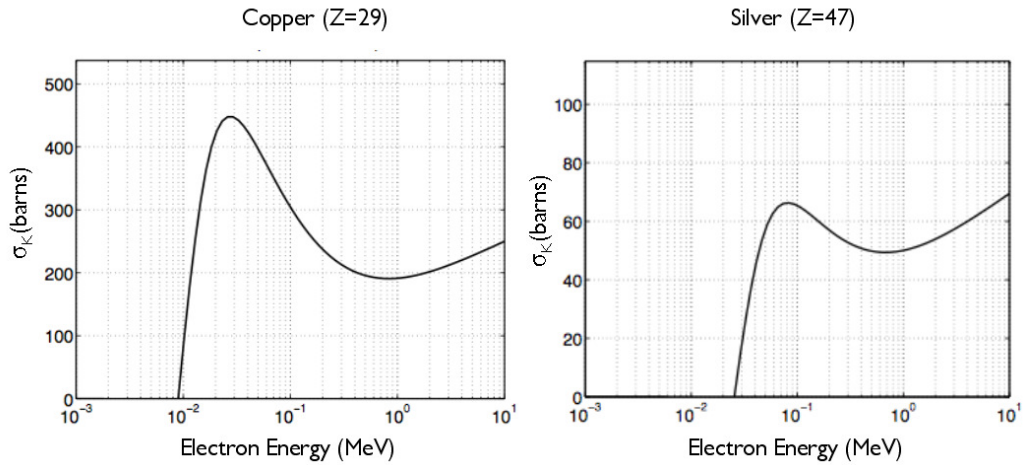

Figure 3.10: **K-shell ionization cross-section in Barns for Cu and Ag ions.**

ionization cross section at high incident electron energies ($E \geq 2$ MeV). Is also important to observe that for $E \approx 3E_K$ the cross section reaches a local maximum, which is about 400 barns for Cu. Therefore, in case of Cu, the $K\alpha$ emission becomes significant for electron energies above 20 keV.

3.3.2 $K\alpha$ fluorescence

In general, not all the K-shell vacancies result in the emission of a $K\alpha$ photon. Non-radiative transitions, in which an electron is emitted instead of a photon, may indeed occur. This effect is known as Auger effect, and the emitted electron is called Auger electron. The fluorescence of the $K\alpha$ emission ω_K depends on the atomic number Z as follows [**?**]:

$$\omega_K(Z) = \frac{\left[\sum_{i=0}^{3} C_i Z^i\right]^4}{1 + \left[\sum_{i=0}^{3} C_i Z^i\right]^4}, \tag{3.7}$$

with $C_0 = 0.037$, $C_1 = 0.031$, $C_2 = 5.44 \times 10^{-5}$, $C_3 = -1.25 \times 10^{-6}$. The evolution of the K-shell fluorescence as function of atomic number is represented in figure **??**.

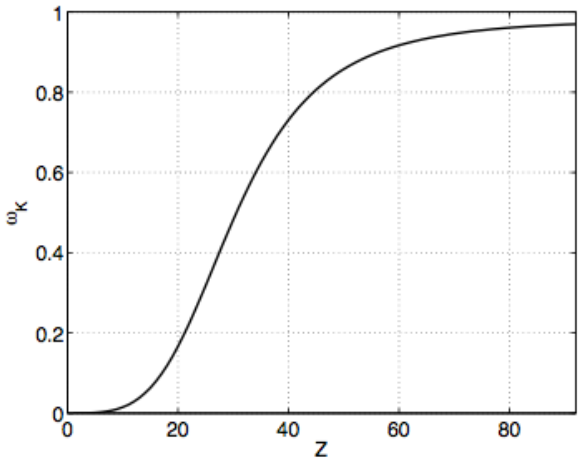

Figure 3.11: **K-shell fluorescence versus atomic number.**

3.3.3 Relation between fast electrons and $K\alpha$ emission

The total $K\alpha$ yield is strictly related to the number of fast electrons propagating through the tracer layer. As we already observed in section **??**, electrons with energy $E \geq 20$ keV produce significant K-shell ionization. Since the average energy of the fast electron beam exceeds by far this lower

boundary, $K\alpha$ diagnostics have to be considered as *particle counters*. The relation between fast electrons and emitted $K\alpha$ photons can be written as follows:

$$N_{K\alpha} = N_{fast} \int_{E_K}^{\infty} f(E_0) dE0 \int_{E_0}^{E_K} \omega_K n_i \sigma_K(E) \left(\frac{dE}{ds}\right)^{-1}, \qquad (3.8)$$

where $N_{K\alpha}$ is total number of $K\alpha$ photons emitted, N_{fast} the total number of fast electrons, $f(E_0)$ is the normalized initial fast electron distribution with E_0 the electron energy, ω_K as defined in the section above, n_i is the tracer layer ion density, $\sigma_K(E)$ is the K-shell ionization cross section and finally dE/ds is the fast electron stopping power in matter. The calculation of the total $K\alpha$ yield using a calibrated spectrometer can provide an estimate of the total number of hot electrons produced and therefore, of the laser-to-electrons energy conversion efficiency. At the same time, varying the position of the tracer layer in the target by varying the thickness of the overcoating layer allows to get information on fast electron transport in the overcoating material, by measuring the variation in the total $K\alpha$ yield. Of course, this cannot be more than an estimate, indeed the fast electron distribution must be inferred from electron or bremmsstrahlung spectroscopy as well as from LPI simulations. Moreover refluxing effects may cause an increase in the total $K\alpha$ yield, introducing additional uncertainty in the calculation.

3.3.4 Bremmsstrahlung radiation

Bremmsstrahlung radiation is characterized by continuum x-ray spectra, and is generated by the deflection of fast electrons from their original trajectory, undergoing Coulomb collisions with the plasma ions. The basic concepts have been exposed in section **??**. The Bremmsstrahlung radiation is directional, with an average angle form the initial electron trajectory $\langle\theta\rangle \propto 1/\gamma$, with γ the relativistic factor. For electron energies > 1 MeV, the characteristic angle is $\approx 1°$, while for lower energies assumes values close to $20°$. The energy distribution is characterized by an exponential decay and the intensity is proportional to Z^2, as the cross section for Coulomb collisions with ions. In

principle, from spectroscopic measurement of the bremmsstrahlung emission is possible to estimate the fast electron energy and angular distribution, by means of Monte Carlo collisional modeling of fast electron transport.

3.3.5 Bragg reflection

The vast majority of x-ray spectrometers is based on the Bragg reflection principle. The phenomenon was first discovered by William Henry and William Lorentz Bragg at the beginning of the 20th century. The term *reflection* is , in this context, actually quite ambiguous, suggesting for a mirror-like process. Bragg reflection is instead based on the scattering of x-ray radiation by the ions of a crystalline lattice. The scattered x-rays by the regular atomic pattern of the crystal interfere destructively with each other, except for those propagating in a specific direction, which interfere constructively and constitute indeed the "reflected" x-ray radiation. The scattering angle θ allowing for constructive interference is determined by the wavelength λ of the incident x-rays and the crystal interatomic spacing d as follows:

$$2d \sin\theta = n\lambda, \tag{3.9}$$

where $n \geq 1$ is a positive integer that indicated the order of reflection. X-rays of different wavelengths are reflected at different angles, allowing for x-ray line spectroscopy. Moreover, a variety of crystals with different interatomic spacings are available, allowing for spectroscopic study of basically all x-ray emission in the range 0.5 to 10 keV. In figure **??** is represented the Bragg reflection mechanism. Moreover, thin artificial crystals can be easily bent in a variety of shapes, spherical, cylindrical, conical, assuming focusing in addition to the spectroscopic properties.

3.3.6 Kα imager

The $K\alpha$ imager is a widely used diagnostic for fast electron transport. It is constituted by a spherically bent Bragg crystal, which interatomic spacing allows to reflect specific $K\alpha$ radiation (usually Cu and Ti $K\alpha$) at $\theta_B \approx$

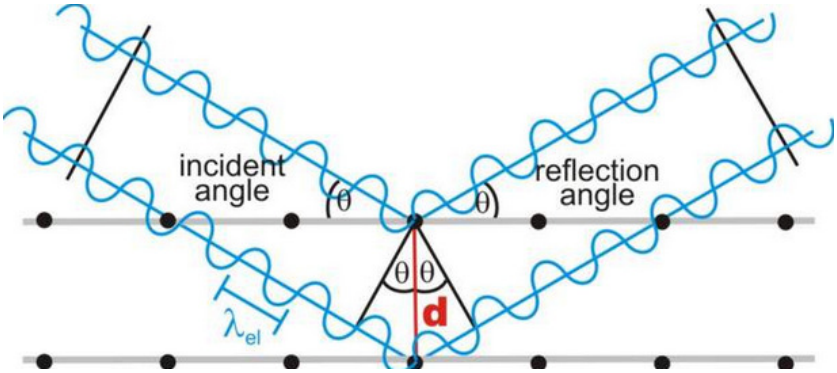

Figure 3.12: **Schematic of the Bragg reflection condition.**

90°, very close to normal incidence. The focusing property of the crystal, determined by its bending, coupled with the quasi-normal x-ray reflection, makes it an imaging device, mathematically described as a spherical mirror:

$$\frac{1}{p} + \frac{1}{q} = \frac{2}{R}, \tag{3.10}$$

where p indicates the image, q the object, and R is the curvature radius of the crystal. In general this equation as the straightforward solution:

$$p = \frac{qR}{2q - R}. \tag{3.11}$$

The $K\alpha$ imager is an intrinsically astigmatic optical system, being the source, and consequently the image, off axis. The x-ray detector has therefore to be positioned between the meridional and the sagittal focal position, close to the so-called *circle of least confusion*, in order to maximize the spatial resolution of the image. The sagittal and meridional focal position is determined by the crystal curvature radius as well as the Bragg angle as follows:

$$p_s = \frac{qR}{2q \sin\theta_B - R} \tag{3.12}$$

$$p_m = \frac{qR \sin\theta_B}{2q - R \sin\theta_B}. \tag{3.13}$$

For example, for a typical alignment on Titan laser, using a spherically bent Quartz $21\bar{3}1$ crystal, with spacing $2d = 3.082\mathring{A}$, curvature radius $R = 500$ mm and Bragg angle for Cu-$K\alpha_1$ (8.0478 eV) $\theta_B = 88.7°$, the values of p and q are respectively 1738 and 292 mm. From equations **?? ??**, the values for p_s and p_m are respectively 1741.2 and 1735 mm. This means that for a distance object-crystal $q = 292$ mm, the maximum tolerance for the positioning of the detector is of $p_s - p_m = 6.2$ mm or ± 3.1 mm around the median position given approximately by $p = 1738$ mm. On the object side, this results in a tolerance of about 200μm or $\pm 100\mu$m for fixed image position at p. This implies that for targets involving tracer layers buried at depth $\geq 100\mu$m from the target front surface, aligned at TCC, the crystal imager should be aligned at an intermediate position between the front surface and the deepest buried tracer layer, in order to do not lose spatial resolution. The astigmatism

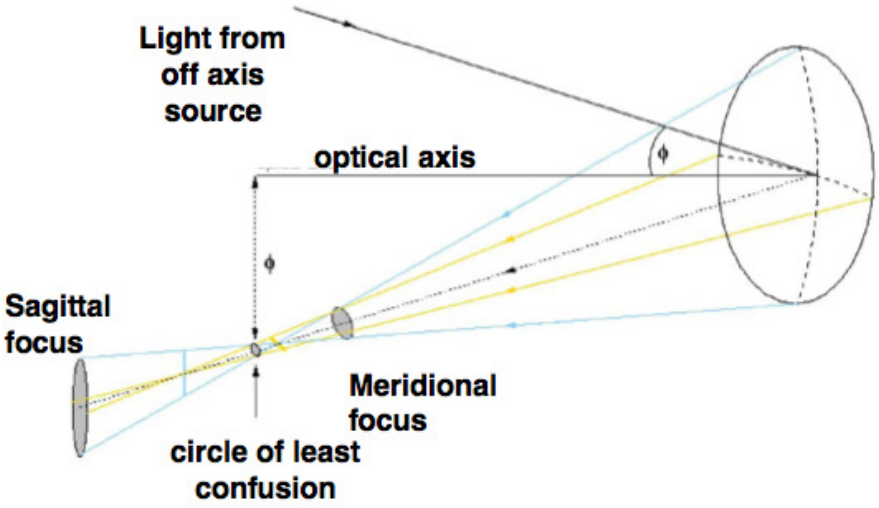

Figure 3.13: **Sagittal, meridional and best focal position (circle of least confusion) for a spherical mirror with off-axis source.**

limited spatial resolution for ideal alignment is given by :

$$\sigma = \frac{M+1}{M}(1 - \sin\theta_B)D, \tag{3.14}$$

where M is the magnification of the system ($M = p/q$) and D is the aperture on limiting the collecting area of the crystal. Another important limitation to the resolution is the bending quality of the crystal, in many cases, the bending process introduces several cracks in the crystal, resulting in mosaic structure, and affecting the overall resolution of the optical system. The crystal is obviously not a perfect monochromator, and the reflected bandwidth depends strongly on the aperture in front of the crystal. For aperture diameter $D = 15$ mm, the spectrum collected by the crystal is about 6 eV, and ranges from 8.046 to 8052 eV. In case of temperature blu-shift of the $K\alpha$ emission, the efficiency of the crystal can sensibly reduce, due to the distribution of the x-ray radiation over a wider energy spectrum.

3.3.7 X-ray spectroscopy

X-ray spectroscopy is a fundamental diagnostic for laser-produced plasmas studies and a variety of spectrometers and spectroscopy techniques are available. We will concentrate our attention in those directly related to the experimental work exposed in this manuscript.

Flat spectrometer

The simplest spectrometer design makes use of a flat crystal to select the x-ray emission. As we have already discussed, a crystal reflects x-rays satisfying the Bragg condition $2d \sin\theta_B = n\lambda$. For a point-like source, each point of the crystal reflects a specific wavelength, allowing their spatial separation resulting in a x-ray spectrum. Following the scheme represented in figure **??** we obtain the following relation:

$$\sin\theta = \frac{a}{\sqrt{a^2 + x^2/4}}. \tag{3.15}$$

Coupling this equation together with the Bragg relation we obtain the spectral dispersion for a flat crystal

$$E = \frac{nhc}{2da}\sqrt{a^2 + \frac{x^2}{4}}. \tag{3.16}$$

Taking the differential of equation **??** and dividing it by E, we obtain the spectral resolution of the spectrometer:

$$\Delta E = \frac{nhc}{2da}\frac{x}{4}\left(a^2 + \frac{x^2}{4}\right)^{-1/2}\Delta x \tag{3.17}$$

$$\frac{\Delta E}{E} = \frac{x}{4a^2 + x^2}\Delta x. \tag{3.18}$$

In general, a flat spectrometer has a quite low reflectivity, that makes

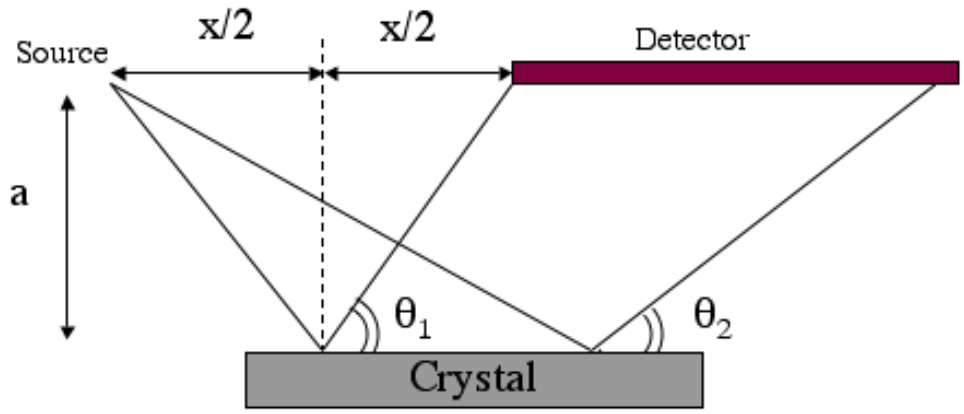

Figure 3.14: **Schematic of the flat crystal spectrometer concept.**

it suitable for experiments at relatively low laser intensities and energies. For petaWatt class laser interacting with plasmas, signal-to-background and signal-to-noise ratios will be very low for flat spectrometers, affecting the quality of the measurements. Therefore, a new crystal design, providing high reflectivity, is required. The Highly Oriented Pyrolytic Graphite crystal guarantees high reflectivity maintaining a relatively high spectral resolution.

Highly Oriented Pyrolytic Graphite spectrometer (HOPG)

The HOPG is a particular case of flat spectrometer in which the crystal is constituted by a mosaic structure of crystalline grains, which plane orientation is randomly distributed around the normal axis to the surface [**?**]. The

mosaic spread γ_s is defined as the full width half maximum of a Gaussian distribution of crystal plane orientations. Typical values for γ_s range from 0.4° to 3.5°. The random distribution of scattering planes of the crystal allows x-rays to always find a plane at the correct Bragg angle and to be refocused on a single point at the image plane, therefore increasing the total reflectivity of the crystal. This focusing property is called *mosaic focusing*, and is similar to the way a spherical crystal spectrometer focuses the x-rays at the image plane. The crystal grains can are indeed distributed on a Rowland circle, and the HOPG is aligned keeping the point source and the image distances equal ($p = q$) allowing therefore monochromatic x-rays will be focused on a single line in the image plane . The spectral resolution of the crystal is quite limited compared to classic flat spectrometers ($\Delta E/E = 10^4$) and typically ranges between 1 and 3×10^{-3}.

3.3.8 Transmission Crystal Spectrometer (TCS)

The transmission crystal spectrometer allows to perform spectroscopic measurements over a very large range of x-ray energies, including the hard x-rays emitted by high Z ions such as Au $K\alpha$ ($\sim$ 70 keV). It is based on a Cauchois type geometry [**?**], featuring a cylindrical crystal working in Rowland circle configuration. Differently from the Bragg crystal introduced in the previous section, the atomic planes of the TCS crystal taking part in the x-ray diffraction, are disposed perpendicularly to the surface, in Von Laue configuration. In figure **??** is represented the scheme of the transmission spectrometer. The x-rays of energy E emitted by the source and satisfying the Bragg condition, are diffracted by the crystal in c. The diffraction takes place in two opposite regions of the crystal, due to the intrinsic sagittal symmetry of the spectrometer geometry. For each x-ray energy, two lines are formed in the image plane, at distance X_D from the axis of symmetry. It is possible to geometrically calculate the position of the spectral lines in the limit for small angles and supposing a point-like source. Under these

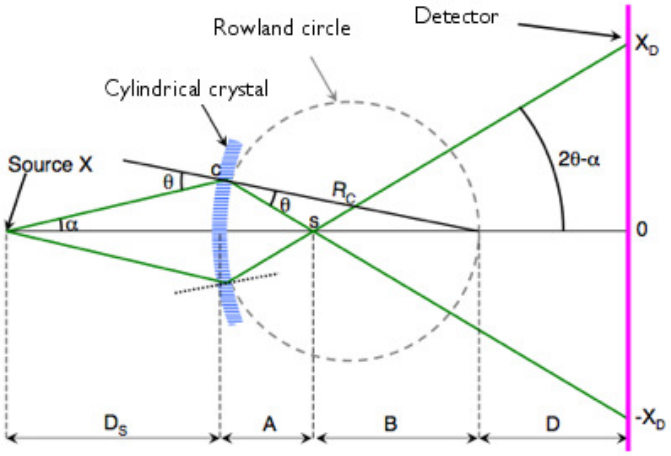

Figure 3.15: **Couchois type transmission spectrometer geometry.**

conditions, the spectral dispersion is given by:

$$E = \frac{nhc}{2dX_D} R_C \left(1 + \frac{D}{B}\right), \tag{3.19}$$

where B is given by:

$$B = R_C - A = R_C - \frac{R_C D_S}{R_C + 2D_S} = R_C \frac{R_C + D_S}{R_C + 2D_S}. \tag{3.20}$$

From equation **??** we can obtain the spectral resolution

$$\frac{\Delta E}{E} = \frac{2dE\Delta X_D}{nhcR_C} \frac{B}{B + D}, \tag{3.21}$$

where ΔX_D is the resolution of the detector, limited in our case, by the scanning resolution of the image plate (50μm). Equation **??** expresses an important feature of the spectrometer: the position s given by the distance A doesn't depend on the angle θ nor by the x-ray energy. In other words, all the x-rays satisfying the Bragg condition will pass by the point s. This allows to spatially filter the background noise with a lead slit at s, eliminating the

most of it. In our experience we adopted the following parameters for the spectrometer: Quartz crystal $10\bar{1}1$, $2d = 6.687\mathring{A}$, $R_C = 254$ mm, $D_S = 600$ mm, $A = 104.8$ mm $D = 0$ or 200 mm. Figure **??** shows the spectrometers theoretical dispersion curves for the parameters above. The detector can be positioned on the Rowland circle ($D = 0$ mm) or at a distance D from it, improving the spectral resolution, reducing the at the same time, the signal intensity.

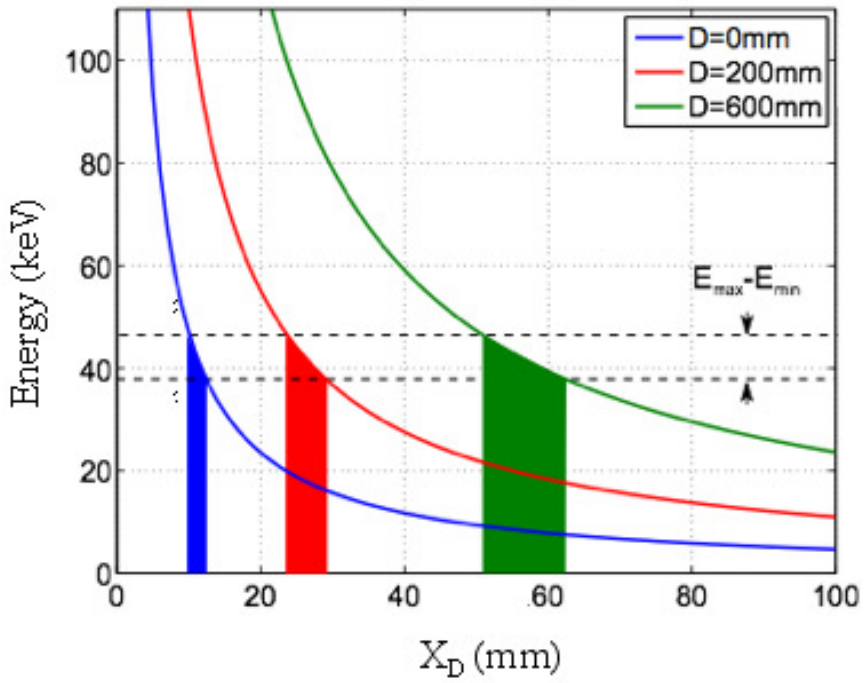

Figure 3.16: **Theoretical spectral dispersion curves for the Cauchois spectrometer. $D = 0$ indicates the Rowland circle, $D = 200$ and $D = 600$ mm behind the Rowland circle. The larger is D the larger is the thickness of the lines on the detector.**

3.3.9 Bremmsstrahlung cannons

The Bremmsstrahlung cannon [**?**] is a spectrometer that allows to measure the bremmsstrahlung emission produced by fast electrons in their propaga-

tion inside the target. Differently from $K\alpha$ emission, which is a line emission, the bremmsstrahlung radiation is characterized by continuous spectrum, decreasing as function of the x-ray energy.

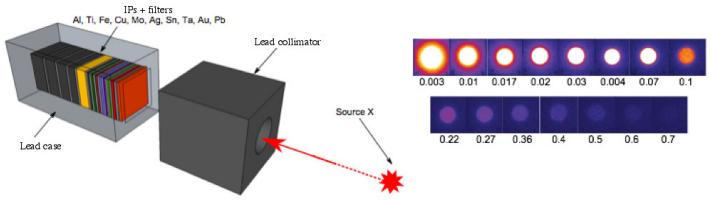

Figure 3.17: **(left) Schematic of the Bremmsstrahlung cannon. (right) Example of experimental data, the numbers corresponds to the energy of the transmitted x-rays (MeV).**

The basic principle of this spectrometer is to attenuate the x-ray emission by using different metallic filters, each of them followed by an x-ray detector called Image Plate (IP). The signal deposited on the IPs is then analyzed. Knowing the absorption of each filter, is in principle possible to reconstruct the bremmsstrahlung spectrum, and, from this spectrum, estimate the fast electron energy spectrum and divergence. However, the latest step is not straightforward, since the fast electron spectrum can be reconstructed only using collisional or hybrid simulations (with collisions package), modulating the fast electron source in order to replicate the experimental data. The spectrometer adopted in our experience is composed by 15 filters, separated by 250μm Mylar foils to minimize the effect of secondary electrons. The first 9 filters are arranged in in increasing Z (Al, Ti, Fe, Cu, Mo, Ag, Sn, Ta, Au) and the remaining 6 are made of Pb with increasing thickness (1, 2, 3, 4, 5 and 6 mm). The stack of IPs and filters is positioned in a lead case to reduce the background noise. In front of the spectrometer is placed a lead collimator to limit the fluorescence radiation.

3.3.10 Image plate detector

Image plate detectors were primarily used as detector for the x-ray diagnostics and the electron spectrometer diagnostic in the experiments. This

detector and the relative scanner are commercial products, the image plates adopted were Fuji TR and FUJI SR, and the scanner was a Fuji FLA-7000. The plate is composed by a 100μm BaFBr:Eu^{+2}, which is a fluorescent material. The Europium ion is excited by the ionizing radiation energy into a metastable state, with an extremely low de-excitation rate, keeping the information stored even for days.

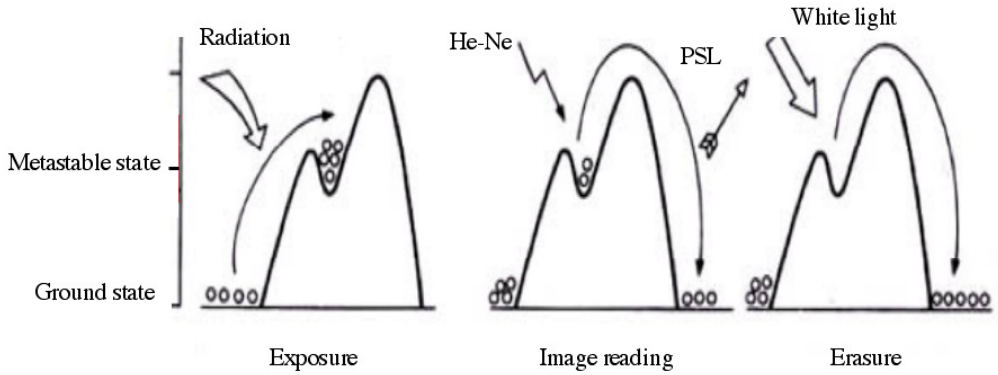

Figure 3.18: **The photo-stimulated luminescence process.**

The information is extracted using a scanner, which uses a helium neon laser that excites the Europium to a higher, but not metastable, state. The Europium then de-excites emitting a photon, this process is called *photo-stimulated luminescence* (PSL). The emitted photon is then collected into a photo-multiplier and the number of photons collected is directly proportional to the energy stored in the detector layer. A very important characteristic of the IP detector is its reusability, the stored information can indeed be deleted by exposing the IP to incoherent visible light for about 20 minutes. Moreover, the detector is constituted by large foils, that can be cut according to the experimental needs, guaranteeing versatility and large detection areas.

3.4 Diagnostics for ion beam generation studies

Ion beams are generated at the target surface by space charge electric field produced by the fast electrons expanding into vacuum. Therefore no x-ray or visible light emission is directly related to the acceleration of ion beams, and the diagnostics usually adopted in experiments are magnetic spectrometers, Thomson parabola spectrometer, radio-chromic films (RCF) and CR39 detectors. We concentrate our attention on the RCF diagnostic, used in the experiment exposed in chapter **??**.

3.4.1 Radio-chromic films (RCF)

The RCF is a dosimetry film [**?**], with a multi-layer structure composed by a gelatin surface layer, an active layer and a Polyester substrate. The active layer is composed by a dye, triphenyl methane dye cyanide, that undergoes a chemical reaction when exposed to ionizing radiation, turning from transparent to blue. The optical density of the active layer is directly proportional to the dose deposited, and for very high radiation fluxes the density may saturate, therefore not corresponding anymore to the deposited dose. Used as ion diagnostic, the RCF are usually arranged in stack, providing an estimate of the ion energy spectrum, calculated from the dose deposited on each subsequent film, and of the ion maximum energy, corresponding to the proton energy required to deposit dose on the last marked film in the stack. The type of RCF used in our proton acceleration experience is Gafchromic HD-810, with single active layer, see figure **??**.

To better understand the RCF data and their relation to the proton energy spectrum, is necessary to introduce the concept of ion stopping power in cold matter.

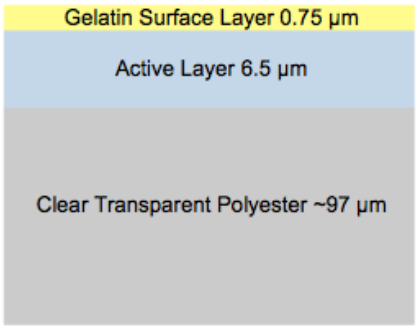

Figure 3.19: **Schematic of the Gafchromic HD-**810 **RCF.**

Ion stopping power

The ion stopping power in cold matter can be expressed by the expression:

$$-\frac{dE}{dx} = N\sum_{n}(E_n - E_0)\int \frac{d\sigma}{dq}dq \tag{3.22}$$

where N is the ion number density, and $d\sigma/dq$ is the differential cross section for the fast ion to raise the atomic energy level from the ground state E_0 to E_n with momentum transfer hq. Following the work in [**?**], the ion stopping power in matter becomes

$$-\frac{dE}{dx} = \frac{4\pi NZ}{m_e}\left(\frac{ze^2}{v}\right)^2 \ln\frac{2mv^2}{\langle E_n - E_0\rangle} \tag{3.23}$$

where z is projectile particle charge, v its velocity and $\langle E_n - E_0\rangle$ is a semi-empirical parameter, determined through experiments, representing an average of energy transfer per fast ion interaction with atoms. In general the energy deposition in matter is characterized by a peak, called Bragg peak: ions with a certain energy E , traversing a medium , release the most of their energy at a very well determined depth x in the target sample, resulting in a peak in the stopping power. This remarkable characteristic of ion beams makes them very suitable for medical applications, such as cancer therapy. Modulating the ion energy spectrum, is possible to reduce the dose

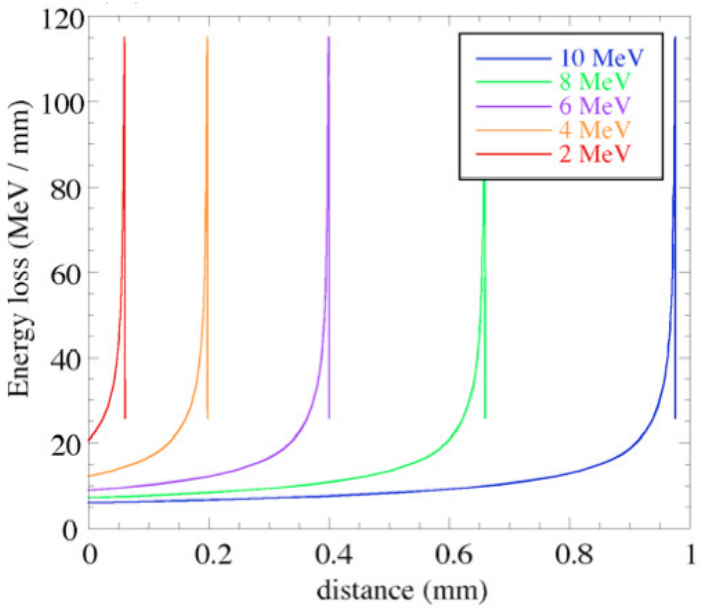

Figure 3.20: **Proton stopping power in polymer versus penetration depth in the target sample.**

deposited on the healthy tissues and concentrate it in the tumor, reducing the side effects of radiotherapy.

Chapter 4

Fast electron transport in resistivity gradients

Fast Ignition, despite its conceptual simplicity, is a very complex problem, involving a large number of yet unknown parameters, which knowledge is fundamental for the proper modeling of a point-design, necessary step to verify the feasibility of the concept itself. Indeed, for example, the amount of ignitor beam energy, required to trigger thermonuclear burst in compressed DT fuel, is determined by fundamental factors such as the initial fast electron energy spectrum and divergence, resulting from the LPI process, as well as from the divergence and energy loss of the hot electron beam, traveling from the critical surface to the compressed core. Fast electron transport experiments, in this sense, might not seem directly relevant for Fast Ignition, since the laser parameters available nowadays are absolutely non-comparable to those of the ignitor beam. This implies that the information deriving from our experiments cannot be, by any mean, directly scaled to a real Fast Ignition scenario. What is then the utility for these experiments?
First of all, in a relatively small scale experiment, is possible to actually observe physical phenomena and validate theories related to the fast electron generation and transport. It is also possible to develop and test new diagnostics, to be implemented on large facilities. But the most important reason to perform experiments on fast electron generation and transport is

related to code validation. If we are able to reproduce, not only qualitatively but quantitatively, a wide variety of experimental results with our simulation codes, we can be more confident that, once scaling the parameters to a real FI scenario, the results will be close to the real ones in a FI experiment, allowing to build a reliable FI point design and verify the feasibility of the FI itself.

Let's focus now our attention on this chapter's topic, related to the study of fast electron transport.
The physics of fast electron transport is, as we already exposed in this work, a very complex process involving collisional and collective effects. In particular, in FI, the fast electrons are required to propagate from the critical surface up to the isochorically compressed fuel, crossing a plasma which properties of density and temperature are rapidly changing approaching the dense core. A very recent experiment, conducted on Titan laser at JLF, studied the fast electron transport in warm dense Aluminum. The compression and heating of an Al transport layer was produced by a shock driven in the target sample. The generated warm dense Al state has different properties from the cold solid Al state, in particular regarding the density and the resistivity of the medium, affecting the fast electron transport through collisional and collective effects.
The original idea was to use a planar shock geometry allowing to discriminate between collisional and collective effects in fast electron transport. Collisional stopping effects, indeed, are directly proportional to the target areal density crossed by the fast electrons, which remains constant under planar compression of the target, while the resistivity of the medium changes, determining different collective stopping effects. More specifically, Al at average density of $2 \times \rho_0$, with ρ_0 being the uncompressed Al solid density, and 2 eV average temperature, presents a higher resistivity than cold Aluminum. This implies, at least transiently, a higher collective stopping power compared to cold uncompressed Al. These effects were already observed and widely explained in [**?**], as result of an experience at LULI 2000 Laser facility . The exceptionality of performing again such experiment at Titan laser resided in the wider range of parameters that could be scanned on this facility, in particular

regarding the higher fast electron current density available on Titan, related to the much higher short pulse energy, compared to the LULI 2000. Given the good characterization of Titan laser in terms of pre-pulse level and the intensity distribution in the focal spot, it represents an ideal source to be used to estimate the accuracy of the simulation codes available.

4.1 Experiment at Titan laser, JLF

The purpose of the experiment is to study how the fast electron transport would be affected by an increase in resistivity in the transport material (Aluminum in our case). As shown in figure **??**, the resistivity for solid density (2.7g/cm^3) Al rises from room temperature and reaches its maximum for temperatures close to the Al Fermi temperature (11.7 eV), before decreasing again as the plasma conditions attain the Spitzer regime. The increase in temperature is produced by a long ($\sim$ 5 ns) laser pulse, focused on the target rear surface, driving a planar shock in the solid Al, compressing it to about $2\rho_0$ and heating it to temperatures $\sim$ 3 eV. A fast electron beam is produced focusing a high intensity laser pulse ($\sim 3\times10^{20}\text{W/cm}^2$ peak intensity) on the target front surface. This experimental design allows to discriminate between collisional and collective effects in the fast electron transport. The collisional effects are indeed directly proportional to the target areal density ρz, which is constant in case of planar compression of the target. The differences in the fast electron transport have therefore to be attributed to the collective effects related to the change in resistivity between compressed and uncompressed targets [**?**].

4.1.1 Laser specifics

The Titan short pulse (SP) and long pulse (LP), have been operated simultaneously in the experience.
The frequency doubled LP beam, $\lambda = 0.53\mu$m, was used to compress the target and delivered $\sim$ 160 J in 5 ns, with square temporal profile. The requested random phase plate (RPP) for the experience was 600μm. For

technical reasons instead the only RPP available produced a $180 \times 150\mu$m spot size giving an average intensity of 1.4×10^{14} W/cm^2 . Due to RPP defects, the intensity profile of the LP spot was far from "flat top", presenting several inhomogeneities and hot spots.
The SP beam was used to generate the fast electron beam. It delivered 120 J in 0.7 ps with $\lambda = 1.06$ nm. It was focused by a f/3 off-axis parabola on the target front surface, in $\sim 10\mu$m spot size containing the 50% of the laser energy and resulting in a peak intensity of $\sim 10^{20}$ W/cm^2.

4.1.2 Experimental setup

The laser pulses were focused on multi-layer targets, composed by a 5μm Al layer on the front, followed by a 5μm Ag layer, an Al transport layer of variable thickness: 20, 40, 60 and 80μm, 10μm Sn layer,10μm Cu layer and finally a 15μm polypropylene ablator layer on the target rear. The SP is focused on the first Al layer, guaranteeing the same LPI for all targets. The Ag layer has the function of characterize the fast electron source in terms of number of electrons produced, via the measurement of the Ag-$K\alpha$ with the TCS spectrometer. The Cu and Sn layers are used as diagnostic for fast electron transport in the intermediate Al layer. In particular, the Ag-$K\alpha$ normalized Cu and Sn-$K\alpha$ yields give relative information on the fast electron stopping in the Al transport layer.

All the diagnostics for fast electron transport used in the experiment are x-ray based and are composed by

- A $K\alpha$ imager looking at the target rear side. with an angle of 40° to the target normal. The crystal is a spherically bent Quartz $21\bar{3}1$, with 50 cm curvature radius and $2d = 3.082\mathring{A}$, reflecting the Cu-$K\alpha$ at 88.7° Bragg angle. The plastic covered lead aperture diameter was 15 mm and the measured spatial resolution was about 20μm. The crystal was used to image the Cu-$K\alpha$ produced by the fast electron beam transport in the target.

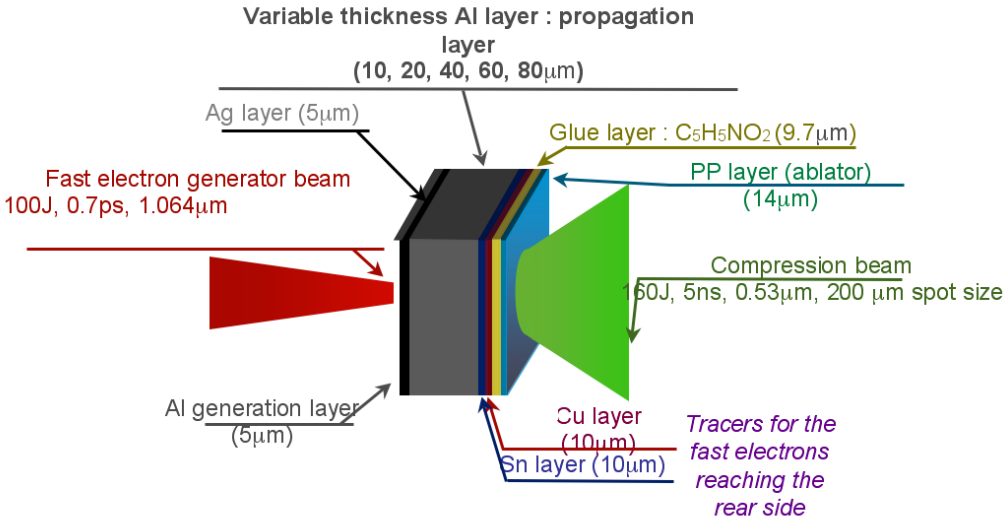

Figure 4.1: **Schematic of the target adopted in the experience.**

- A double channel HOPG (DC-HOPG), looking at the target rear and collecting the Cu and Ag-$K\alpha$ signals.
- A TCS spectrometer looking at the target rear side and collecting the Ag and Sn-$K\alpha$, signals.
- Bremmsstrahlung cannons, looking at the target rear side, at 45 and 75° from the target normal.
- A Von-Hamos crystal spectrometer with high spectral resolution, recording the Cu-$K\alpha$ emission from the Cu tracer layer.
- A KB microscope [**?**], looking at the target rear side with an angle of 35° to the target normal, and imaging x-rays in the range 4-9 keV.

4.1.3 Compressed targets

The timing between SP and LP must be adjusted for each type of target in order for the shock to propagate through the most of the Al transport layer,

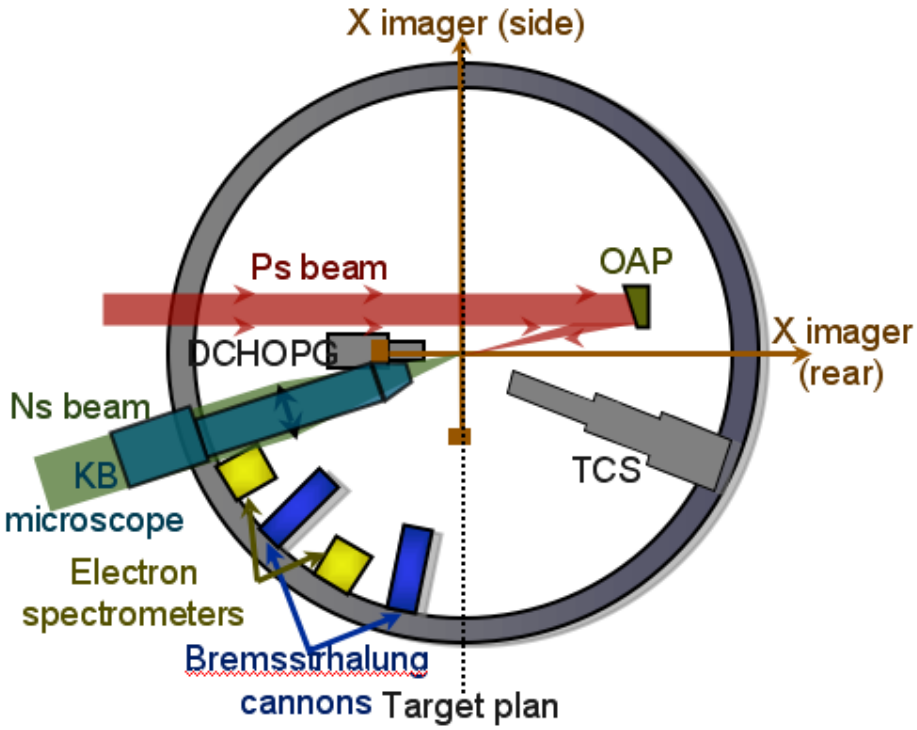

Figure 4.2: **Experimental setup at Titan laser.**

before the fast electron generation by the SP. Unfortunately, for technical issues, we couldn't use the SOP diagnostic in our experiment and the shock-breakout time from the Al transport layer was found via Hydro-simulations using the code CHIC [**?**]. The Hydro simulations were performed considering 300 J on the LP beam. Scaling laws were finally used in order to take into account the real LP beam energy of 150 J.

$$t_B = t_{B-300J} \left(\frac{300}{E_{LP}} \right)^{1/3} . \tag{4.1}$$

Fast electron transport in uncompressed targets was also studied for comparison. In this case, a constant delay of 1.9 ns between SP and LP was adopted, preventing the shock from reaching the Al transport layer but allowing to create a large scale length plasma on the target rear side. In the shock compressed targets, indeed a large scale length plasma expanding from

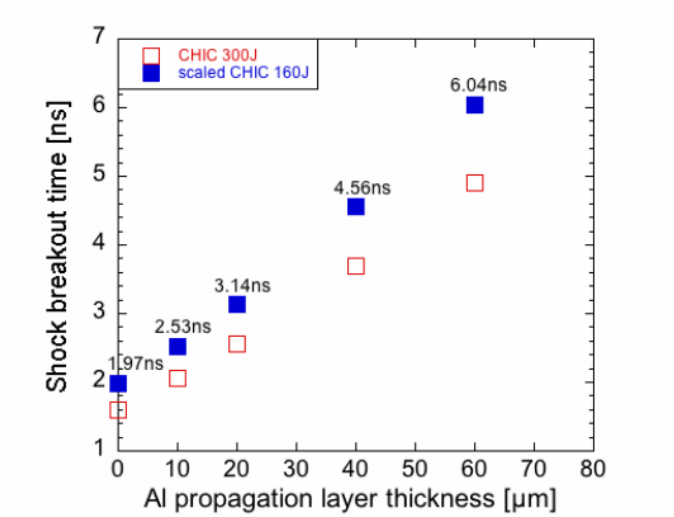

Figure 4.3: **Shock breakout time versus Al propagation layer thickness.**

the target rear side strongly reduces the fast electron refluxing by reducing the space charge fields. The LP beam was therefore used for all shots in order to keep similar fast electron transport conditions. The density and temperature profiles for all targets, taken on the axis of symmetry ($R = 0$ in cylindrical coordinates) are represented in figure **??**. However, using an RPP providing a LP spot size $\leq 200\mu$m, the profiles displayed in figure **??** have to be considered only as approximations on the axis of symmetry, The LP, indeed, produces a non-planar compression of the target, introducing density and temperature gradients not only in the longitudinal but also in the radial direction. Thus 2D effects cannot be dis-regarded in the modeling of the experiment. 2D hydrodynamic simulations using the code CHIC have been performed to obtain the correct density and temperature profiles. As an example, 2D simulation results for a 60μm Al transport layer targets are presented in figure **??**.

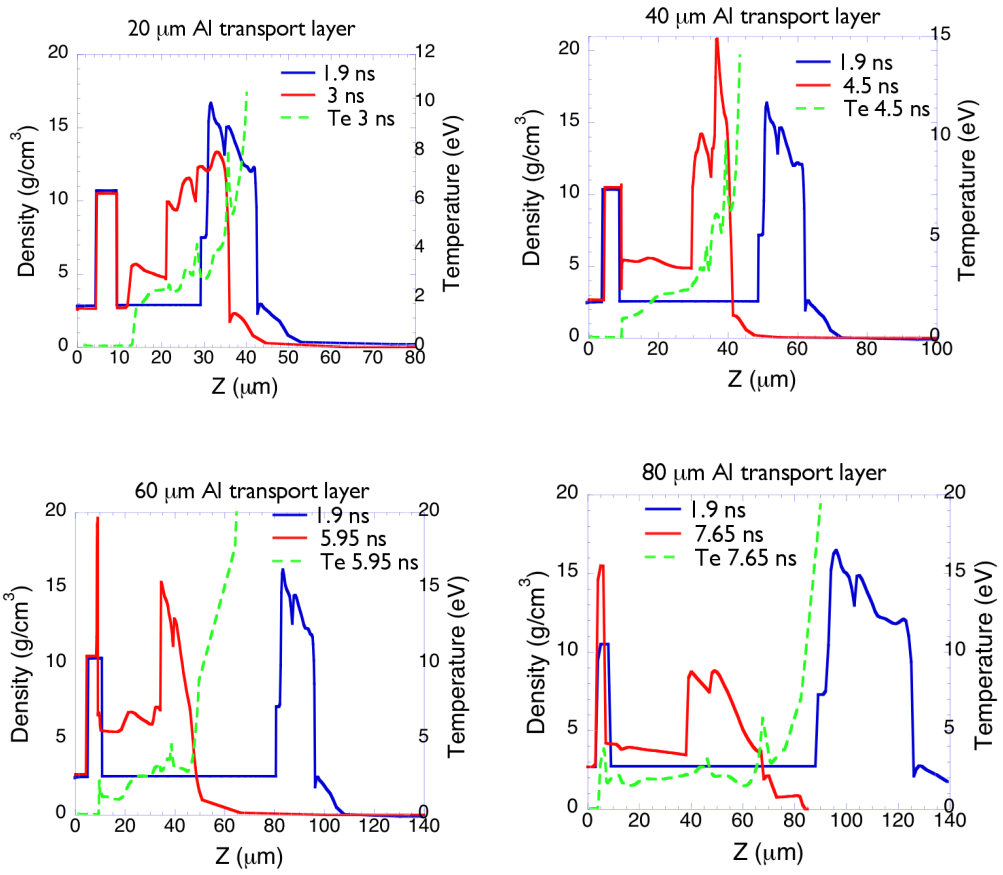

Figure 4.4: **Density and temperature profiles for uncompressed and compressed targets corresponding to the time the SP beam is focused on the target front side.**

4.2 Experimental results

4.2.1 $K\alpha$ imager and KB microscope data

The $K\alpha$ imager gives a 2D-spatially resolved image of the $K\alpha$ emission related to the transport of the fast electron current through the Cu tracer layer. In this experience, a very large difference in the $K\alpha$ spot size has been observed for compressed and uncompressed targets. In particular, a very large $K\alpha$ spot has been observed for shock compressed targets. Result rather un-

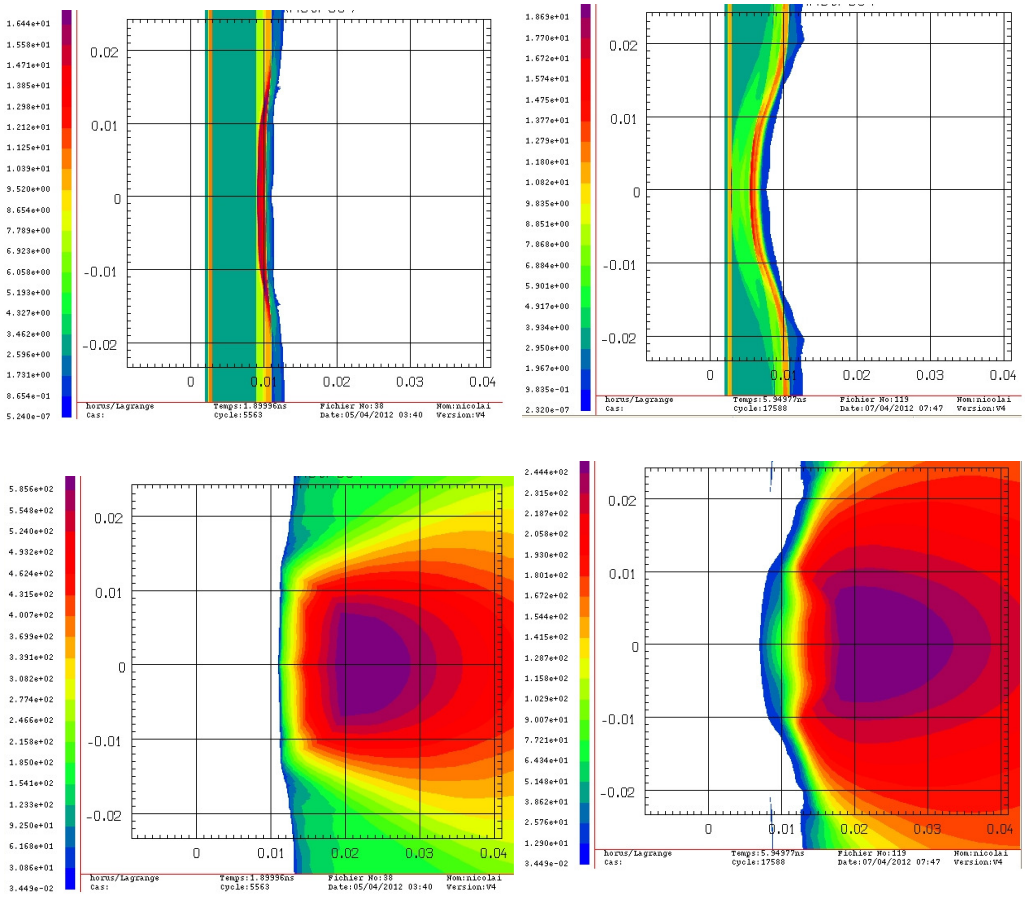

Figure 4.5: **Density and temperature profiles for uncompressed (left column) and compressed (right column) 60μm Al transport layer targets, obtained from CHIC simulations, corresponding to the time the SP beam is focused on the target front side.**

expected according to previous analogous experiments [**?**] [**?**]. This effect is consistently observed by the $K\alpha$ imager and the KB microscope, with spot sizes largely greater than 200μm for initial Al transport layer thicknesses $\geq$ 60μm, while in the uncompressed case, both diagnostics give results in agreement with measurements on fast electron divergence found in literature.

The results for $K\alpha$ imager and KB microscope are represented in figure **??**, and in figure **??** is represented the shot-to-shot correlation between the two

diagnostics. The fast electron divergence is calculated taking into account the Al layer realistic thickness as it comes from the hydro simulations. This is, of course, an approximation since the Al thickness considered is relative to the axis of symmetry of the compressed target ($R = 0$ in cylindrical coordinates), while we are indeed dealing with a bi-dimensional geometry. If we assume that the $K\alpha$ measured spot size in this experiment is truly an effect of fast electron divergence, the fast electron divergence measured from the $K\alpha$ and the KB data are respectively $155 \pm 12°$ and $152 \pm 10°$ full angle for the compressed case and for the solid case $40 \pm 5°$ and $36 \pm 4°$ full angle. These values of divergence for fast electron transport are extremely large compared to those ever found in literature, and the explanation of these data, which constituted a large part of my work, represents a very intriguing problem, which may have interesting consequences for Fast Ignition point design research.

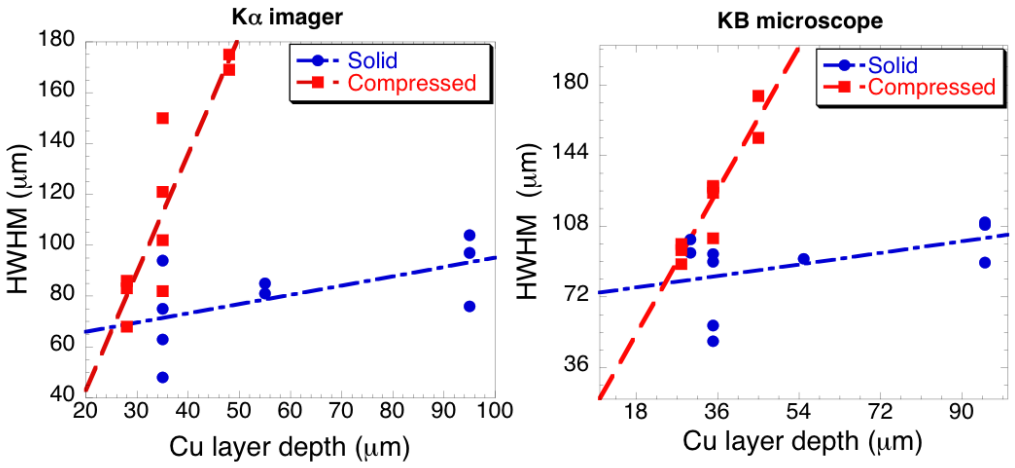

Figure 4.6: $K\alpha$ **imager (left) and KB microscope (right) measurements of** $K\alpha$ **spot size. The data from the two diagnostics show a strong correlation, supporting the evidence of large divergence. The divergence measured from** $K\alpha$ **imager and KB microscope are respectively** $155 \pm 12°$ **and** $152 \pm 10°$ **full angle for the compressed case and for the solid case** $40 \pm 5°$ **and** $36 \pm 4°$ **full angle.**

4.2.2 X-ray spectroscopy results

The x-ray spectroscopy data, instead do not show any peculiar behavior for compressed samples as the x-ray imagers do. The results are instead in line with the previous experiments cited above. In particular if we focus our attention on the Ag-$K\alpha$ normalized Cu and Sn-$K\alpha$ yields, which is related to the energy loss of the fast electron beam crossing the Al transport layer and, at the same time, is immune from shot to shot variation, we do not observe striking difference between solid and compressed Al. The Sn-$K\alpha$/Ag-$K\alpha$ ratio suggests higher fast electron energy losses in compressed material, more evidently for thick Al transport layers as expected from the model discussed in [**?**], but the overall signal decrease is simply related to the fast electrons propagating deeper into the target material and releasing their energy along the path. The experimental results are shown in figure **??**.

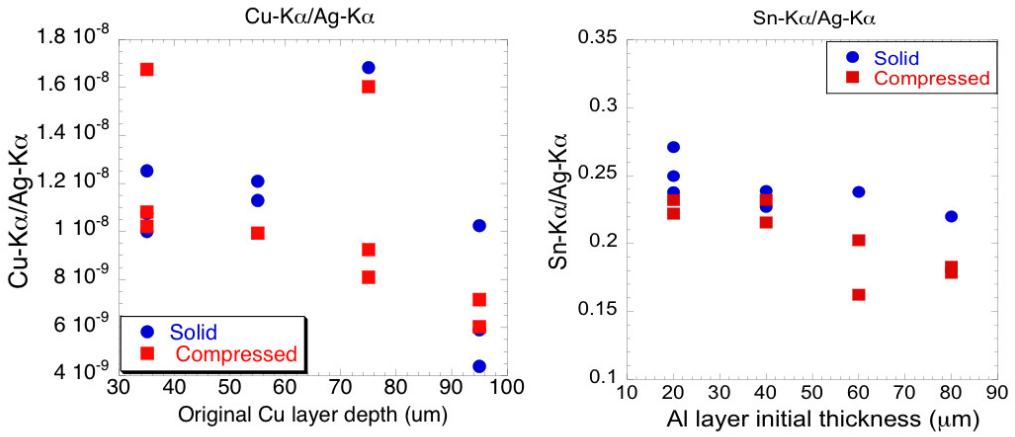

Figure 4.7: **Ag-$K\alpha$ normalized Cu-$K\alpha$ (left) yield and Sn-$K\alpha$ (right) yield. The Ag and Sn-$K\alpha$ yields are obtained from the TCS diagnostic, while the Cu-$K\alpha$ yield is measured by the HOPG spectrometer. The Cu-$K\alpha$ yield is measured in Photo Stimulated Luminescence (PSL)/steradian units, while the Ag and Sn$K\alpha$ yields in photons/steradian units.**

4.3 Resistivity gradients induced fast electron divergence

The very large fast electron divergence observed in presence of shock compression of the target is an effect not observed in any of the previous experiments on fast electron transport in warm dense aluminum. In my recent PhD work, I focused my attention on trying to explain this effect, and to find out wether there could be some analogy in the broader picture of the Fast Ignition research.

The two fundamental differences between the JLF experiment and previous works are the non-planar shock, related to the small LP focal spot and the larger fast electron current density, related to the higher energy of the Titan short pulse. In particular, the presence of a non-planar compression introduces density and temperature gradients in the longitudinal as well as in the radial direction. These gradients may act on the fast electron current in such a way to deflect the fast electron trajectories and determine a broader divergence. Also, the higher fast electron current density may amplify these effects. We expose in this section a model describing collective effects related to fast electron transport in density gradients.

4.3.1 Fast electron induced magnetic field in presence of density gradients.

The plasma resistivity can be described, in first approximation, by the classic Drude model as follows:

$$\eta = \frac{m_e \nu}{e^2 n_e}. \tag{4.2}$$

As we already discussed is section **??**, the collision frequency model is strongly dependent on the plasma conditions, and in particular on the plasma temperature. In the temperature range of our interest, which is included between the melting point and the Spitzer regime, the collision frequency is limited by the cutoff frequency ν_c, expression of the fact that the electron mean free path λ cannot be smaller than the interatomic distance r_0. The

upper boundary for the frequency ν_c can be expressed as:

$$\nu_c = \frac{v_{th}}{r_0} = v_{th}\left(\frac{4\pi n_i}{3}\right)^{1/3}, \tag{4.3}$$

where v_{th} is the electron thermal velocity. Therefore, being $n_e = \bar{Z}n_i$ and noting that $(4\pi/3)^{1/3} \approx \pi/2$, we can write the plasma resistivity in the range of temperature of our interest as:

$$\eta = \frac{\pi}{2}\frac{m_e v_{th} n_i^{1/3}}{e^2 \bar{Z} n_i} = \frac{\pi}{2}\frac{m_e v_{th}}{e^2 \bar{Z} n_i^{2/3}}. \tag{4.4}$$

Therefore η depends on the ion plasma density as :

$$\eta \propto n_i^{-2/3}, \tag{4.5}$$

and the variation of η as function of the plasma ion density in cylindrical coordinated and disregarding the angular variable θ can be expressed as :

$$\partial\eta \propto -\frac{2}{3}n_i^{-5/3}\partial n_i(r,z) = -\frac{2}{3}n_i^{-5/3}\left(\partial_r n_i + \partial_z n_i\right). \tag{4.6}$$

Therefore, in this range of temperatures,the resistivity gradient is opposite to the density gradient: to higher density corresponds lower resistivity. This means that, after the dissipation of the temperature gradients due to the action of the fast electron beam, at the shock front the resistivity sharply reduces proportionally to the density increase, resulting in a sharp resistivity gradient. The relation between resistivity and density holds for all materials, as soon as the temperature ranges between their melting point and their Spitzer temperature (the Spitzer regime is attained at higher temperatures for higher Z materials). Figure **??** shows the LMD calculated resistivity for 2D-shock driven 80μm Al transport layer target equal to the sample represented in figure **??**, with constant temperature of 5 eV.

Following now the model exposed in [**?**], combining the Ohm's law

$$\mathbf{E} = -\eta \mathbf{J}_f ast \tag{4.7}$$

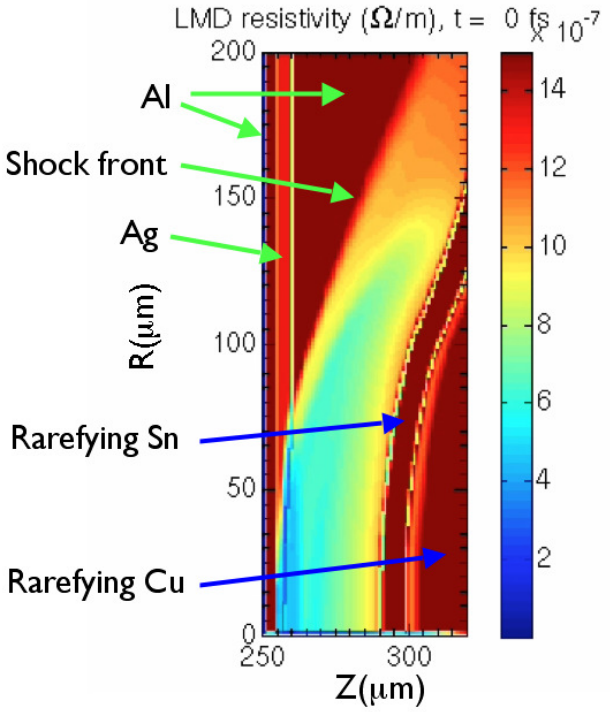

Figure 4.8: **Shock driven 80μm Al transport layer target. The resistivity of the different Z layers scales as their density. For Sn and Cu is higher because the layers are expanding as result of the rarefaction wave. The temperature is constant for all layers and equal to 5 eV.**

with the Faraday's law

$$\frac{\partial \mathbf{B}}{\partial t} = \eta \nabla \times \mathbf{J}_{fast} + \nabla(\eta) \times \mathbf{J}_{fast}. \tag{4.8}$$

The first term on the right hand side produces a collimating magnetic field pushing the electrons towards the high current density regions while the second term forces the fast electrons in the higher resistivity regions. We are obviously interested in the second term, since is related to the presence of resistivity gradients in the plasma. The component of the magnetic field, expressed in cylindrical coordinates, that causes the collimation/decollimation of an electron beam propagating along z direction with a certain angular dis-

tribution $\Omega(\theta) = 2\pi \sin\theta\Theta(\theta)$, is the azimuthal **B** field component B_θ. The angular distribution $\Theta(\theta)$ can be considered in first approximation as the ratio between the radial and the longitudinal components of the fast electron current density $\mathbf{J} = J_r\hat{r} + J_z\hat{z}$:

$$\Theta(\theta) \propto \frac{J_r}{J_z}. \tag{4.9}$$

Therefore introducing a fast electron angular distribution implies the presence of the two **J** components. Neglecting now the first term on the right hand side of equation **??**, the temporal variation of the B_θ component can be found as:

$$\partial_t B_\theta = J_r \partial_z \eta - J_z \partial_r \eta. \tag{4.10}$$

The contribution of the two terms on the right hand side of equation **??** determines the B_θ field growth rate. As we can see, the generation of the magnetic field is proportional to the resistivity gradients as well as the to the fast electron angular distribution, expressed by the magnitude of the J_r and J_z components. It is easy to verify that for a shock, planar or bi-dimensional, propagating along z, the B_θ component sign, produced by a fast electron beam with a certain angular distribution, is such that it has a de-collimating effect on the fast electron current. Our task now is to verify wether this effect is the cause of the large divergence observed in the experiment, replicating the experimental conditions on Titan laser in a set of hybrid simulations.

4.3.2 Hybrid simulations of fast electron transport

Once developed the analytic model and verified that the underlying physics qualitatively meets our hypothesis on the cause of the large fast electron divergence, we performed 2D-hybrid simulations using the Lsp [**?**] hybrid code in order to try to obtain quantitative agreement with the experimental data. As remark, this work represents a sort of milestone in the usage of the Lsp code, since never before simulations involving multilayer targets, density and temperature gradients, and the usage of equation of state for all materials, have ever been performed. This work required a huge effort in terms of time

and tentatives, and took the capabilities of the code at the extreme.
In order to verify the wether we could replicate the experimental results obtained at JLF, the first simulated target was chosen to be the one that gave the largest difference in fast electron divergence from solid to compressed. As we already explained, the hydrodynamic profiles were obtained by hydro simulations using the code CHIC. The 2D hydrodynamic profiles were imported on Lsp layer by layer, in form of two 2D matrixes defining the pixel by pixel respectively the layer density and temperature. As an example, in figure **??** are reported the density profiles layer by layer for the compressed sample case.

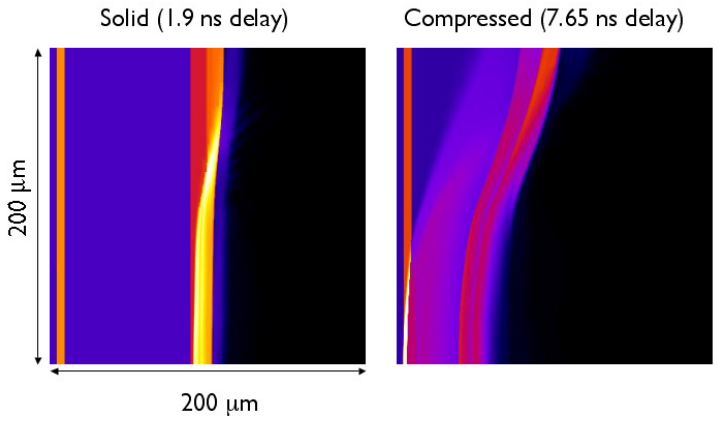

Figure 4.9: **Density profiles for solid and compressed 80μm Al transport layer target, in cylindrical coordinates as obtained from CHIC simulations. The color-scale is different for the two cases in order to improve the visibility of all layers.**

The ablated Carbon layer has subsequently been substituted for all simulations by a constant density (5×10^{22}cm^{-3}) and constant temperature ($T = 2$ eV) C foil, 400μm thick, in order to avoid numerical instability related to the usage of the LMD resistivity package in presence of a very low density plasma. The plasma ionization degree for each target material was calculated using the equation of state (EOS) tables PROPACEOS, and the x-ray generation, including $K\alpha$ and bremmsstrahlung, was obtained using cross section tables from the Monte Carlo collisional code ITS. The x-ray photon information

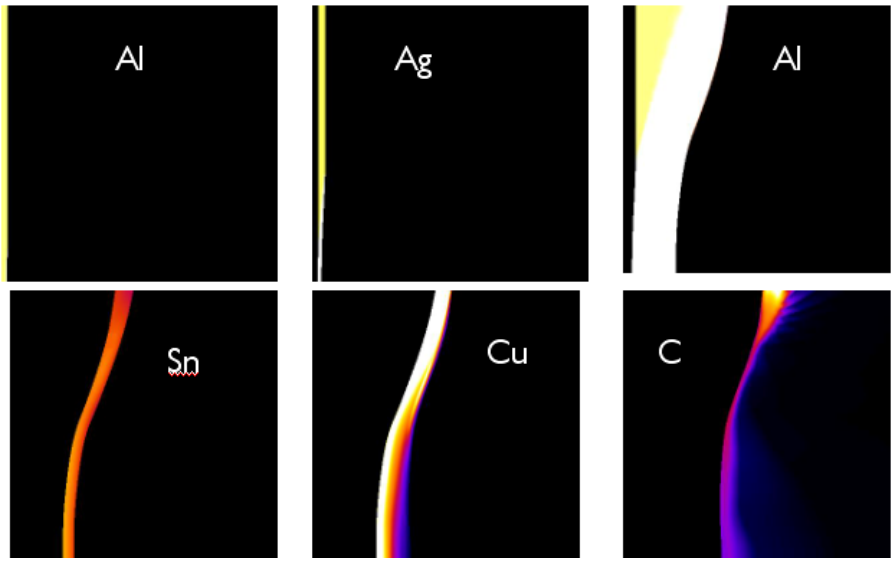

Figure 4.10: **Density profiles layer by layer for the compressed sample case. The color-scale is different for each layer.**

is collected into photon files, written at each data dump, containing the information on the generation coordinates, the photon energy and the photon propagation direction. The fast electron source was obtained from PIC simulations of laser plasma interaction, which laser and pre-plasma parameters were tuned according to experimental measurements on Titan pulse intensity distribution from the EPM diagnostic, temporal profile and pre-pulse measurement. The simulations were performed in cartesian coordinates and the results transformed in cylindrical geometry, introducing an uncertainty related to the absence of any mathematical solution for the transformation. The transformed fast electron source has therefore to be tested by trying to reproduce experimental results, in order to adjust the parameters related to the angular and energy distribution (see figure **??**). The fast electron energy and angular distribution for the Titan source are reported in figure **??**. The fast electron beam temporal profile can be approximated by a Gaussian with 0.7 ps full width half maximum pulse duration centered at 1 ps simulation time. The total fast electron energy injected is ≈ 60 J, the 80% of which is carried by fast electrons with energy ≥ 1 MeV, while the 80% of the current is

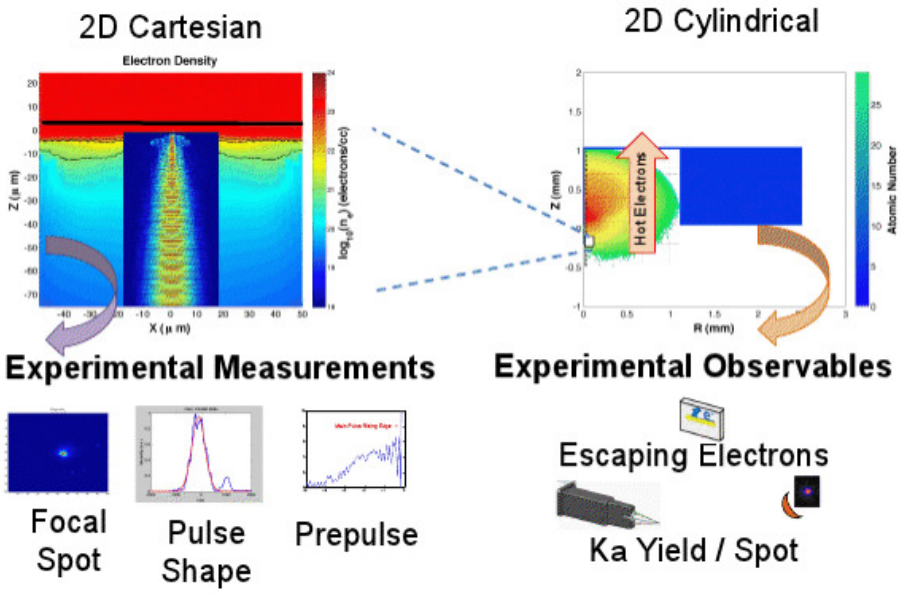

Figure 4.11: **Procedure adopted to obtain a reliable fast electron source replica in cylindrical coordinates. Image courtesy of Antony J. Link.**

carried by electrons with energy ≤ 1 MeV. The simulations were performed on a regular grid with 0.5μm spatial resolution and the time step Δt was chosen in order to respect the Courant condition $\Delta t \leq \Delta x/c$, where Δx is the size of the cell and c is the speed of light. The simulations were run for 3 ps simulation time, when the most of the fast electrons released their energy in the system or escaped the simulation box.

The requirement, for these simulations, of using temperature gradients starting from room temperature imposed to study the behavior of the LMD resistivity model, adopted by Lsp, over a wide range of temperatures, from room temperature up to 30 eV. To do so, I varied continuously the temperature of an Al layer, from 0.03 up to 30 eV and let the simulation run for 1 time step, obtaining from the EOS, the values of electron density and friction factor in any point of the aluminum slab. From these values the LMD resistivity was calculated and the result is displayed in figure **??**, where the resistivity

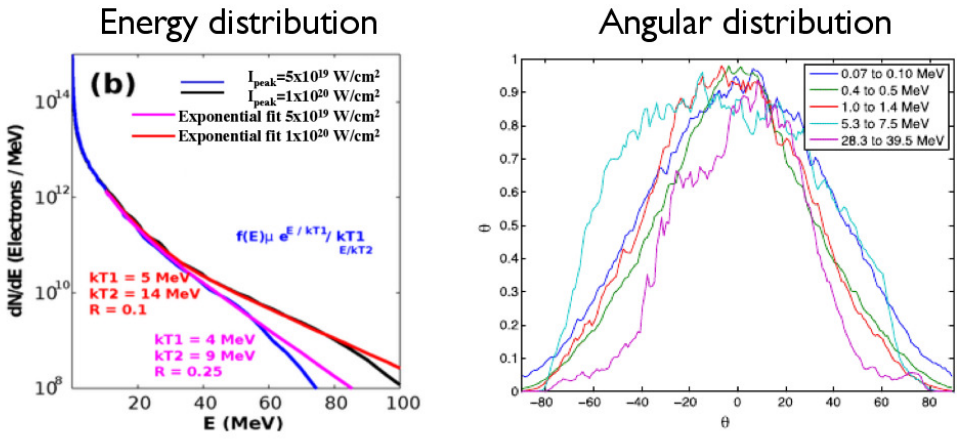

Figure 4.12: **Fast electron energy distribution (left) from PIC simulations using the Titan SP specifics, for two laser intensities and energy resolved fast electron angular distribution (right) relative to the laser peak intensity of 10^{20} W/cm^2. Image courtesy of Antony J. Link.**

is compared to the one calculated using the Eidmann-Chimier model. It

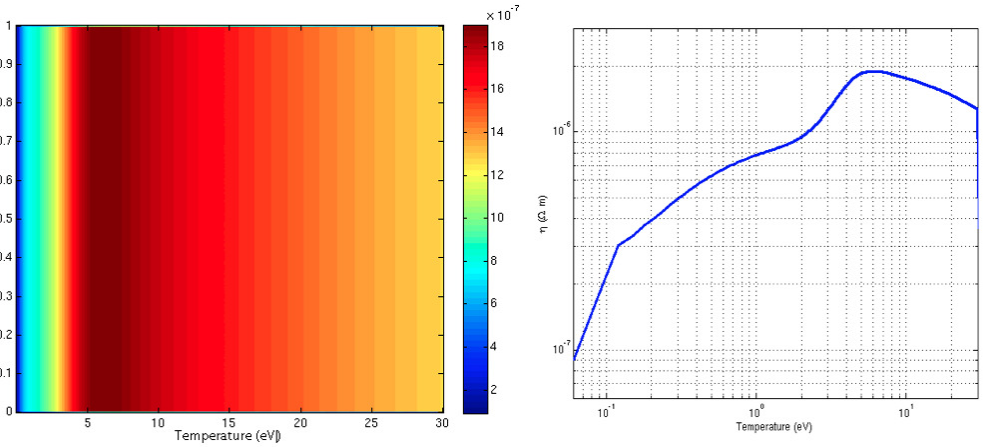

Figure 4.13: **LMD calculated resistivity plot in Al (left), with temperature continuously increasing from 0.03 to 30 eV. (right) Lineout of the LMD calculated resistivity.**

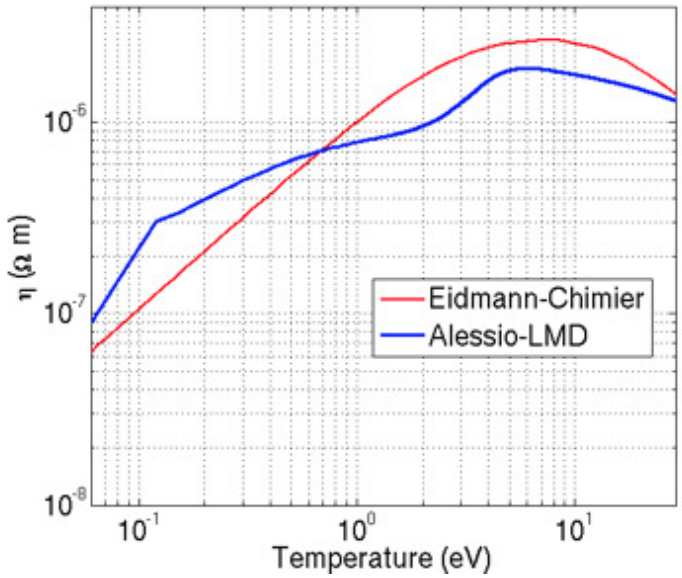

Figure 4.14: **Comparison between the LMD calculated resistivity from Lsp simulation and the Eidmann-Chimier model for Al in the same range of temperatures.**

appears that the LMD package on Lsp is able to replicate quite accurately the resistivity for Al, without discontinuities at the melting point. This measurement provided confidence that the values of plasma resistivity were reasonably replicated for a wide range of temperatures.

4.3.3 Simulation results for solid and compressed target samples

The simulation results for 80μm Al transport layer target do not match the experimental results in terms of fast electron divergence and approach the experimental results in terms of x-ray $K\alpha$ yields. The simulation results for solid and compressed target sample are displayed in a sequence of frames, since the plasma conditions, and therefore, resistivity gradients and magnetic field growth, evolve continuously during the fast electron injection. Figure **??** shows the density profiles of the two simulated cases.

Simulation of the solid sample target

The simulation results for the solid sample case is the most suitable to explain the various effects and aspects involved in the simulation.
Figure **??** shows the evolution of the LMD calculated resistivity as function of time for the solid sample case. The first frame, characterized by the title "0 fs", represents the initial target resistivity. The green line at the first interface Al-Ag is an image interpolation artifact and has no influence in the simulation. The resistivity for Al and Ag at room temperature is, as expected, very low. The Sn layer has naturally a very high room temperature resistivity, which is replicated in the simulation. The higher density and the ionization related to the shock front, as result of the 1.9 ns delay between the SP and the LP, to create the plasma "get lost" layer, reduces the Sn resistivity even if its temperature is increased. This behavior is different from the Al case. In driven Al, indeed, the action of the shock initially increases the resistivity compared to the cold solid density case, because even if the density is higher, the temperature of the shocked Al is large enough to determine a higher resistivity for the driven medium. In presence of a fast electron beam the Al resistivity gradient reverses with time, as result of the fast electron induced ohmic heating of the target sample, uniforming the temperature. The resistivity is then determined predominantly by the density of the medium. The Al behavior is followed by the Cu as well. The resistivity for driven Cu is indeed higher than its room temperature one. This aspect is also well reproduced by the simulation code. Finally the Carbon layer has a high resistivity, partially related to the naturally higher resistivity of Carbon, partially due to the constant density $5 \times 10^{22}\mathrm{cm}^{-3}$, which is lower than the C solid density ($\sim 10^{23}\mathrm{cm}^{-3}$) and to the 2 eV constant temperature.

At 750 fs simulation time, 250 fs before the peak of the Titan pulse injection, the fast electron beam transport produces the ohmic heating of the target material, increasing the resistivity of the two Al layers as well as the Ag layer. The fast electron current density layer is yet not high enough to produce significant plasma heating of the whole Al transport layer, which resistivity deeper in the target remains almost unchanged, as well as for Sn and

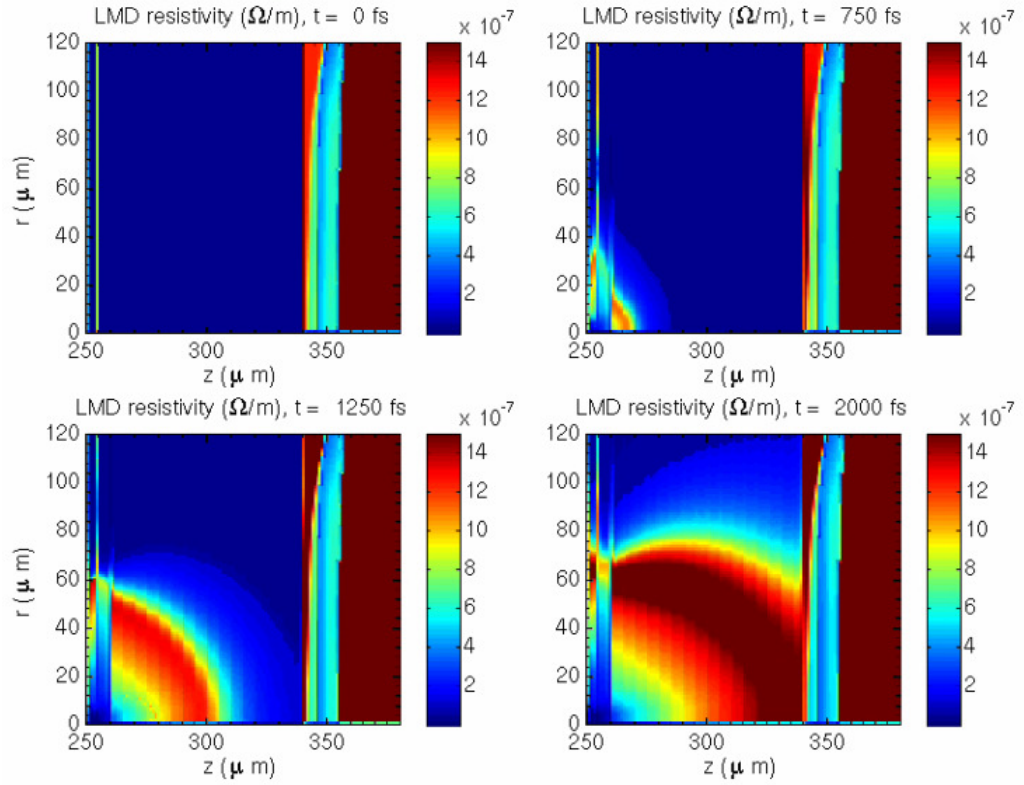

Figure 4.15: **Evolution of the LMD calculated resistivity as function of time. The plasma heating is produced by the fast electron beam.**

Ag. It is worth of notice that the plasma temperature close to the injection point (1μm inside the target), is, at this instant, already high enough that the resistivity starts decreasing, getting closer to Spitzer conditions. Therefore the spatial distribution of the resistivity in Al appears as a "wave", determined by the plasma temperature gradient, as the temperature increases from the room temperature close to the Fermi temperature, the resistivity increases as well, when the temperature further rises to values far above the Fermi temperature, the resistivity decreases again, producing a wave-like spatial distribution. The resistivity for the Ag layer, despite rising with temperature as well, remains much lower than the surrounding Aluminum one. This will have effects on the induced B field. The other two resistivity map frames, taken respectively at 1250 fs and 2000 fs, follow the behavior

just exposed for the 750 fs frame. The Al electronic temperature further increases deeper in the target determining the extension and broadening of the resistivity wave-like distribution. Close to the injection point the temperature is high enough that the first Al layer, as well as the Ag layer, falls into Spitzer regime, characterized by very low resistivity. Farther away from the injection point, quite large resistivity gradients are produced at the interfaces Al/Ag/Al, remaining the Ag resistivity much lower than the Al case. These resistivity gradients give rise to the well known interface effects, characterized by the generation of an azimuthal B field at the interfaces between different Z materials. In our case, as we will see, this doesn't produce strong B-fields being the fast electron current density quite low at the point where the gradient reaches its maximum absolute value. Since the plasma resistivity is, in the solid case, determined by the electron plasma temperature, we focus our attention now on the temperature maps correspondent to the resistivity plots in **??**. The initial electron plasma temperature is characterized by room temperature for the first three Al/Ag/Al layers , followed by a temperature of $\sim$ 2 eV for the Sn and Ag layers, related to the LP pulse generated shock 1.9 ns before with the SP focusing on the front surface. The temperature as well as the density of Carbon was, as we already reported, fixed at the beginning of the simulation to be 2 eV for all cases. The injected fast electron beam produces the heating of the target sample. The temperature decreases almost exponentially from the injection point to deep inside the target (note that we adopted a logarithmic color scale).A temperature gradient is observed at the Ag/Al interface, 10μm deep in the target, characterized by a decrease in temperature between the two layers. This effect has not to be attributed to higher ohmic heating in the Ag layer, being its resistivity lower than the surrounding Al layers, as consequence of a much higher plasma electron density (see figure **??**). It is, indeed, due to the combination of higher collisional stopping power and low (initial) specific heat compared to Al. Both phenomena contribute to the high ionization degree for Ag. This can be observed in the plasma electron density plots in figure **??**. The rapidly increasing plasma electron density in the Ag layer has to be attributed to the combination of lower binding energy for electrons in

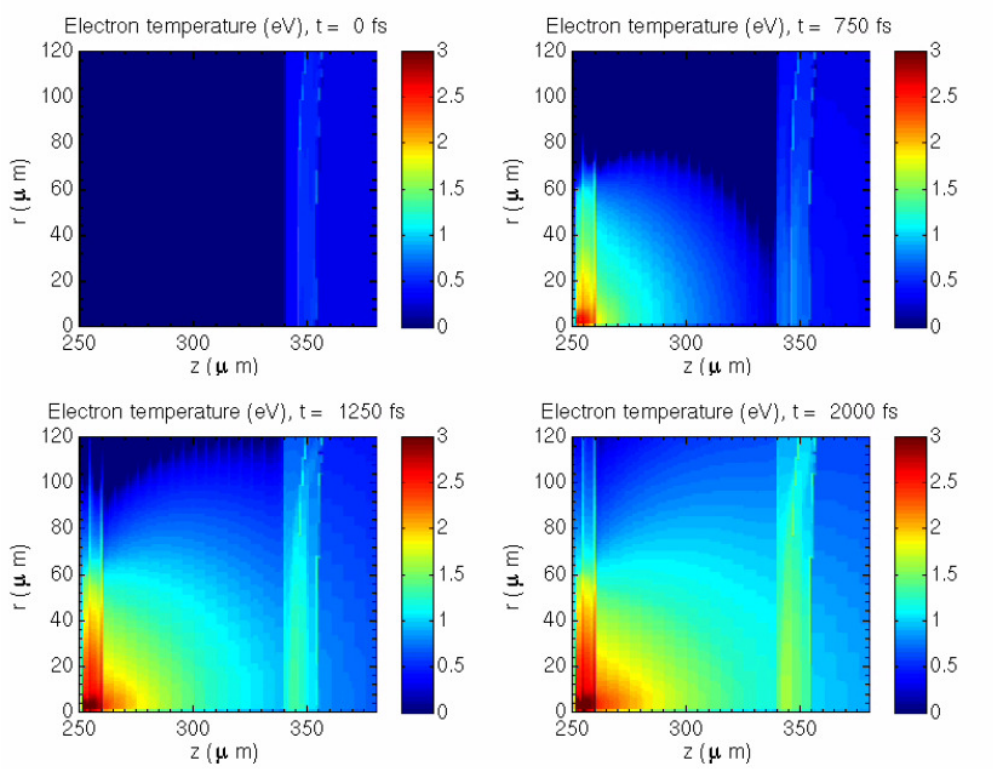

Figure 4.16: **Electron plasma temperature growth versus time.**

the outer atomic shells as well as to a much higher collisional stopping power of the fast electrons in the high Z layer and to a lower specific heat compared to Al.

It is possible to associate the evolution of the Al resistivity spatial distribution to the background electron temperature if we notice that the peak in the Al resistivity corresponds to the region where the plasma temperature is close to 10 eV. For lower as well as for higher temperatures, the Al resistivity reduces.

From the plasma electron density maps (see figure **??**.) it is possible to better understand the behavior of the plasma resistivity discussed previously. Initially, the plasma electron density is obviously very low for the Al and Ag layers, at room temperature, and only the shocked Sn and Cu layers present

a significant electron plasma density. Despite the Carbon initial temperature is set to 2 eV, its lower density compared to the C solid density and the low Z of Carbon result in a very low plasma electron density. This explains why, in these simulations, the resistivity for the C layer is always very high.
At 750 fs simulation time, when the fast electron current density becomes important, the electron plasma density rapidly increases in the Ag layer compared to the Al layers. As we already discussed above, the lower binding energy for outer Ag atomic electrons, the low specific heat and the higher collisional stopping power for fast electrons are all factors contributing to the high ionization degree. This finally results in a low plasma resistivity compared to the surrounding Al, as we already observed discussing the simulation results displayed in figure **??**. At later times, the plasma electron density further increases for the Al and Ag layers, reaching its maximum close to the fast electron injection position, where the plasma is fully in Spitzer regime. We can concentrate now our attention on the fast electrons generated magnetic field in the target, which time evolution of the azimuthal component B_θ is resumed in figure **??**. The magnitude of the magnetic field becomes important for high current densities, corresponding to simulation time $\geq$ 750 fs. The resistive B field develops from the injection region at early times, due to the overall high current density. Around the peak of the injection, when the current density reaches its maximum, a relatively strong ($|B_\theta| \sim 1$ MG) resistive B field develops up to 50μm inside the target, while close to the injection region it reaches values as high as $\sim$ 10 MG. It is interesting to observe that the resistive B field is reduced inside the Ag layer, as consequence of the lower resistivity compared to the surrounding Al material. It is also possible to observe the development of interface fields at the Al/Ag/Al interface due to the resistivity gradients between the two layers. For simulation time $\geq$ 1000 fs, is possible to observe the development of a relatively weak collimating (negative) B field at the interface Al/Sn, and a decollimating (positive) B field on the shock front, inside the Sn layer. This is due to the resistivity gradient related to the density gradient at the shock front. The fast electron current crossing the resistivity drop at higher plasma density, induce a magnetic field that tends to force the electrons in the higher

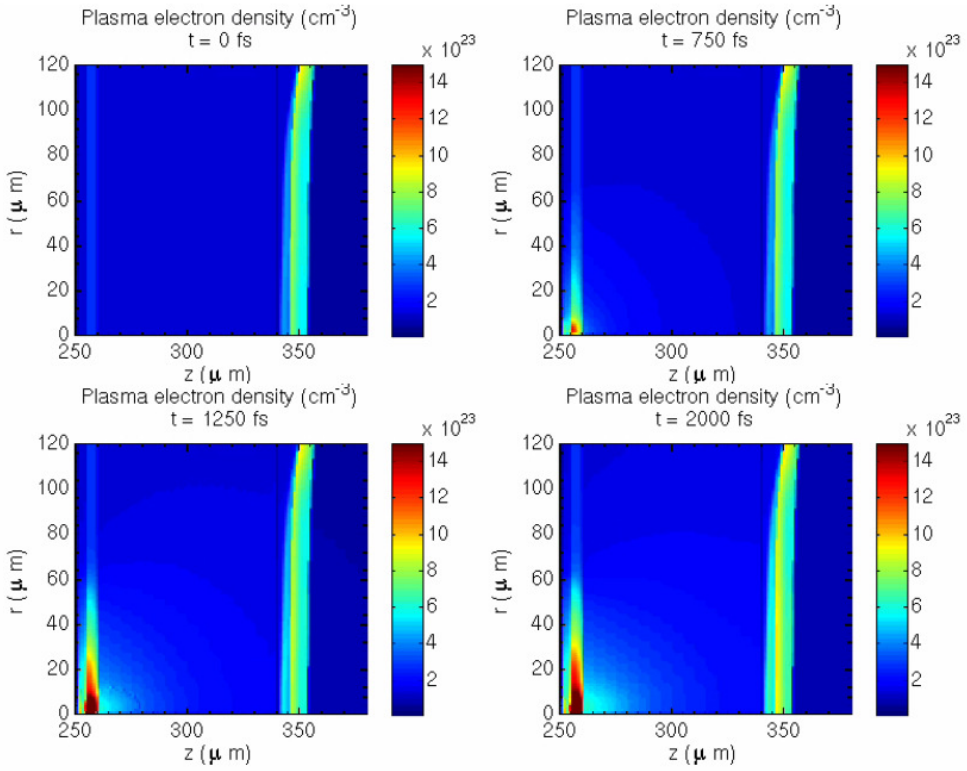

Figure 4.17: **Evolution of the plasma electron density versus time.**

resistivity region, before the shock front. This concept is described in the simple model developed in section **??**. The strong positive B field on the axis at $R = 0$ is a numerical effect, which doesn't strongly affect the simulation, since its action on the fast electrons is to reflect them at the axis, which is what a cylindrical geometry simulation does, therefore the presence of this numerical B field is not detrimental for the simulation.

A strong positive B field also develops on the target front surface, related to the fast electron refluxing and streaming along the front surface. The effect of this field is to reflect the electrons back in the target. The presence of a pre-formed plasma may reduce this field effect, which in any case, affects the simulation only for the very first microns from the front surface and has no effect on the fast electron transport inside the target material.

We can finally discuss the fast electron density data. One important remark

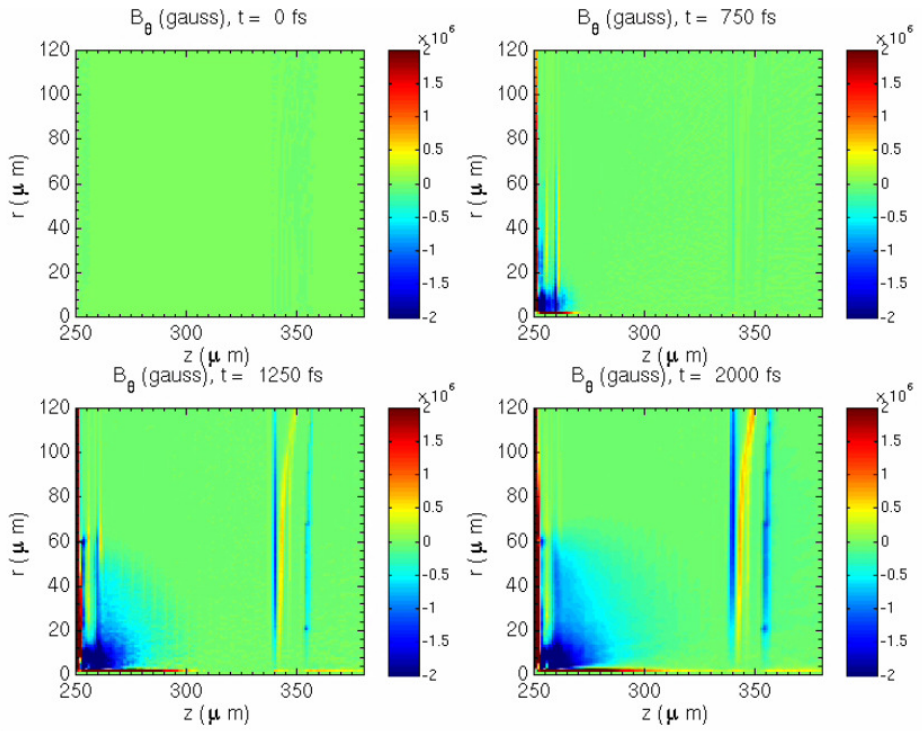

Figure 4.18: B_θ **component growth versus time. The resistive field is generated by the fast electron current.**

is that these data are not energy resolved, therefore all fast electrons are displayed regardless of their energy, implying that at late simulation time, the fast electron density includes also the hot electrons that have actually been stopped (mostly by collisional processes). The simulation results for fast electron density are displayed in figure **??**. As we can observe from the simulation results, there is no evidence of strong field effects at the Al/Ag/Al interfaces. The fast electron density increases with time as they propagate in the target. At later times, the fast electron density decreases again and is possible to distinguish the fraction of fast electrons that have been stopped in the simulation (2 ps frame). The fast electrons are mostly stopped in the high Z and high density regions of the target.

The integrated $K\alpha$ yield, as well as the $K\alpha$ spot size are obtained from post processing of the simulation data. The results for $K\alpha$ emission will

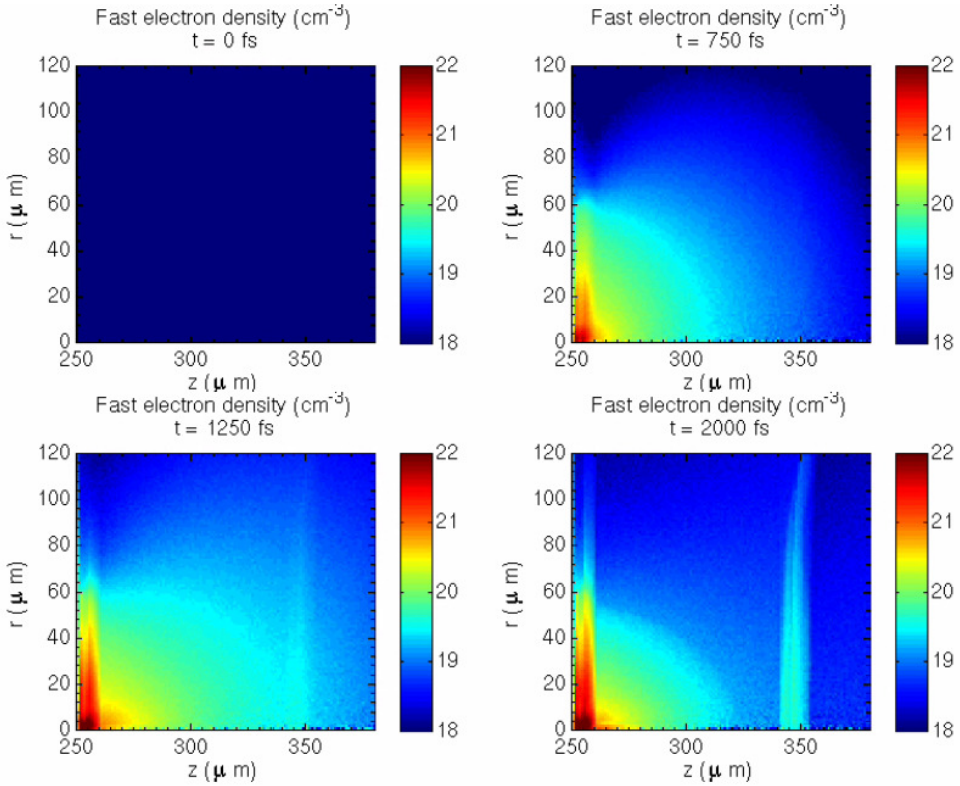

Figure 4.19: **Simulation results for fast electron density versus time. The fast electron density at late times, as in the 2000 fs frame, displays mostly fast electrons that have been lost all their energy by collisions, showing higher density in correspondence to high Z material layers and compressed material (mostly on the shock front).**

be exposed at the end of this section, the description of the simulation for the compressed sample. Once described in detail the various aspects of the simulation for solid Al sample, we can analyze the data for the compressed target simulation with more confidence.

Simulation of the compressed sample target

The simulation results for the compressed case are presented in this section. As for the solid case, we begin our discussion treating the LMD calculated

resistivity at different simulation times, represented in figure **??**. The first

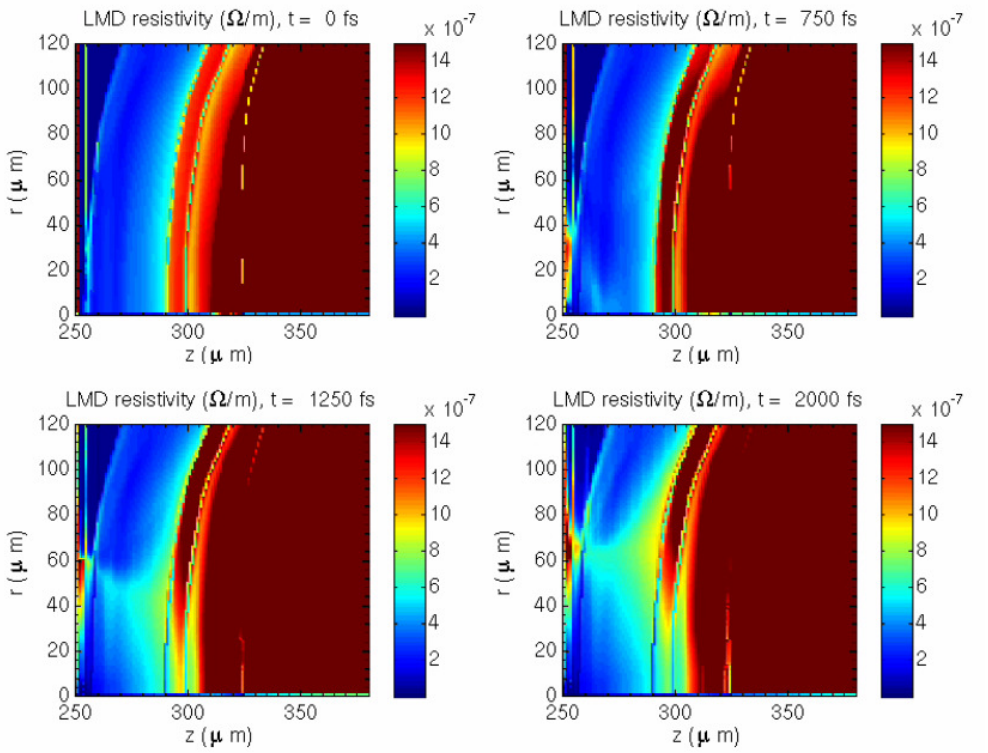

Figure 4.20: **LMD calculated resistivity for compressed target sample. The high resistivity for Sn and Cu layers is due to their hydrodynamic expansion after compression. The initial resistivity of compressed Al is higher than the resistivity for solid on the front surface due to the higher electron temperature.**

considerations on the initial condition of resistivity for the compressed sample are related to the Al transport layer, which resistivity is higher than the solid Al front layer. This is due to the higher electron temperature in the shocked layer. The shock front reached the Ag layer in proximity of the injection point. The very high resistivity for the Sn and Cu layer is due to their hydrodynamic expansion as consequence of the rarefaction wave propagation after compression, reducing their density and therefore their capability to sustain a current. During the fast electron injection, the resistivity close to

the injection point immediately drops as expected due to the high plasma temperature. At the same time the resistivity in the compressed Al layer rises, but up to a much lower value compared to the solid case. This is in very good agreement with the model in section **??**. The higher density of the Al transport layer reduces its resistivity compared to solid Al for an equal plasma temperature. The resistivity of Sn and Cu reduces due to further ionization and heating by fast electrons.
The effect we were interested in, is the evolution of the resistivity gradient at the shock front. It is possible to observe the presence of a rather sharp gradient at the interface Al/Ag, moving away from the injection region as the plasma temperature rises. The amplitude of this gradient, associated with the relatively low fast electron divergence as result of the type of injection adopted, is not sufficient to generate a strong enough magnetic field that could actually affect the fast electron divergence at the shock front. It gives rise, nevertheless, to a stronger B field compared to the solid case, demonstrating that the field is not only due to Al/Ag interface effects, but it is actually sensitive to the presence of the shock front in the Ag layer. Moreover, the hydro profiles adopted in the simulation are actually locally 1D at the injection point: the fast electron beam doesn't actually deal with 2-dimensional gradients unless radially very far away from the injection, where the fast electron current density is very low and therefore unable to generate strong collective effects. The magnetic field evolution represented in figure **??** reflects the considerations expressed above. We can also notice that the overall resistive magnetic field amplitude in the shocked Al is lower than in the solid case, as result of the lower peak resistivity at higher densities. Small amplitude magnetic fields develop at later times at the interfaces of the Al/Sn and Sn/Cu layers as result of the resistivity gradients observable in figure **??**. As expected from the above considerations, the fast electron transport, represented in figure **??** doesn't appear to be sensibly affected by the presence of a bi-dimensional hydro profile. Indeed the overall behavior is very similar to the uncompressed case.

The fast electron divergence as measured from the post processing of

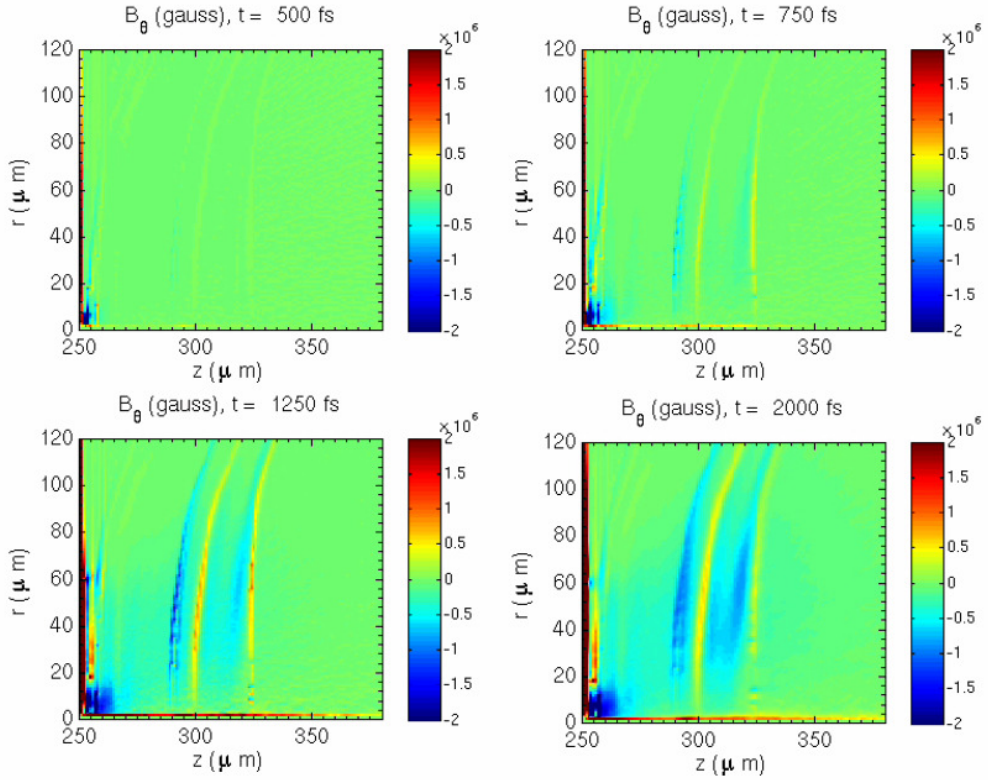

Figure 4.21: B_θ **component generated by the fast electron beam transport in the target. Differently from the results in figure ??, a stronger positive** B_θ **component develops at the shock front located close to the interface Al/Ag. This magnetic field amplitude and spatial extension is not sufficient to affect the fast electron divergence.**

the $K\alpha$ data collected in the simulation, has a reversed trend compared to the experimental results. The $K\alpha$ spot size in the compressed case results smaller than in the solid sample case. This is due to the similar fast electron divergence, in presence of a Cu tracer layer much closer to the fast electron source compared to the solid case, leading to a smaller $K\alpha$ spot size. The Cu-$K\alpha$ spot size lineouts are represented in figure **??**, and the results for the analysis of the $K\alpha$ yields are represented in table **??**. The Cu-$K\alpha$ spots are interpolated in order to reproduce the $K\alpha$ imager response with resolution

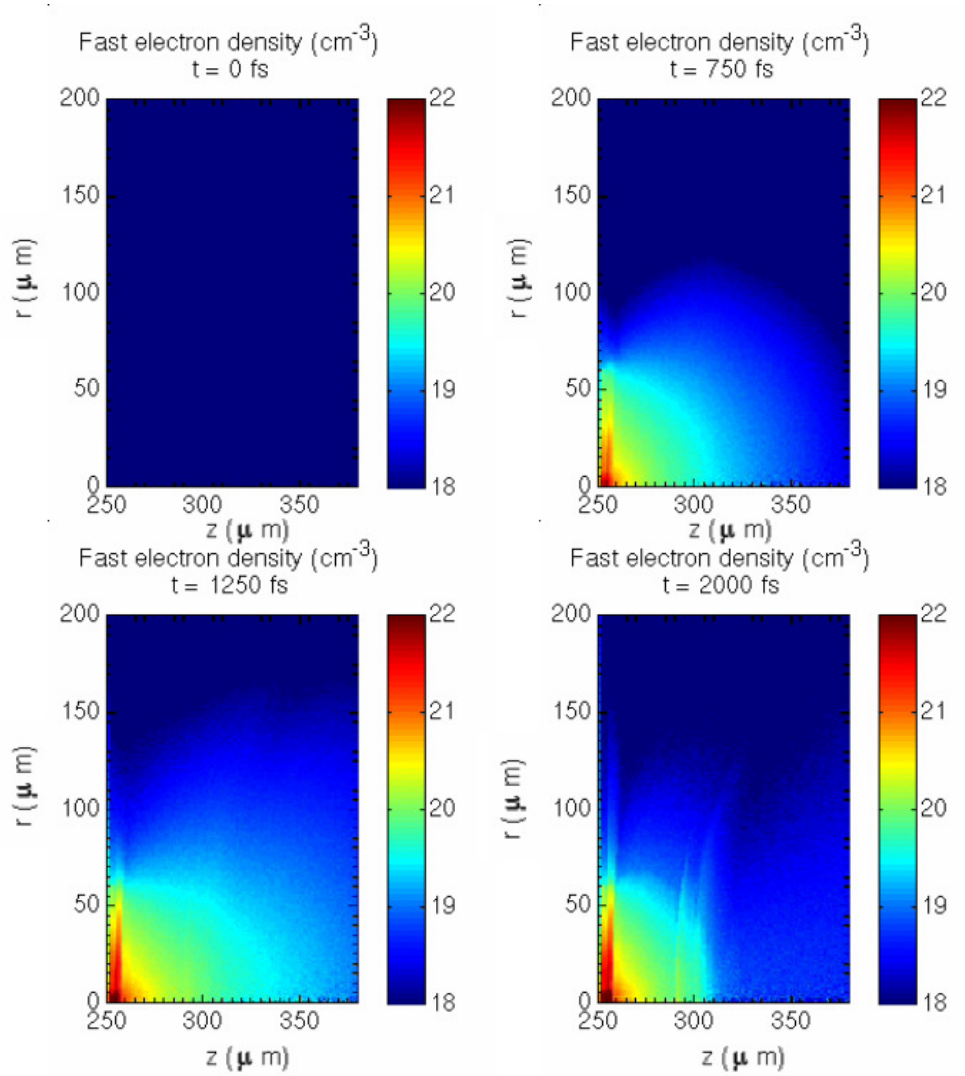

Figure 4.22: **Fast electron density maps for the compressed sample case. There is no clear evidence of any difference in transport compared to the solid Al sample case.**

of 20μm.

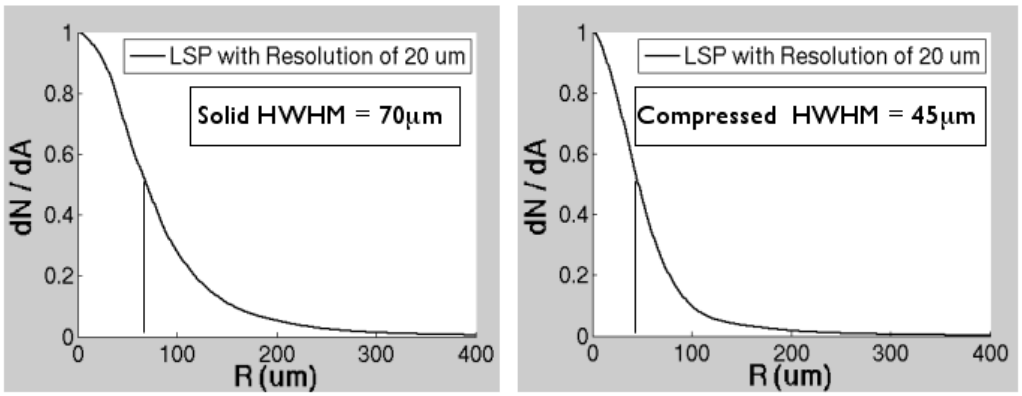

Figure 4.23: **Cu-$K\alpha$ spot sizes obtained from the simulations and interpolated in order to replicate the $K\alpha$ imager response with resolution of 20μm. The peak value is normalized to 1.**

Table 4.1: X-ray analysis results

Target	Cu-$K\alpha$/Ag-$K\alpha$	Cu-$K\alpha$ spot size(μm)	Sn-$K\alpha$/Ag-$K\alpha$
Solid	2.94	70	0.51
Compressed	4	45	0.69

4.3.4 Conclusions on the simulations for the JLF experiment

The simulations for the 80μm Al transport layer target didn't provide the answer to our main question about the large measured fast electron divergence.
Several could be the reasons for this large difference between experimental and simulation data:

1. The shock broke out from the front layer before the SP was focused, changing the LPI. This represents a possibility since shock breakout data from SOP weren't collected.

2. The Titan source we adopted for the simulation is not correspondent to the real fast electron beam distribution in our experimental conditions. The Titan distribution was built using EPM data from 2010

and conditions may have changed. Moreover the distribution is the result of a transformation from 2D cartesian from LPI simulations to 2D cylindrical coordinates which is subject to a rather large uncertainty.

3. A possible mis-alignment between the SP and LP beam might have made the fast electron beam interact with the edge of the shock, instead of being collinear.

4.3.5 Spherical shock

In order to verify wether it is possible to observe any fast electron decollimation due to resistivity gradients using the Titan injection adopted in the previous simulations, and, at the same time, in order to verify wether the hydrodynamic profiles adopted were correct, we performed a simulation using a simplified spherical shock hydrodynamic profile (corresponding to an extremely small LP spot size). The hydrodynamic profile was built artificially, using a sixth order super-Gaussian profile to simulate the density and the temperature increase as across a shock front, followed by an exponential density and temperature decrease after the shock front. The simulated target was a multi-layer, constituted by 80μm Al, 10μm Cu and 400μm C as get lost layer. The radius of the shock was chosen as 80μm, starting from the Cu layer. The distance between the target front surface and the shock front was therefore 10μm. The total areal density is for the Al and Cu layer is conserved in the shock-compression. A schematic of the target is represented in figure **??**. The temperature ranges from room temperature, 0.03 eV, up to 3.1 eV at the shock front, and a 4$\times$ Al solid density was chosen as shock peak compression. The Titan source exposed in the section above was used, and the simulation run for about 2 ps, showing the evolution of the resistivity gradient related magnetic field, as well as the fast electron guiding on the shock front. The simulation results are summarized in figure **??**. A sharp resistivity gradient at the interface solid-compressed Al gives rise to a ~ 3.5 MG de-collimating magnetic field. The action of the resistive magnetic field at the front coupled with the de-collimating field at the shock acts as a guide for fast electron in the relatively low energy part of the spectrum ($\leq$ 500

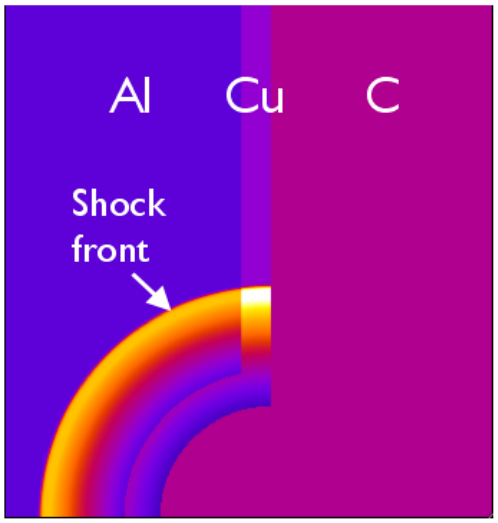

Figure 4.24: **Density profile for the spherical shock simplified simulation.**

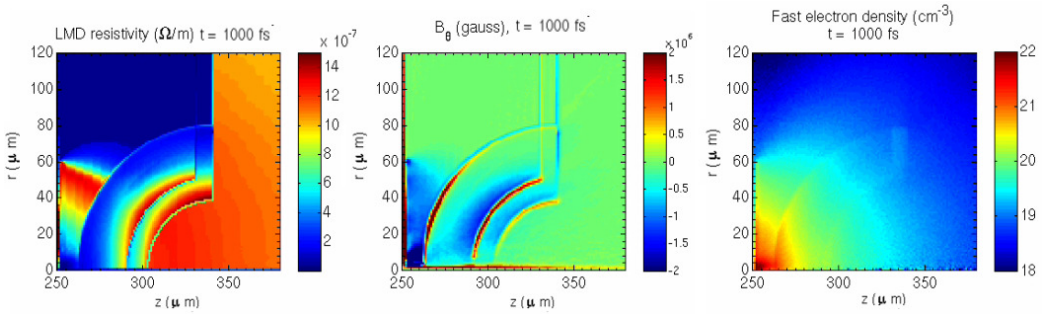

Figure 4.25: **Simulation results at 1 ps simulation time for simplified spherical shock-compressed target. A sharp resistivity gradient between solid and compressed Al generates a ~ 3.5 MG de-collimating magnetic field. A small fraction of fast electron is being deflected.**

keV). A similar field structure is observed at the interface Al/Cu and Cu/C. The negative B_θ field in the shocked region is due to reversed resistivity gradient between the layers. Despite its lower amplitude, the spatial extension is large enough to produce a collimation of the electrons propagating in between the layers. In figure **??** are represented the trajectories of 500 keV mono-energetic electrons, generated with uniform angular distribution

(not isotropic), in the magnetic field structure obtained from the simulation (collisions are neglected). The trajectories are calculated using the particle pusher adopted by Zuma hybrid code.

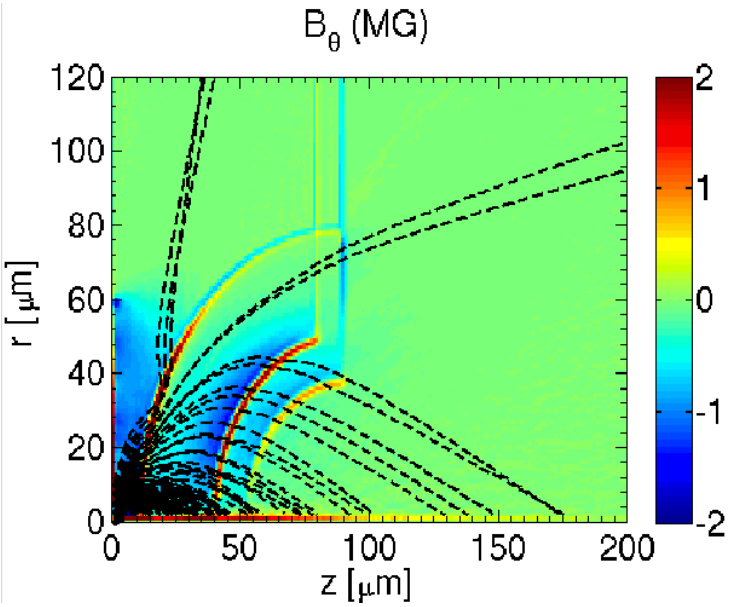

Figure 4.26: **Trajectories for 500 keV mono-energetic electrons in the magnetif field structure obtained from spherical-shock compression simulation. Electrons with the right entering angle are deflected or guided by the magnetic field.**

It is possible to observe that the produced magnetic field can deflect or guide 500 keV electrons entering the field structure with an optimum angle with respect to axis of symmetry of the simulation. The simulated Cu-$K\alpha$ spot represented in figure **??** shows a weak guiding effect of fast electrons by the magnetic field, resulting in a weak lateral spot merged with the classic Gaussian-like spot profile.

Conclusion on simplified spherical shock compression

The simplified 2D compression simulation shows some deflective effect on fast electron transport by the resistivity gradient generated magnetic field. Nevertheless, this effect is not large enough to observe a large de-collimating

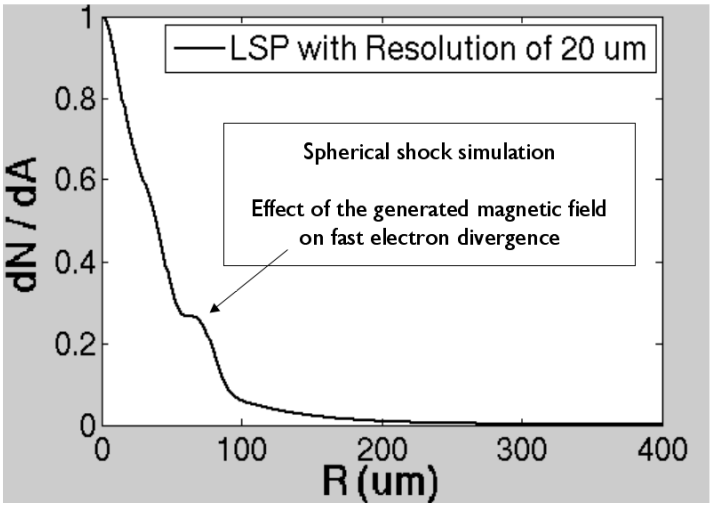

Figure 4.27: **Simulation results at 1 ps simulation time for simplified spherical shock-compressed target. A sharp resistivity gradient between solid and compressed Al generates a ~ 3.5 MG de-collimating magnetic field. A small fraction of fast electron is being deflected.**

effect that would lead to a divergence similar to that one observed in the JLF experiment.
This indeed, rules out any possible doubt about the usage of inappropriate hydro-dynamic profiles. The questions remained open are relative to the usage of an appropriate fast electron source or the possibility of shock breakout before the short pulse focusing on the target front surface.

4.4 Future work on fast electron transport in resistivity gradients.

The study of fast electron transport in resistivity gradients led to the more general problem of fast electron transport in counter-directed resistivity gradients. This is a problem of great interest for Fast Ignition research, since the ignitor beam is expected to travel in a plasma which parameters of density and temperature are rapidly changing from the critical surface up to the isochorically compressed DT fuel.

The idea is to perform a simulation work, which theoretical basis is the model exposed in section **??**, in which a fast electron beam propagates in a planar shocked material (Al), mimicking for example the conditions the ignitor beam will encounter at the cone tip, where a strong shock followed by a plasma jet will be driven inside the cone by the implosion of the surrounding capsule. The study of possible detrimental effects related to the presence of the shock may be important for Fast Ignition point design. Following the model exposed in **??**, in a planar shock the component of the fast electron current that will generate the magnetic field will be J_R, since J_Z will be collinear with the resisitvity gradient and therefore not producing any magnetic field ($\partial_r \eta = 0$). Therefore our study will be focused on scanning for which parameters of angular distribution and current density, a resistivity gradient related to the presence of a shock could have detrimental effects for the transport of fast electrons in the energy range 1-2 MeV, the range of interest for FI. The generated B_θ component needs to have an amplitude of $\sim$ 10 MG over few (3-4) μm to start affecting the transport of electrons in the FI energy range of interest. The author conducted some preliminary simulations at relatively low current density (10^{12}A/cm^2) at the shock front, adopting a planar shock geometry which properties (compression, temperature, layers) are identical to those of the spherical shock exposed in the previous section. Three simulations have been performed, keeping the same current density and pulse duration and varying the fast electron angular distribution as follows:

1. $\Omega = \sin\theta cos\theta$, with narrow ($\cos\theta$) angular distribution.

2. $\Omega = \sin\theta \exp\left[-(\theta/\Delta\theta)^4\right]$, adopting a super-Gaussian distribution as in reference [**?**].

3. $\Omega = \sin\theta$, isotropic distribution.

The fast electron distribution is a two temperature exponential with $T_1 \approx 1$ MeV and $T_2 \approx 6$ MeV. The target density plot is represented in figure **??**, the temperature profile follows the density profile as in the spherical shock case. The only difference is that the minimum temperature has been chosen to be

1 eV, value not far from reality if we consider a pre-pulse induced heating of the front layer.

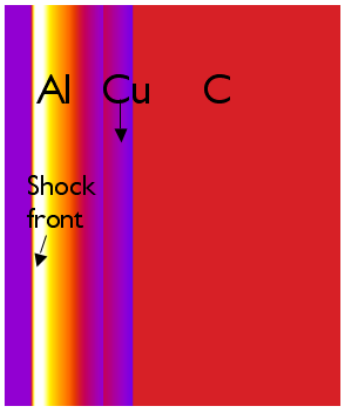

Figure 4.28: **Density profile for the planar shock target design.**

The preliminary results show, as expected from the model, larger positive B_θ component for broader angular distribution, its peak amplitude is ~ 8.5 MG for isotropic distribution, ~ 6 MG for super-Gaussian and ~ 4.5 MG for cosine distribution. We do not re -propose all the maps to avoid redundancy. Figure **??** displays the trajectories for 500 keV electrons, generated with uniform angular distribution, for each of the B field maps at 1 ps simulation time.

It appears clear that the magnetic field amplitude plays an important role on fast electron transport, as for the isotropic distribution generated magnetic field, some of the electrons are reflected at the shock front and many other are widely diffused. An intermediate behavior is found for the electrons in the super-Gaussian angular distribution-generated magnetic field. Finally strong collimation due to the prevalence of the resistive magnetic field is observed is the case of cosine angular distribution-generated magnetic field. We remark again that all the trajectory images are obtained using the same uniform fast electron angular distribution.

Therefore we obtained some promising preliminary results that confirm our model on fast electron transport in counter directed resistivity gradients. Further simulation is required to estimate for which beam parameters the

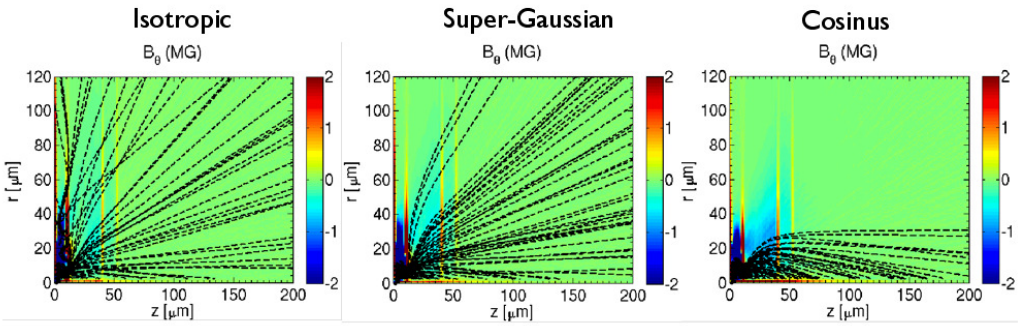

Figure 4.29: **500 keV electrons trajectories in the magnetic field structures produced by isotropic, super-Gaussian and cosine fast electron angular distributions propagating in the same hydrodynamic profile. The 500 keV test electrons are generated with uniform angular distribution.**

magnetic field amplitude becomes detrimental for electron in the FI energy range of interest.

Chapter 5

Improved laser-to-proton conversion efficiency in isolated reduced mass targets

5.1 Introduction

The ion fast ignition is a very promising alternative to fast electron fast ignition. Some of the issues related to fast electron fast ignition, such as the fast electron energy spectrum and fast electron divergence are overcome by proton FI. Indeed, a relatively broad proton energy spectrum, with energy ranging from 3 to 18 MeV is not only acceptable but actually preferable than a mono-energetic spectrum. Indeed protons in this energy range can be treated as classic particles with different time of flight from the source up to the isochorically compressed fuel. The higher energy protons produce a preliminary heating of the DT fuel, causing the reduction of the proton stopping power in DT plasma, being this dependent on the DT plasma temperature. Therefore, in order for the proton beam to release its energy in a small volume of DT, producing the lateral hot spot, the proton energy must reduce during the heating process to attain the energy density conditions in the hot spot necessary to successfully trigger a self-sustained thermonuclear reaction. Some recent works demonstrated [**?**] the focusability of proton

beams by means of shaped foils such as hemispherical targets and the proton induced heating of target samples.
Other possible applications of short pulse laser produced ion beams include proton oncology [**?**] [**?**], beam injection in conventional accelerators [**?**].

A still open problem is represented by the laser-to-proton energy conversion efficiency, which is still very low ($\sim 1\%$) compared to the laser-to-hot electron energy conversion efficiency.
In this work, entirely conducted by the author solely, is presented an experimental study on the dependence of the laser to proton energy conversion efficiency from the target isolation, using reduced mass targets (RMT).
The idea is to use a thin reduced mass target (RMT) linked to its support by thin legs, in order to isolate the target as much as possible from the surrounding structure. The large isolation minimizes fast electrons from freely spreading radially and leaking out from the proton acceleration foil, forcing them to reflux and lose their energy into the RMT. This has the effect of keeping the space charge fields for longer and thus accelerating protons more efficiently.

5.2 Experimental setup

The experiment was performed using the T-Cubed at the Center for Ultrafast Optical Science (CUOS), University of Michigan, Ann Arbor. The Nd:glass laser, with central wavelength at 1053 nm, delivered 5 J of laser energy in 400 fs and was tightly focused onto the target front surface with 20μm focal spot size resulting in a average intensity of 3×10^{18} W/cm^2.

As shown in figure **??** , a laser-cut RMT (150μm square,10μm thick) was only attached to a 10μm thick surrounding Cu foil by means of 4 legs of variable size (21, 42 and 84μm) for each target and 106μm length. Smaller leg size corresponds to a higher RMT isolation. In addition, large (3mm x 3mm) uniform, 10μm thick Cu foil targets were also used as comparison. Figure **??** shows a microscope picture of the RMT targets.

A stack of Radio-chromic film (RCF), Gafchromic HD-810 was used as a

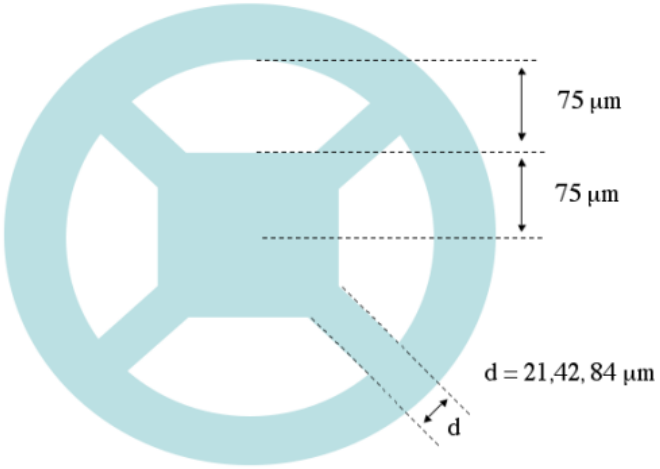

Figure 5.1: **Schematic of the reduced mass target adopted in the experience.**

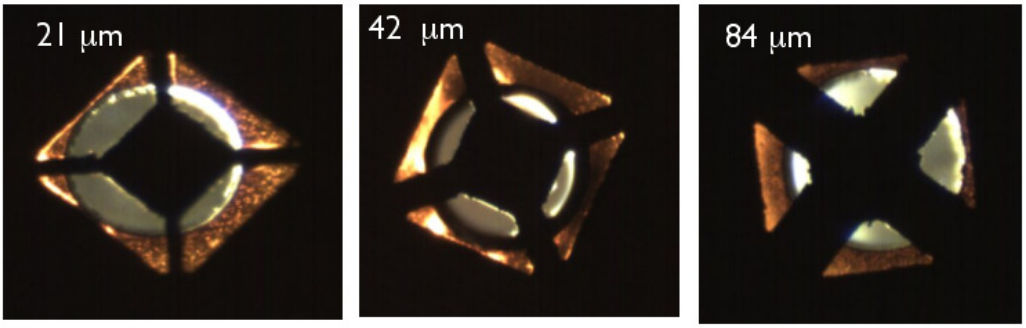

Figure 5.2: **Microscope picture of reduced mass targets. From left to right, respectively 21, 42 and** 84μ**m leg size targets.**

proton beam diagnostic. The RCF stack was positioned 4 cm from the target rear and protected with 12.5μm Al foil, allowing protons with energies equal or higher than 1.05 MeV to deposit energy in the first RCF foil active layer.

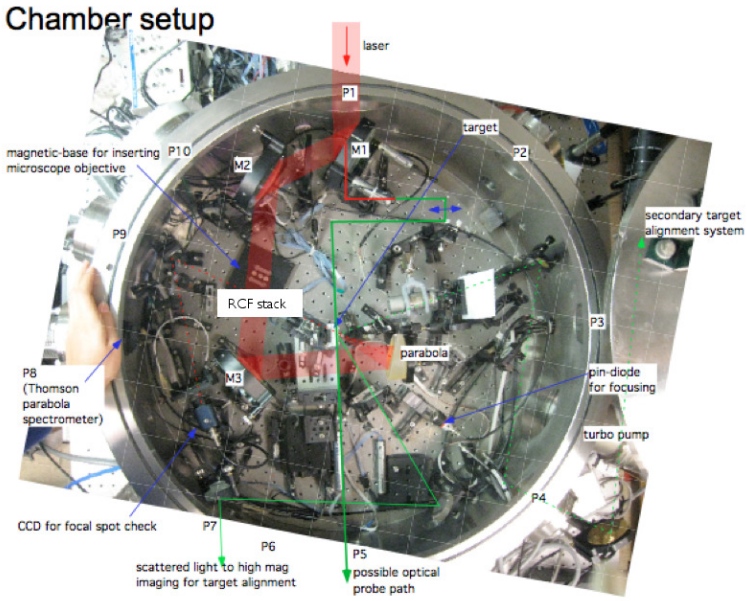

Figure 5.3: **Overview of the Tcubed laser interaction chamber.**

5.3 Experimental results

The RCF images were digitalized with a calibrated scanner and the total dose was then evaluated in krads, adopting calibration curves and relative dose errors as in reference [**?**]. The dose deposited on the first RCF, corresponding to protons with energy above 1.05 MeV, is strongly dependent on the leg size, showing higher dose as the leg size decreases. The dose released on the second RCF, corresponding to protons with energy above 3.1 MeV, is over an order of magnitude lower than that one deposited in the first RCF, due to the rapid decay of the proton number with increasing energy. In this case, no clear relation is found between target leg size and integrated dose on the RCF. Example of the collected RCF data is given in figure **??** and the experimental results are displayed in figure **??**.

Varying the tab size increases or decreases the solid angle in which the fast electrons can freely spread out from the focal spot region. This constitutes a geometrical constraint for the fast electron propagation, confining them into the RMT by space charge fields. To a smaller tab size corresponds a smaller

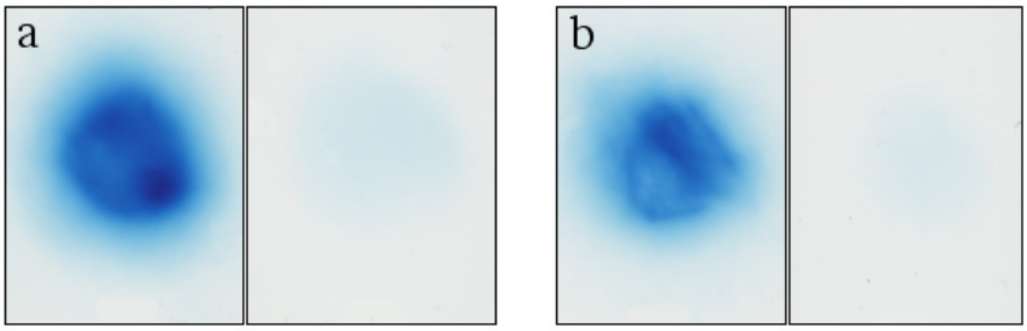

Figure 5.4: **Collected RCF data for (a) 21μm tab width and (b) 84μm tab width. The 21μm tab width 1^{st} RCF data shows higher density (dose) compared to the 84μm one. In both cases the dose on the 2^{nd} RCF results very low.**

free propagation solid angle, and therefore a higher confinement.

5.4 3D hybrid simulations of proton acceleration from RMT targets

To appropriately model the experimental results, 3D cylindrical hybrid simulations using Lsp hybrid code have been performed. The RMT is represented by a 75μm radius disk connected to the main foil by 4 legs with size of respectively 21 and 84μm. Also the completely isolated RMT and a simple Cu foil are simulated. The main foil is represented by a ring of 350μm external radius and 150μm internal radius, connected to a conductive boundary. The Cu foil thickness is set to 10μm.
A fully ionized H contaminant layer is coated to both front and rear target surface.
A 3D rendering of the simulated targets is represented in **??** To allow for a reasonable simulation wall time, the maximum grid resolution along the z-axis (normal to the target), is set to 250 nm; the time step is then limited by the electromagnetic Courant condition, given by the ratio of the cell size Δx and the speed of light in vacuum c: $\Delta t = \Delta x/c$. To guarantee enough parti-

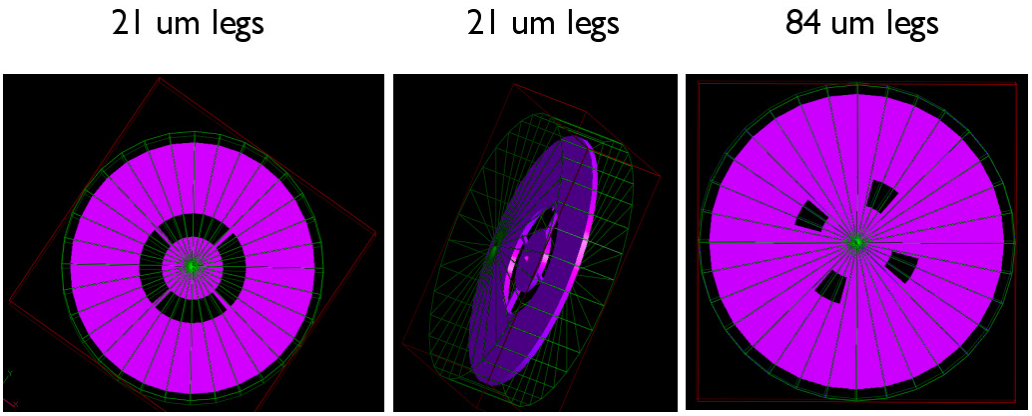

Figure 5.5: **3D rendering of 21 and 84μm leg size simulated RMTs.**

cle statistics, the proton contaminant layer is 8 cells thick, corresponding to 2μm total thickness. However this is unrealistic, being the real contaminant layer thickness of few tens of nanometer. To obtain realistic results, the density of the contaminant layer has been reduced to $n_H = n_e = 3.35 \times 10^{20}\text{cm}^{-3}$ in order to conserve the total contaminant mass. The initial temperature of the Cu foil is set to $T_i = T_e = 5$ eV with a fixed charge Cu^{4+} and a density of $n_{Cu} = 8.5 \times 10^{22}\text{cm}^{-3}$. To guarantee charge neutrality, the corresponding electron density was set to $n_e = 3.4 \times 10^{23}\text{cm}^{-3}$. An exponential fast electron distribution, with slope temperature of 1.1 MeV and total energy of 1.46 J is injected. The spatial distribution is Gaussian with 10μm FWHM and a 45° full angle angular distribution has been adopted. The simulations are terminated when the fast electrons release the 99% of their kinetic energy into the system. In figure**??** are represented 3D particle images of proton acceleration 1.5 ps after laser irradiation.

In order to explain the effect of leg width on conversion efficiency and spectra we need to understand the fast electron dynamics and the resulting sheath fields in various target isolation configurations. We have studied the fast electron density n_{e-fast} and the electric field component normal to the target surface at different simulation times. The axial lineouts of n_e and E_z are axial obtained averaging over the whole RMT surface. At the peak of the injection (800 fs) the electric field reaches its maximum averaged amplitude

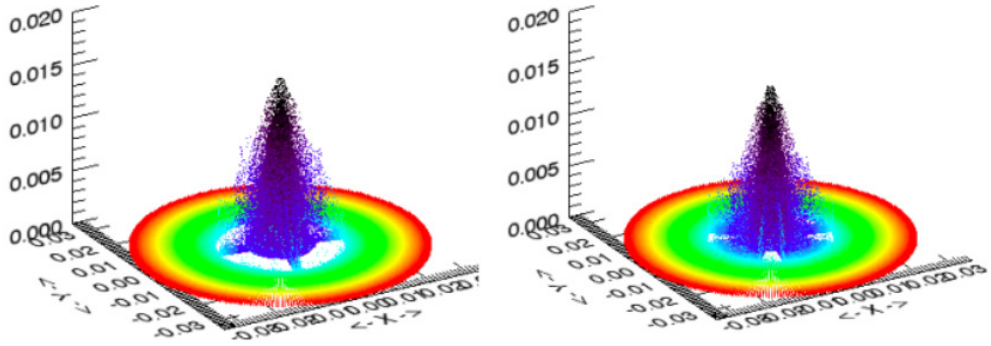

Figure 5.6: **Particle image from simulation of proton acceleration from 21 and** 84μ**m leg size. The macro-particles are colored according to their charge. The image is taken at** 1.5 **ps simulation time.**

($\sim$ 280 kV/μ)m. At this time the fast electron density measured from the target surface appears to be almost identical for all target configurations, as shown in figure **??** (left). As a consequence, the amplitude of E_z doesnt vary significantly (see **??** (right)).

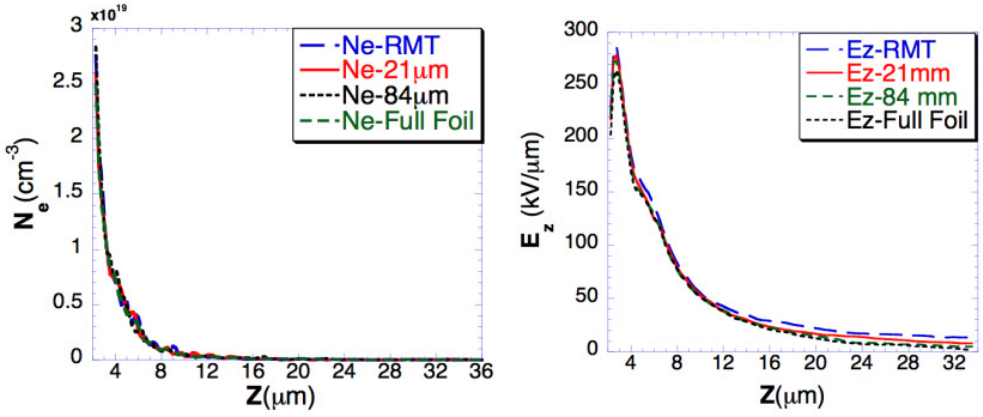

Figure 5.7: **Fast electron density (left) and corresponding** E_z **component (right) at the peak of the injection and averaged over the RMT surface, as function of distance from the target surface.**

Protons composing the high energy tail of the energy distribution are

accelerated at this stage. This explains the uniform proton signal obtained for protons with energies equal or above 3.1 MeV. However, at later times the differences between the various targets start to become more evident. Shortly after the end of the injection stage the (radially averaged) fast electron density is larger for more isolated targets, as represented in figure **??**. In fact, for these highly isolated targets the fast electrons are better confined on the RMT, leading to larger charge density and consequently larger E_z. In poorly isolated targets instead, the fast electrons can spread radially more easily, and the overall charge density is reduced, as well as the amplitude of E_z.

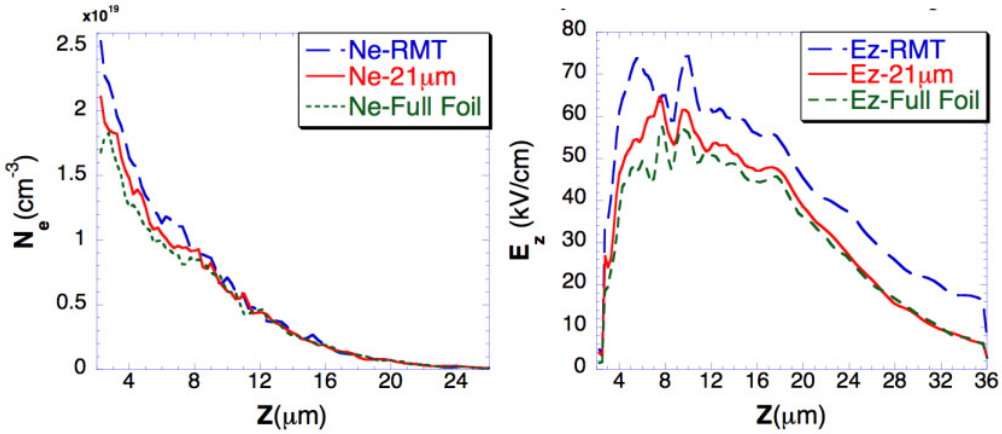

Figure 5.8: **Fast electron density (left) and E_z component (right),** 0.5 **ps after the end of the injection stage, and averaged over the RMT surface, as a function of the distance from the target surface. At this time it is already possible to observe the dependence of proton acceleration on target isolation.**

The slower electric field decay for isolated targets allows to accelerate protons more efficiently at later times, with clear differences in the proton spectra, represented in figure **??**.

The simulated spectra of figure **??** are representative of the energy distribution gained by the protons at the end of their acceleration stage. From these data it is possible to obtain the integrated doses deposited into the RCFs. The calculation is made accounting for the Bragg curve in the RCF

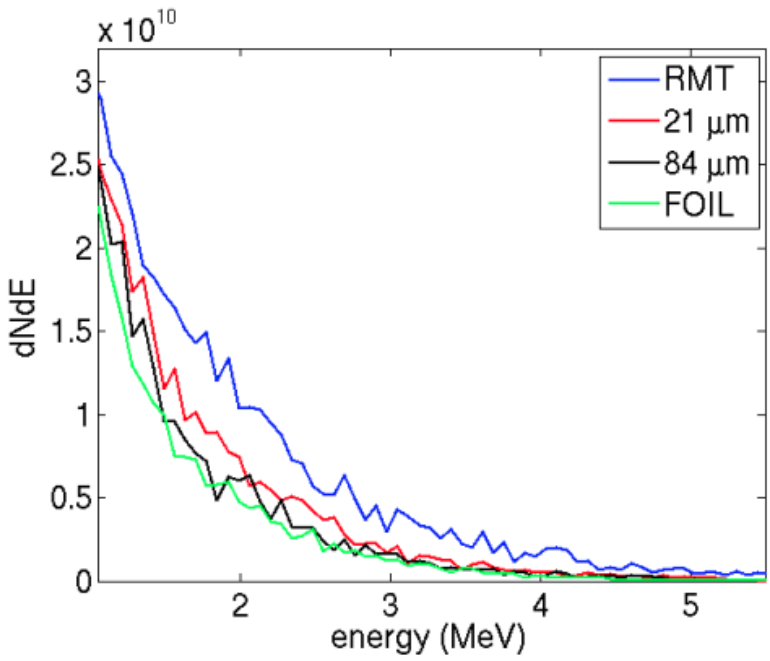

Figure 5.9: **Proton spectra for the four targets, taken at the end of the simulation, when the fast electrons released the** 99% **of their energy in the system.**

relative to the specific proton energy.

In figure **??**, the quantitative comparison between experiment and simulations is shown. We assumed a laser-to-fast-electron conversion efficiency of 30% to calculate the simulated, energy-normalized deposited dose. This is consistent with experimentally inferred values [**?**]. For the first RCF, sensitive to proton energies above 1.05 MeV, with larger contribution by protons in the 1-2 MeV range (due to the Bragg curve), the simulated trend of normalized dose vs. leg width is in excellent agreement with the experimental data (figure **??** left), implying that the simulated proton energy scales correspondingly to the experimental data in this energy range. The dose deposited in the second RCF was an order of magnitude smaller than in the first one. This feature is captured by the simulations too. However we stress that for this case it is less obvious whether the simulations are in agreement with the experimental data, due to the large experimental uncertainty (figure **??**

right).

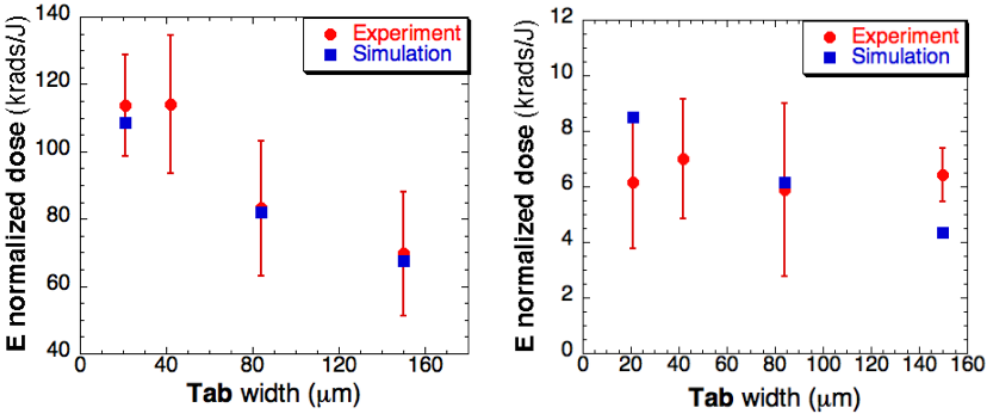

Figure 5.10: **Experimental data and 3D hybrid simulation results for RCF 1 (left) and RCF 2 (right).**

Nonetheless, the results just presented give us confidence about the quality of our simulations. Since the experimental uncertainty in the laser-to-proton conversion efficiency is large, we turn to the simulation data to get an estimate for these quantities. Figure **??** shows the time integrated proton kinetic energy as a function of time; it demonstrates how the laser-to-proton conversion efficiency is highly dependent on the target isolation. We observe that even though the initial acceleration stage is similar for all targets, at around 1.2 ps the curves start to separate. The acceleration saturates earlier for poorly isolated targets; conversely, the higher the isolation, the longer is the acceleration of the protons and hence the higher is the laser-to-proton conversion efficiency. The calculated laser-to proton conversion efficiencies for the 21?m tab, 84 ?m tab and full-foil cases are respectively the 3, 2.5 and 2.14%, corresponding to an efficiency increment of about 50% for highly isolated targets, with respect to flat foils.

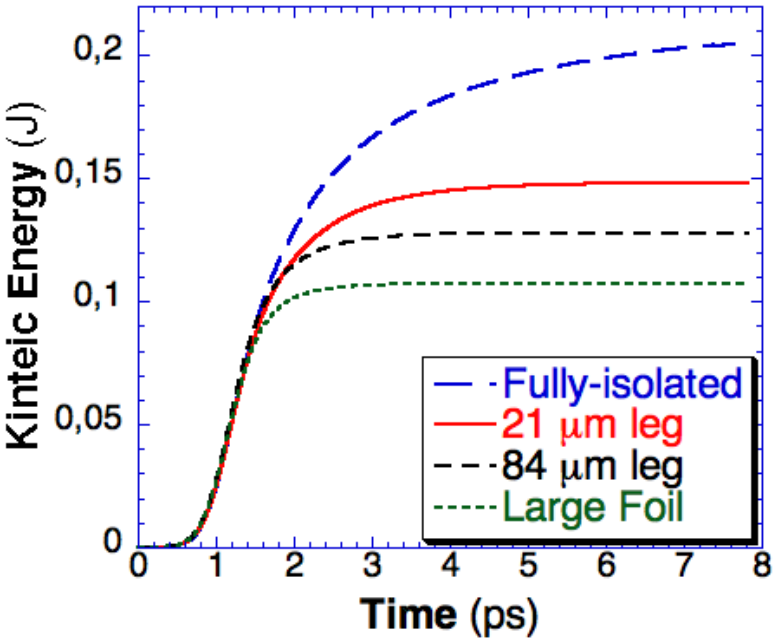

Figure 5.11: **Proton (forward accelerated) total kinetic energy vs. time, for the four different targets described in the text. The proton acceleration is initially identical and starts diversifying at about 1.4 ps simulation time, or 0.4 ps after the injection.**

5.5 Conclusion on laser-to-proton energy conversion efficiency

In this work we have demonstrated that the use of highly isolated, reduced mass target (RMT) foils can significantly improve the laser-to-proton energy conversion efficiency. These RMT foils are attached to an external support by thin legs. The use of thin legs reduces the radial spread of the fast electrons and results in a significant increase of the proton acceleration time. We observe that the smaller the leg size (i.e., the higher the isolation with respect to the supporting structure), the higher is the conversion efficiency. These results are relevant for many applications, including fast ignition where the conversion efficiency into protons will play an important role in determining whether proton-driven fast ignition is a viable scheme to pursue. In this

respect, experiments adopting cone shaped targets and hemispherical RMTs will be performed to prove the principle here demonstrated, for conditions closer to a fast ignition scenario.

Chapter 6

Conclusion and perspective

6.1 Summary of the thesis work

In this thesis work the author presented a small fraction of the experimental experience accumulated during the years of Master and PhD studies. Nevertheless, the two experiences described played an important role in my scientific formation.

The experimental analysis and complex modeling of fast electron transport in warm dense matter have been successfully conducted. For the first time, full scale Lsp hybrid simulation of fast electron transport in multilayer targets with density and temperature gradients and the usage of EOS for each material, have been conducted. A simple model of fast electron transport in counter-directed resistivity gradients have been developed. The model is general and applies to all configurations in which a fast electron beam propagates along an axis on which the plasma parameters are rapidly changing, and relates the collective effects of magnetic field generation to the intrinsic fast electron divergence. This has important implications for FI since the plasma conditions from the critical surface to the compressed DT fuel core are rapidly changing, leading to resistivity gradients along the ignitor beam path that could affect the fast electron beam divergence with important implications for the determination of the parameters for Fast Ignition point design. In the specific work presented in the thesis the counter-directed re-

sistivity gradients were associated to density gradients in Aluminum plasmas. A novel target design for ion acceleration has been presented. Experimental data demonstrated that a 50% improvement in laser-to-proton energy conversion efficiency is achievable with highly isolated RMTs. 3D cylindrical hybrid simulations have been performed, showing *quantitatively*striking agreement with the experimental data and allowing to estimate the exact values of the conversion efficiency achieved in the experiment.
The proposed target design is suitable for application in FI research as well as for the generation of proton sources for cancer therapy and particle acceleration application, being suitable for mass production and high repetition rate operation.

6.2 Future work

The author will further research the physics of fast electron transport in resistivity gradient. The future work will be focused on the determination of the beam parameters, such as current density and angular distribution, for which the propagation in a sharp, counter directed resistivity gradient will be detrimental for fast ignition, affecting the transport of electron in the 1-2 MeV energy range.
The next step in proton FI research will be coupling the highly isolated RMTs, designed with hemispherical shape, to a cone target, and conduct proton focusing experiments, in order to verify if the usage of RMTs will affect the focusing of the proton beam due to edge field effects. At the same time this will allow to verify the contribution of the electric field developed on the cone wall to the focusing of the proton beam.

Bibliography

[1] John Lindl, *Development of the indirectdrive approach to inertial confinement fusion and the target physics basis for ignition and gain*, Phys. Plasmas 2, 3933 (1995).

[2] S. Atzeni and J. Meyer-Ter-Vehn, *The Physics of Inertial Fusion*, Oxford Science publications.

[3] J. Lindl,*Development of the indirect-drive approach to inertial confinement fusion and the target physics basis for ignition and gain*, Physics of Plasmas 2,11 (1995)

[4] M. Tabak, J. Hammer, M. Glinsky, W. Kruer, S. Wilks, J. Woodworth, E. Campbell, M. Perry, and R. Mason textitIgnition and high gain with ultra- powerful lasers.Phys. Plasmas, 1, 5, 1626, (1994)

[5] M. Roth, T. Cowan, M. Key, S. Hatchett, C. Brown, W. Fountain, J. Johnson, D. Pennington, R. Snavely, and S. Wilks *Fast ignition by intense laser- accelerated proton beams*, Phys. Rev. Lett., 86, 3, 436439, (2001).

[6] R. Kodama, P. Norreys, K. Mima, A. Dangor, R. Evans, H. Fujita, Y. Kita- gawa, K. Krushelnick, T. Miyakoshi, and N. Miyanaga, *Fast heating of ultrahigh-density plasma as a step towards laser fusion ignition*, Nature, 412, 6849, 798, (2001)

[7] S. Atzeni and M. Tabak, textitOverview of ignition conditions and gain curves for the fast ignitor,Plasma Phys. Control. Fusion 47, (2005) B769-B776.

[8] P. Gibbon, *Short Pulse Laser Interaction with Matter*, Imperial College press.

[9] S. C. Wilks, W. L. Kruer, M. Tabak, and A. B. Langdon,*Absorption of Ultra-Intense Laser Pulses*, Physical Review Letters, 69, 9, 1383 (1992).

[10] J.Koch et al Phys. Rev. E, 65, 016410 (2001).

[11] Pisani et al. Phys. Rev. E, 62, R5927 (2000).

[12] Beg et al.Phys. Plasmas, 4, 447 (1997).

[13] M. Key

[14] L.D. Landau and E.M. Lifshitz, *Course of theoretical physics: The classical theory of elds*, volume 2, Butterworth-Heinemann, (2010).

[15] J. Angus and S. Krasheninnikov,*Energy gain of free electron in pulsed electromagnetic plane wave with constant external magnetic elds*. Physics of Plasmas, 16, 113103, (2009).

[16] bibliographic information

[17] H. A. Bethe, textitTheory of passage of swift corpuscular rays through matter, Ann. Physik, 5, 325, 1930.

[18] H. A. Bethe, *Scattering of electrons*, Z. fur Physik, 76, 293, (1932).

[19] S. M. Seltzer and M. J. Berger textitBremsstrahlung energy spectra from electrons with kinetic energy 1 keV-10 GeV incident on screened nuclei and orbital electrons of neutral atoms

with z = 1-100,Atomic Data and Nuclear Data Tables, 35, 345 418 (1986).

[20] N. W. Ashcroft and N. D. Mermin, *Solid State Physics* Saunders College, Philadelphia, 1976

[21] D.G. Yakovlev and V.A. Urpin, Astron. Zh. 57, 526 (1980).

[22] Y. T. Lee and R. M. More, *An electron conductivity model for dense plasmas*, Physics of Fluids, 27 (1984), p. 1273.

[23] K. Eidmann, J. Meyer-ter-Vehn, and T. Schlegel, *Hydrodynamic simulation of subpicosecond laser interaction with solid-density matter*,Physical Review E, 62, 1, 1202 (2000).

[24] L. H. Thomas, *The calculation of atomic elds*,Mathematical Proceedings of the Cambridge Philosophical Society, 23, 542-548 (1927).

[25] M. N. Saha . *On a Physical Theory of Stellar Spectra*, Proceedings of the Royal Society A: Mathematical, Physical and Engineering Sciences 99, 697 (1921) I

[26] R. A. Snavely, M. H. Key, S. P. Hatchett, T. E. Cowan, M. Roth, T. W. Phillips, M. A. Stoyer, E. A. Henry, T. C. Sangster, M. S. Singh, S. C. Wilks, A. MacKinnon, A. Offenberger, D. M. Pennington, K. Yasuike, A. B. Langdon, B. F. Lasinski, J. Johnson, M. D. Perry, and E. M. Campbell, *Intense high- energy proton beams from petawatt-laser irradiation of solids*,Physical Review Letters 85, 2945 (2000).

[27] E. L. Clark et. al. *Measurements of Energetic Proton Transport Through Magnetized Plasma from Intense Laser Interactions with Solids*, Physical Review Letters, 84, 670 (2000).

[28] R. A. Snavely*Intense High-Energy Proton Beams from Petawatt-Laser Irradiation of Solids*, Physical Review Letters, 85, 2945 (2000).

[29] A. Maksimchuk, S. Gu, K. Flippo, D. Umstadter, and V. Y. Bychenkov textitForward Ion Acceleration in Thin Films Driven by a High-Intensity Laser, Physical Review. Letters, 84, 4108 (2000).

[30] K. Krushelnick *Multi-MeVIonProductionfromHigh- Intensity Laser Interactions with Underdense Plasmas*, Physical Review Letters, 83, 737 (1999).

[31] P. Mora *Plasma Expansion into a Vacuum*, Physical Review Letters, 90, 185002 (2003).

[32] D. Spence, P. Kean, and W. Sibbett, *60-fsec pulse generation from a self-mode-locked Ti:sapphire laser*, Optics Letters, 16, 42 (1991).

[33] F. J. McClung, and R. W. Hellwarth, *Giant optical pulsations from ruby*, Journal of Applied Physics 33 3, 828-829 (1962).

[34] D. Strickland and G. Morou, *Compression of amplified chirped optical pulses*, Optics Communications 56, 219 (1985)

[35] I. Jovanovic, B. J. Comaskey, C. A. Ebbers, R. A. Bonner, D. M. Pennington, and E. C. Morse,*Optical parametric chirped-pulse ampli- fier as an alternative to Ti:sapphire regenerative amplifiers*,Applied Optics, 41, 2923 (2002).

[36] W. Lotz *Electron-Impact Ionization Cross-Sections for Atoms up to* $Z = 108$, Z. Physik 232, 101-107, (1970).

[37] C. Hombourger*An empirical expression for K-shell ionization cross sec- tion by electron impact*, Journal of Physics B ,vol. 31, 16, 3693 (1998).

[38] W. Bambynek, *A new evaluation of k-shell fuorescence yields (fit :* $K : 5 \leq z \leq 100$*)*, (1984).

[39] A. Pak, G. Gregori, J. Knight, K. Campbell, D. Price, B. Hammel, O. L. Landen and S. H. Glenzer.*X-ray line measurements with high efficiency Bragg crystals*, Review of Scientific Instruments, 75, 10, 3747, (2004).

[40] H. Friesen, H. F. Tiedje, D. S. Hey, M. Z. Mo, A. Beaudry, R. Fedosejevs,Y. Y. Tsui, A. Mackinnon, H. S. McLean, P. K. Patel, *Kirkpatrick-Baez microscope for hard X-ray imaging of fast ignition experiments* Review of Scientific Instruments, 84, 023704 (2013).

[41] Y. Cauchois *Spectrographie des rayons X par transmission d'un faisceau non canalis travers un cristal courb*,Journal de Physique et le Radium, 3, 7, 320, (1932).

[42] C. D. Chen, J. A. King, M. H. Key, K. U. Akli, F. N. Beg, H. Chen, R. R. Freeman, A. Link, A. J. Mackinnon, A. G. MacPhee, P. K. Patel, M. Porko- lab, R. B. Stephens and L. D. Van Woerkom *A Bremsstrahlung spectrometer using k-edge and differential filters with image plate dosimeters*, Review of Scientific Instruments, 79, 10E305, (2008).

[43] *GAFCHROMIC website*,http://www.gafchromic.com, (2011).

[44] H. A. Bethe and R. W. Jackiw, *Intermediate Quantum Mechanics*. W.A. Ben- jamin, Inc., (1968).

[45] D. J. Strozzi, M. Tabak, D. J. Larson, L. Divol, A. J. Kemp, C. Bellei, M. M. Marinak, and M. H. Key,*Fast-ignition transport studies: Realistic electron source, integrated particle-in-cell and hydrodynamic modeling, imposed magnetic fields*, Physics of Plasmas 19, 072711 (2012).

[46] S. V. Bulanov and V. S. Khoroshkov, Plasma Physics Report 28, 453, (2002).

[47] S. Fritzler, V. Malka, G. Grillon, J. P. Rousseau, F. Burgy, E. Lefebvre, E. dHumires, P. McKenna, and K. W. D. Ledingham *Proton beams generated with high-intensity lasers: Applications to medical isotope production*, Applied Physics Letters 83, 30393041 (2003).

[48] P. Antici, M. Fazi, A. Lombardi, M. Migliorati, L. Palumbo, P. Audebert, and J. Fuchs. Journal of Applied Physics 104, 124901 (2008).

[49] P. K. Patel,A. J. Mackinnon, M. H. Key,T. E. Cowan, M. E. Foord, M. Allen, D. F. Price, H. Ruhl, P. T. Springer, and R. StephensPhysical Review Letters 91, 125004 (2003).